DISS. ETH NO. 25533

# A Flexible Needle with Fluoroscopic Imaging and Magnetic Steering for Neurosurgical Applications

A thesis submitted to attain the degree of

DOCTOR OF SCIENCES of ETH ZURICH

(Dr. sc. ETH Zurich)

presented by

AYOUNG HONG

MSc in Mechanical Engineering and Aerospace System

Korea Advanced Institute of Science and Technology

born on 11.09.1987

citizen of South Korea

accepted on the recommendation of

Prof. Dr. Bradley J. Nelson, examiner

Prof. Dr. Andrew J. Petruska, co-examiner

Prof. Dr. med. Ajmal Zemmar, co-examiner

2018

To my family

# Acknowledgement

This thesis would not have been possible without the support and advice from many people. Foremost, I would like to thank Prof. Bradley Nelson for giving me the opportunity to work in his group, as well as for his guidance and support. I would also like to thank Prof. Andrew Petruska for his mentorship, encouragement, and crucial contribution to this thesis. I also thank Prof. Dr. med. Ajmal Zemmar for initiating our collaboration with the University Hospital of Zurich and for being on my doctoral committee.

I am highly grateful to Dr. med. Lennart Stieglitz and Dr. med. Marcus Oertel for providing their knowledge about surgical procedures and for giving me great advice on clinical applications. I would like to acknowledge Kevin Akeret for dealing with all the demanding paperworks to get through the ethics committee. Special thanks go to all the patients who participated in the project for sharing their clinical data. I would also like to thank Prof. Fatih Toy for sharing his knowledge on digital holography.

Many thanks go to the present and past members of the Multiscale Robotics Lab. I would like to thank Brigitte Geissmann for listening to my worries and helping me to relieve them, Erdem Siringil for his technical support and Dr. Daniel Ahmed for sharing his enthusiasm towards research. I would also like to thank Dr. Quentin Boehler, Samuel Charreyron, Dr. Olgac Ergenemann, and Dr. Salvador Pane for our academic collaborations, and Jan Burri for zusammenfassung of the thesis. Thanks to Xiaopu Wang, Andre Lindo, and Juho Pokki for creating a good office environment and for sharing exotic foods and drinks. Special thanks to Bumjin Jang, Carlos Alcantara, and Hen-Wei Huang for their friendship and for having countless lunches and dinners together. I am very grateful for having them to hang out, discuss ideas, and share joy and agony. I have enjoyed my daily life with you.

My special thanks are extended to all my friends in Zurich and Korea. With their continuous messages and funny pictures, my daily life has been more colorful and energetic.

# Abstract

Neurological disorders such as epilepsy, dementia, and Parkinson's disease, are estimated to affect around one billion people worldwide, and this number is expected to increase because of a demographic transition. To date, they are treated with medication and non-invasive neurostimulation methods, including transcranial magnetic stimulation. If the methods fail and the symptoms are severe, invasive surgeries such as lesional dissection or deep brain stimulation (DBS) are performed. DBS is a common and effective surgical treatment where small electrodes are implanted at specific locations in the brain and modulates neural activities around that region using electrical signals. However, the current procedure uses a straight rigid needle, which restricts the search for feasible target areas in the brain. Robot-assisted minimally invasive surgery is a promising approach for improving the current procedures by enhancing dexterity, precision, and stability. Recent research on the magnetic steering of flexible tools have explored these strategies and demonstrated their versatility in different surgical applications.

The objective of this thesis is to develop a new robotic-based method for targeting and placing surgical tools in specific brain regions. To this end, magnetic and fluoroscopic guidance were utilized for steering a flexible needle. The respective surgical planning algorithm was then developed and evaluated. First, a fluoroscopic tracking method is developed to assess localization uncertainties associated with a single fluoroscopic image and sequentially combines different views using a Kalman filter. The method is implemented and validated for two minimally invasive surgical tools, ablation catheters and neurostimulation electrodes. Second, the steering of a flexible needle with an embedded magnetic tip is implemented based on fluoroscopic guidance. Then, a kinematic model for the magnetic needle is derived based on a nonholonomic bicycle model, and a closed-loop control strategy with feed-forward and feedback components is implemented using a chained-form transformation. The proposed needle steering method is validated through *in vitro* and *ex vivo* experiments. Finally, a surgical planning algorithm for guiding flexible magnetic needles in neurosurgical scenarios is implemented and evaluated using rapidly-exploring random trees.

# Zusammenfassung

Neurologische Erkrankungen wie Epilepsie, Demenz und Parkinson-Krankheit betreffen weltweit schätzungsweise rund eine Milliarde Menschen, und es wird erwartet, dass diese Zahl aufgrund eines demographischen Übergangs zunimmt. Bis heute werden sie mit Medikamenten und nicht-invasiven Neurostimulationsmethoden, einschlielich transkranieller Magnetstimulation, behandelt. Wenn die Methoden versagen und die Symptome schwerwiegend sind, werden invasive Eingriffe wie Läsionsdissektion oder Tiefenhirnstimulation (THS) durch-geführt. THS ist eine häufige und effektive chirurgische Behandlung, bei der kleine Elektroden an bestimmten Stellen im Gehirn implantiert werden und die neuronalen Aktivitäten in dieser Region durch elektrische Signale moduliert werden. Das derzeitige Verfahren verwendet jedoch eine gerade starre Nadel, die die Suche nach möglichen Zielgebieten im Gehirn einschränkt. Die robotergestützte minimal-invasive Chirurgie ist ein vielversprechender Ansatz zur Verbesserung der derzeitigen Verfahren durch Verbesserung von Beweglichkeit, Präzision und Stabilität. In neueren Forschungen zur magnetischen Steuerung von flexiblen Werkzeugen wurden diese Strategien erforscht und ihre Vielseitigkeit in verschiedenen chirurgischen Anwendungen bewiesen.

Ziel dieser Arbeit ist es, eine neue roboterbasierte Methode zu entwickeln, um chirurgische Instrumente in spezifischen Hirnregionen gezielt einzusetzen. Zu diesem Zweck wurde die magnetische und fluoroskopische Führung zur Steuerung flexibler Nadeln verwendet. Anschliessend wurde der entsprechende Algorithmus für die Operationsplanung entwickelt und ausgewertet. Zunächst wurde ein fluoroskopisches Tracking-Verfahren entwickelt, um die mit einem einzelnen fluoroskopischen Bild verbundenen Lokalisierungsunsicherheiten zu bewerten und um verschiedene Ansichten mit Hilfe eines Kalman-Filters sequentiell zu kombinieren. Die Methode wurde für zwei minimal-invasive chirurgische Instrumente, Ablationskatheter und Neurostimulationselektroden, implementiert und validiert. Zum anderen wurde die Steuerung der magnetischen Nadel auf der Grundlage einer fluoroskopischen Steuerung realisiert. Anschliessend wurde ein kinematisches Modell für die Magnetnadel auf Basis eines nichtholonomen Fahrradmodells abgeleitet und eine geschlossene Regelkreisstrategie mit Feed-

Forward- und Feedback-Komponenten über eine Kettenformtransformation implementiert. Die vorgeschlagene Nadelsteuerungs-methode wird durch In-vitro- und Ex-vivo-Experimente validiert. Schliesslich wurde ein chirurgischer Planungsalgorithmus zur Führung flexibler Magnetnadeln in neurochirurgischen Szenarien implementiert und mit Hilfe von rapidly-exploring-random-tree Algorithmen ausgewertet.

# Contents

# List of Tables

# List of Figures

# Abbreviations

| | |
|---|---|
| 2D | two dimensional |
| 3D | three dimensional |
| CAD | computer aided design |
| CMOS | complementary metal-oxide-semiconductor |
| CT | computed tomography |
| DBS | deep brain stimulation |
| DIH | digital in-line holography |
| DOF | degree of freedom |
| FDA | Food and Drug Administration |
| GPU | graphics processing unit |
| IPG | implanted pulse generator |
| MIS | minimally invasive surgery |
| MRI | magnetic resonance imaging |
| RRT | rapidly-exploring random tree |

# Chapter 1

# Introduction

The brain is one of the most important organs in our body. It generates and controls movement, and receives, integrates, and interprets sensory information. Our brain is also responsible for the control of blood pressure and heart rate, and associated with our intelligence, emotion, cognition, and memory. These activities are the result of the interconnection of billions of neurons in the brain. After birth, this network is maintained through neuronal migration and differentiation. Defects during this process, caused by premature death or misplaced growth can result in neurological disorders. This is suspected to be the cause behind epilepsy, Alzheimer's disease, Parkinson's disease, and schizophrenia.

This chapter starts with a broad overview of the brain anatomy and of some brain abnormalities that can cause neurological disorders. Then, deep brain stimulation (DBS) is introduced as a neurosurgical treatment for these diseases. Finally, details about the underlying surgical procedures behind DBS and its current outcomes are elaborated. Further details about the brain can be found in *Vander's human physiology* [1].

## 1.1 Human Brain Anatomy and Neurological Disorders

The human brain makes up the central nervous system together with the spinal cord. Protected by the skull and suspended in the cerebrospinal fluid, the brain consists of the cerebrum, diencephalon, brainstem, and cerebellum.

The largest component of the brain is the cerebrum, which is separated to the right and left cerebral hemispheres by a deep longitudinal groove. Underneath

they are connected by a large group of nerve fibers. The outer shell of the hemisphere is the cerebral cortex, which is divided into four lobes such as the frontal, parietal, occipital and temporal lobe. The cerebral cortex collects and processes signals from the sensory nerves through the diencephalon, and controls muscle movement by sending signals to the brainstem and spinal cord. The inner layer of the hemisphere is composed of several subcortical nuclei such as the basal ganglia, hippocampus, and olfactory bulb, which are responsible for the movement and behavior regulation.

Below the cerebrum, the diencephalon forms the central core of the brain, which includes the thalamus and hypothalamus. The first is a collection of several nuclei which serve as the synaptic relay stations to integrate inputs to the cortex, and the latter regulates homeostasis.

The brainstem and cerebellum, are situated at the base of the brain. Between the diencephalon and the spinal cord, the brainstem contains all the nerve fibers relaying signals from the other parts of the brain to the spinal cord. Through these nerve fibers, it receives and integrates inputs from all regions of the central nervous system. The brainstem is also involved in motor functions, cardiovascular and respiratory control, and sleep regulation. The cerebellum, which is located posteriorly to the brainstem, is responsible for coordination and balance, and may also have some cognitive functions.

There are two body fluids circulating in the brain, the blood and the cerebrospinal fluid. The blood is supplied to the brain through the internal carotid arteries and the vertebral arteries. It provides oxygen and glucose which is an essential source of energy to the brain. Therefore, when the blood supply is deficient for a few minutes, this can easily cause severe brain damage. The cerebrospinal fluid is produced by specialized cells in four ventricles in the brain. It circulates through the interconnected ventricles, and provides nutrients, regulates temperature and blood pressure, and clear the waste products from the brain. This fluid fills the gap between the brain and skull, supporting and protecting the soft neural tissues.

This complex structure of the brain is interconnected by neurons, which receive and transmit information using electrical signals. They are connected to muscles, glands, and sensory organs in the body through multiple neural pathways. These networks of neurons develop from the embryonic phase until birth. After that point, neurons do not experience extensive regeneration. Therefore, abnormalities and injuries in the brain's neural network can potentially cause neurological disorders.

**Celebral cortex**

Frontal lobe

Parietal lobe

Occipital lobe

Temporal lobe

Fornix

**Cerebrum**

Cingulate cortex

Thalamus

Hippocampus

**Thalamic Nuclei**

ANT

VA

VL

VI

VPL

CM

VPM

Globus pallidus

**Cerebellum**

**Brainstem**

Spinal cord

| | |
|---|---|
| **ANT** | Anterior |
| **VA** | Ventral anterior |
| **VL** | Ventral lateral |
| **VI** | Ventral intermedial |
| **VPL** | Ventral posterolateral |
| **VPM** | Ventral posteromedial |
| **CM** | Centromedian |
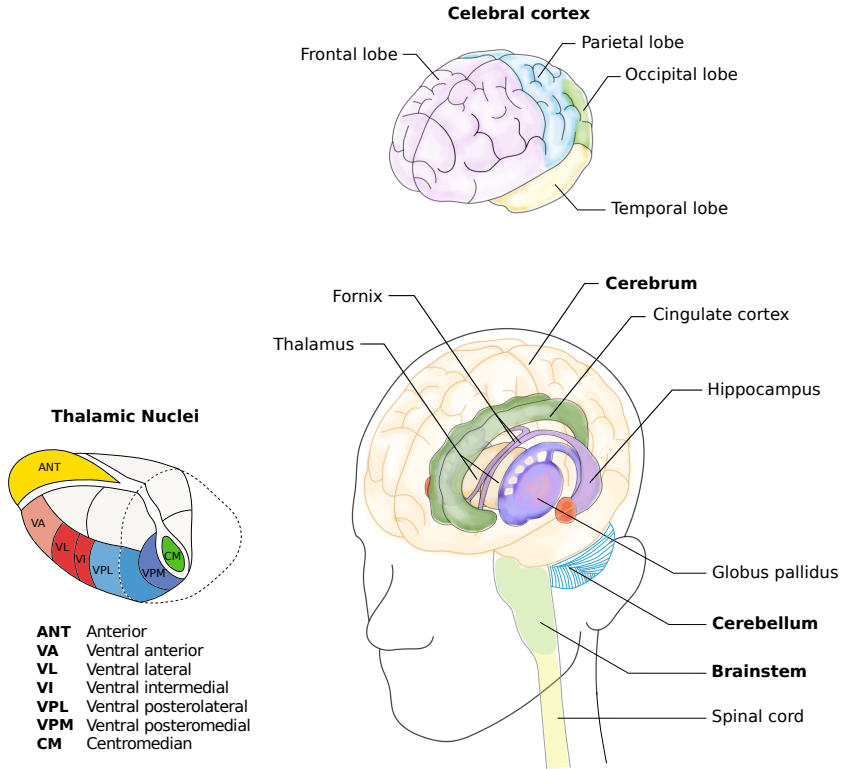
Figure 1.1 : The human brain anatomy.

Parkinson's and Alzheimer's disease, epilepsy, and dystonia are examples of neurological disorders currently affecting hundreds of millions of people worldwide [2]. The most widely accepted causes for these conditions are associated with the death of neurons or abnormal neural activities in the brain [3], [4]. Ongoing solutions used to rectify these issues include both medication and non-invasive neurostimulation such as transcranial magnetic stimulation. If those methods fail and the symptoms are severe, invasive surgeries such as deep brain stimulation or ablation are performed.

Table 1.1 : DBS for Different Neurological Disorders

| Disease | Possible Targets | Comments |
|---|---|---|
| Parkinson's Disease[†] | STN, GPi | The most common DBS indication. |
| Essential tremor[†] | VIM | First FDA-approved target for essential tremor and tremor-dominant disorders [10]. |
| Dystonia[†] | VL, GPi | Pediatric DBS for treating dystonia is under investigation [11]. |
| Epilepsy[†] | ANT | Only used for patients who cannot have resective brain surgery [12], [13]. |
| Alzheimer's Disease | Fornix | A transventricular approach is required to reach fornix [14]. |
| Tourette's Syndrome / OCD | CM, GPi | DBS for treatment-resistant OCD is approved under a Humanitarian Device Exemptions.[a] |
| Depression | NAc, SCC, VC/VS, Lateral Habenula | Small number of clinical studies have demonstrated the antidepressant effects for treatment-resistanc depression [8], [15]. |
| Pain Syndrome | VPL,VPM | The patient selection is more important than other disorders [9] |

[†] These are the FDA-approved applications.
[a] HDE is the FDA approval process for the devices for a rare disease or condition.
NAc, nucleus accumbens; SCC, subcallosal cingulate;

## 1.2 Deep Brain Stimulation

Deep Brain Stimulation (DBS) is a well-established neurosurgical technique used to treat a variety of neurological disorders with high efficacy. Millimeter-sized electrodes are implanted into a specific region of the brain and connected to an implanted pulse generator (IPG) which controls the electrical stimulus. DBS has been successfully applied to movement disorders such as Parkinson's disease or Essential Tremor [5], [6], psychiatric disorders such as depression or obsessive-compulsive disorder [7], [8], and pain syndromes such as chronic pain after stroke or amputation [9]. Depending on the type of neurological disorders, different brain regions are targeted for stimulation, as described in Table 1.1.

Frame-based Method                                    Frameless Method



(a)                    (b)                    (c)                    (d)
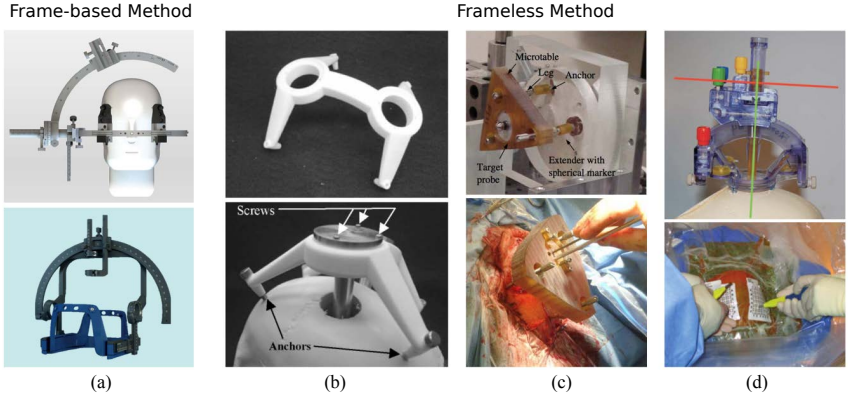
Figure 1.2 : Electrode placement systems utilized in DBS surgery : frame-based and frameless method. (a) ZD-stereotactic system from inomed (Emmendingen, Germany) and Leksell Vantage from Elekta (Stockholm, Sweden). (b,c) A customizable frame STarFix microTargeting platform and Microtable developed at Venderbilt University [18], [19]. (d) ClearPoint system with the skull-mounted aiming device SmartFrame for interventional MRI-guided DBS from MRI Interventions Inc (Irvine, CA, USA).

### 1.2.1 Surgical Procedure

To determine the exact location of an electrode with respect to the target region, we need a coordinate system fixed to the patient's head. The most common placement method is the frame-based method, shown in Figure 1.2 (a). A stereotactic head frame is mounted around the patient's head and the preoperative imaging is acquired with a localization device attached to the frame. This introduces the polar coordinate system, which designates the target point as the center of the sphere and the trajectory as a straight line along the movement axis. This frame-based method is capable of sub-millimeter accuracy.

A relatively new frameless method is presented in Figure 1.2 (b-d). The guiding appliance is directly fixed on the patient's head with three or four bone-screws, which later serve as the fiducial markers. The advantages of frameless systems are their flexibility and reduced weight, which enable mounting without space restrictions such that they can be used in magnetic resonance imaging (MRI) scanners [16]. However, the frameless systems have less accuracy than the frame-based system due to their coordinate system [17]. The small discrepancy in the insertion axis can influence the tip of the electrode.

Figure 1.3 : Surgical procedure of DBS. Images taken from [20]–[25]

Implanting an electrode in a specific region of the brain is a complicated and sensitive procedure. The exact steps of DBS surgery always depend on the neurosurgeon's preference and experience, as well as available clinical devices. Nevertheless, most of the surgeries can be split into the following steps, as outlined in Figure 1.3:

- Preoperative target identification and surgical planning
- Intraoperative targeting and electrode implantation
- Postoperative validation
- IPG implantation and programming

Here, the procedure of DBS is explained in detail based on the protocol used in the University Hospital of Zurich, however, it may differ in other centers. Target identification and surgical planning is the first step of a DBS procedure, based on the preoperative imaging. Depending on the electrode placement method, either frame-based or frameless, the relevant frames or fiducials are implanted under local anesthesia prior to the surgery. Then the preoperative MRI and CT

are acquired to localize frames or fiducials and identify the anatomical targets. Usually, MRI is utilized to obtain a high resolution image of soft tissues and CT is done after frame placement to identify the frame positions. Then, the pre-operative MRI is merged with the CT scan to locate the target in high-resolution MRI in reference to the frame positions on the CT scan. Based on these imaging modalities, the neurosurgeon determines the insertion point(s) and surgical trajectory with the help of a computer-assisted system such as StealthStation from Medtronic [21].

In the operating room, a small hole is first drilled into the patient's skull based on the planned insertion point. Then the microdrive is attached to the stereotactic frame or fiducial screws. The microelectrode is inserted along the planned trajectory in submillimetric scales using the microdrive. This micro-electrode records the intraoperative physiological information near the preoperatively planned target location which can be used for confirmation and refinement for anatomical localization. The same microelectrode is also used for direct stimulation, which is useful to test the stimulation-evoked paresthesia or motor contractures and to check the alleviation of the symptoms such as tremor and rigidity. Once the final location is determined, the DBS electrode is implanted. The final electrode position is confirmed, e.g. via fluoroscopy.Postoperative position verification is currently done in several ways, including 3D localization using a CT or MRI scan. At certain centers, this includes that the patient is transported out of the operation room to the scanner with the frame mounted. If there is suboptimal discrepancy of the electrode placement, the patient needs to be brought back to the operation room for a second insertion.

Once the entire neurosurgical procedure is performed and verified, the IPG is implanted in a preformed pocket subcuteaneously in the chest, and connected to the DBS lead with an extension wire. The initial programming is usually performed a few days or weeks after the surgery when the patient has returned to the symptomatic baseline. During the adjustment procedure, a few adaptations on pulse amplitude, width, and frequency are required to stabilize the clinical benefit for long-term follow-up [26].

### 1.2.2 Current Outcome

The efficacy and safety of DBS is well established. The stimulation of the subthalamic nucleus , which is one of the most common targets for Parkinson's disease, can reduce the motor fluctuation by more than 50% [27]. The stimulation of

the ventral capsule/ventral striatum (VC/VS) relieves the symptoms of patients with highly-resistant obsessive-compulsive disorder [7], [28]. DBS treatment for chronic pain, which was the original purpose of its development, was found to be effective in patients whose chronic pain was traceable to specific brain regions [29]. Recently, small numbers of clinical studies have also demonstrated the antidepressant effect of DBS for treatment-resistant depression [8], [15]. DBS has several advantages over other procedures such as pallidotomy or thalamotomy, wherein a small region of the brain is destroyed or removed, because the stimulation-related side effects can be reversed [30] and the reimplantation of the electrode is also feasible.

However, despite the promising outcome of DBS in treating various neurological disorders, a few complications have been reported with the current technique [31], [32]. One group is related to hardware implantation. Hemorrhages, one of the most serious complications, can occur at various steps in the DBS procedure such as microelectrode recording, guide tube insertion, and final electrode implantation, when the trajectory crosses through the vessels and the ventricles. This can happen at various steps in the DBS procedure such as microelectrode recording, guide tube insertion, and final electrode implantation. The second group is related to hardware defects and infections, which can affect one tenth of patients. This includes electrode fractures, electrode migrations, short or open circuits, infections and allergic reactions associated with IPGs or electrodes [32], [33]. The other common complications are stimulation-related adverse effects. During the adaptation time of IPG programming, most of the patients experience side-effects. Some neuropsychiatric symptoms, including depression, anxiety, apathy, or suicide attempts in severe cases, could occur after DBS surgery. Also, cognitive decline in verbal fluency, long-term memory, and processing speed have been reported [34], [35].

DBS is a common and effective neurosurgical treatment. However, a few adverse complications exist and the exact physiological mechanism of the treatment still remains unknown [36]. A better understanding of brain physiology and patholody would definitely help to explore the action mechanism of DBS, thus providing new guidelines for designing electrodes and IPGs. On the other hand, as the fundamental purpose of current DBS technique is to modulate neural activities at a specific brain region, careful preoperative targeting and precise electrode placement are important factors [37]. Therefore, improved targeting methods and new placement methods would enhance technical development in

DBS.

## 1.3 Thesis Outline

This thesis aims to enhance the current neurosurgical technique, where the purpose is to place surgical tools at specific locations in the brain region in a precise and safe manner, by means of new targeting and placing methods. Fluoroscopic imaging is used to localize small surgical tools because it is the most available imaging modality in the operating room and provides good resolution and frame rates. Under fluoroscopic guidance, a new placement method using a flexible needle and a magnetic steering system is implemented. A surgical planning algorithm that uses a sampling-based method and considers surgical constraints is demonstrated to facilitate the placement of neurosurgical tools.

Chapter 2 outlines the current robotic solutions in neurosurgery. It introduces different robotic systems developed for neurosurgery, and imaging or sensing technologies used for those systems in the operating room. In Chapter 3, a tracking method using a single fluoroscope is presented. The proposed method is validated with different minimally invasive tools. In Chapter 4, a magnetically guided flexible needle is modeled and implemented using the proposed tracking method for neurosurgical application. Using a fluoroscopic feedback of the needle tip position and orientation, the proposed control strategy is validated in a brain phantom tissue and a biological tissue. Chapter 5 presents a surgical planning approach for flexible needles to aid neurosurgeons to adapt to the new proposed method.

# References

[1] E. P. Widmaier, H. Raff, and K. T. Strang, *Vander's human physiology: the mechanisms of body function*. McGraw-Hill Higher Education, 2008.

[2] WHO, *Neurological disorders: public health challenges*. World Health Organization, 2006.

[3] G. L. Wenk *et al.*, "Neuropathologic changes in alzheimer's disease," *Journal of Clinical Psychiatry*, vol. 64, pp. 7–10, 2003.

[4] A. Krumholz, "Epilepsy: A comprehensive textbook," *Annals of Neurology: Official Journal of the American Neurological Association and the Child Neurology Society*, vol. 45, no. 6, pp. 825–825, 1999.

[5] A.-L. Benabid, P. Krack, A. Benazzouz, P. Limousin, A. Koudsie, and P. Pollak, "Deep brain stimulation of the subthalamic nucleus for parkinson's disease: Methodologic aspects and clinical criteria.," *Neurology*, vol. 55, no. 12 Suppl 6, S40–4, 2000.

[6] J. Jankovic, "Treatment of hyperkinetic movement disorders," *Lancet Neurol*, vol. 8, no. 9, pp. 844–856, 2009.

[7] B. D. Greenberg, D. A. Malone, G. M. Friehs, A. R. Rezai, C. S. Kubu, P. F. Malloy, S. P. Salloway, M. S. Okun, W. K. Goodman, and S. A. Rasmussen, "Three-year outcomes in deep brain stimulation for highly resistant obsessive-compulsive disorder," *Neuropsychopharmacology*, vol. 31, no. 11, p. 2384, 2006.

[8] D. R. Cleary, A. Ozpinar, A. M. Raslan, and A. L. Ko, "Deep brain stimulation for psychiatric disorders: Where we are now," *Neurosurg Focus*, vol. 38, no. 6, E2, 2015.

[9] E. A. Pereira and T. Z. Aziz, "Neuropathic pain and deep brain stimulation," *Neurotherapeutics*, vol. 11, no. 3, pp. 496–507, 2014.

[10] Food and Drug Administration, Available at: https://www.fda.gov/.

[11] E. L. Air, J. L. Ostrem, T. D. Sanger, and P. A. Starr, "Deep brain stimulation in children: Experience and technical pearls," *J Neurosurg Pediatr*, vol. 8, no. 6, pp. 566–574, 2011.

[12] V. Salanova, T. Witt, R. Worth, T. R. Henry, R. E. Gross, J. M. Nazzaro, D. Labar, M. R. Sperling, A. Sharan, E. Sandok, *et al.*, "Long-term efficacy and safety of thalamic stimulation for drug-resistant partial epilepsy," *Neurology*, vol. 84, no. 10, pp. 1017–1025, 2015.

[13] C. H. Halpern, U. Samadani, B. Litt, J. L. Jaggi, and G. H. Baltuch, "Deep brain stimulation for epilepsy," in *Neuromodulation*, Elsevier, 2009, pp. 639–649.

[14] F. A. Ponce, W. F. Asaad, K. D. Foote, W. S. Anderson, G. Rees Cosgrove, G. H. Baltuch, K. Beasley, D. E. Reymers, E. S. Oh, S. D. Targum, *et al.*, "Bilateral deep brain stimulation of the fornix for Alzheimer's disease: Surgical safety in the advance trial," *J Neurosurg*, vol. 125, no. 1, pp. 75–84, 2016.

[15] B. H. Bewernick, S. Kayser, V. Sturm, and T. E. Schlaepfer, "Long-term effects of nucleus accumbens deep brain stimulation in treatment-resistant depression: Evidence for sustained efficacy," *Neuropsychopharmacology*, vol. 37, no. 9, p. 1975, 2012.

[16] P. A. Starr, L. C. Markun, P. S. Larson, M. M. Volz, A. J. Martin, and J. L. Ostrem, "Interventional MRI–guided deep brain stimulation in pediatric dystonia: First experience with the clearpoint system," *J Neurosurg Pediatr*, vol. 14, no. 4, pp. 400–408, 2014.

[17] H. Bjartmarz and S. Rehncrona, "Comparison of accuracy and precision between frame-based and frameless stereotactic navigation for deep brain stimulation electrode implantation," *Stereotact Funct Neurosurg*, vol. 85, no. 5, pp. 235–242, 2007.

[18] R. Balachandran, J. E. Mitchell, B. M. Dawant, and J. M. Fitzpatrick, "Accuracy evaluation of microtargeting platforms for deep-brain stimulation using virtual targets," *IEEE Trans Biomed Eng*, vol. 56, no. 1, pp. 37–44, 2009.

[19] R. F. Labadie, J. Mitchell, R. Balachandran, and J. M. Fitzpatrick, "Customized, rapid-production microstereotactic table for surgical targeting: Description of concept and in vitro validation," *Int J Comput Assist Radiol Surg*, vol. 4, no. 3, pp. 273–280, 2009.

[20] R. L. O'Gorman, J. M. Jarosz, M. Samuel, C. Clough, R. P. Selway, and K. Ashkan, "CT/MR image fusion in the postoperative assessment of electrodes implanted for deep brain stimulation," *Stereotact Funct Neurosurg*, vol. 87, no. 4, pp. 205–210, 2009.

[21] Medtronic, Available at: https://www.medtronic.com/.

[22] Inomed Medizintechnik GmbH, Available at: https://www.inomed.com.

[23] Boston Scientific, Available at: http://www.bostonscientific.com/.

[24] Elekta Instrument AB Stockholm, Available at: https://www.elekta.com/.

[25] J. Y. Lee, J. W. Kim, J.-Y. Lee, Y. H. Lim, C. Kim, D. G. Kim, B. S. Jeon, and S. H. Paek, "Is MRi a reliable tool to locate the electrode after deep brain stimulation surgery? comparison study of CT and MRI for the localization of electrodes after DBS," *Acta Neurochir*, vol. 152, no. 12, pp. 2029–2036, 2010.

[26] J. Volkmann, E. Moro, and R. Pahwa, "Basic algorithms for the programming of deep brain stimulation in parkinson's disease," *Mov Disord*, vol. 21, no. S14, S284–S289, 2006.

[27] P. Krack, A. Batir, N. Van Blercom, S. Chabardes, V. Fraix, C. Ardouin, A. Koudsie, P. D. Limousin, A. Benazzouz, J. F. LeBas, *et al.*, "Five-year follow-up of bilateral stimulation of the subthalamic nucleus in advanced Parkinson's disease," *N Engl J Med*, vol. 349, no. 20, pp. 1925–1934, 2003.

[28] D. D. Dougherty, A. R. Rezai, L. L. Carpenter, R. H. Howland, M. T. Bhati, J. P. O'Reardon, E. N. Eskandar, G. H. Baltuch, A. D. Machado, D. Kondziolka, *et al.*, "A randomized sham-controlled trial of deep brain stimulation of the ventral capsule/ventral striatum for chronic treatment-resistant depression," *Biol Psychiatry*, vol. 78, no. 4, pp. 240–248, 2015.

[29] D. Rasche, P. C. Rinaldi, R. F. Young, and V. M. Tronnier, "Deep brain stimulation for the treatment of various chronic pain syndromes," *Neurosurg Focus*, vol. 21, no. 6, pp. 1–8, 2006.

[30] A. Machado, A. R. Rezai, B. H. Kopell, R. E. Gross, A. D. Sharan, and A.-L. Benabid, "Deep brain stimulation for parkinson's disease: Surgical technique and perioperative management," *Mov Disord*, vol. 21, no. S14, S247–S258, 2006.

[31] R. Bakay and A. Smith, "Deep brain stimulation: Complications and attempts at avoiding them," *Open Neurosurg J*, vol. 4, no. Suppl 1-M4, pp. 42–52, 2011.

[32] M. Y. Oh, A. Abosch, S. H. Kim, A. E. Lang, and A. M. Lozano, "Long-term hardware-related complications of deep brain stimulation," *Neurosurgery*, vol. 50, no. 6, pp. 1268–1276, 2002.

[33] K. A. Sillay, P. S. Larson, and P. A. Starr, "Deep brain stimulator hardware-related infections: Incidence and management in a large series," *Neurosurgery*, vol. 62, no. 2, pp. 360–367, 2008.

[34] V. Voon, C. Kubu, P. Krack, J.-L. Houeto, and A. I. Tröster, "Deep brain stimulation: Neuropsychological and neuropsychiatric issues," *Mov Disord*, vol. 21, no. S14, 2006.

[35] H. L. Combs, B. S. Folley, D. T. Berry, S. C. Segerstrom, D. Y. Han, A. J. Anderson-Mooney, B. D. Walls, and C. van Horne, "Cognition and depression following deep brain stimulation of the subthalamic nucleus and globus pallidus pars internus in Parkinson's disease: a meta-analysis," *Neuropsychol Rev*, vol. 25, no. 4, pp. 439–454, 2015.

[36] K. Ashkan, P. Rogers, H. Bergman, and I. Ughratdar, "Insights into the mechanisms of deep brain stimulation," *Nat Rev Neurol*, vol. 13, no. 9, p. 548, 2017.

[37] C. C. McIntyre, A. Chaturvedi, R. R. Shamir, and S. F. Lempka, "Engineering the next generation of clinical deep brain stimulation technology," *Brain Stimul*, vol. 8, no. 1, pp. 21–26, 2015.

# Chapter 2

# Robotics in Neurosurgery

In this chapter, different robots that are used in neurosurgery are introduced, and the tracking methods and surgical planning approaches that aid those robots are elaborated. A review on surgical robots can be found in [1]–[3] and those particularly focusing on neurosurgical applications are covered in [4]–[10].

## 2.1 Surgical Robots in Neurosurgery

Surgical robots are categorized into passive and active robots based on their different mechanisms [1]. Passive robots usually serve as tool holding devices. The earliest applications of surgical robots were in this category, where they were used to hold fixtures at predefined locations and help surgeons perform the rest of neurosurgical procedures. Active robots are more involved in the surgical procedure. They perform complex tasks such as skull drilling, tissue dissection, and electrode implantation, which were previously carried out by neurosurgeons.

According to their interaction with surgeons, surgical robots can be further classified into three categories which are supervisory-controlled, teleoperated, and shared-control systems [5]. In supervisory-controlled systems, robots are able to perform fully automated procedures. Surgeons can specify the motion of the robot prior to the operation, and the robots follow the programmed motion in the operating room. The surgeons are close to the patients and robots, however, they do not need to intervene until it becomes necessary. In teleoperated systems, surgeons have full control over robots from remote sites. They can obtain real-time visual feedback from surgical scenes through the use of cam-

eras, and haptic feedback from force sensors that are integrated into the robots. These feedback signals aid surgeons to control master devices as if they were operating on the patients, while the robot motion is determined by following the master device. In shared-control systems, surgeons and robots share the control over surgical instruments. The surgical procedure is carried out by surgeons, while the robots serve as a complement for steady-hand manipulation, such as reducing the surgical tremor.

In the following section, robots used in neurosurgery are reviewed, and I also have discussed potential surgical robots that can be used in neurosurgery.

### 2.1.1 Robotic Arms

Earlier studies used industrial robotic arms as passive tool holders for surgical applications [11]. The calibrated robotic arm was used to register preoperative CT scans of patients in the operating room and then moved to the desired position at which a burr-hole is located by supervisory-control. Then the robots were locked in the stationary position, thus allowing the surgeons to perform biopsy. An industrial robotic arm was recently tested for stereotactic neurosurgery as an active tool [12]. The robot autonomously drilled a burr-hole, inserted a guidewire, and implanted electrodes in the pig's brain, following the planned trajectory.

Surgical robots such as the neuromate, the ROSA, and the Renaissance, are designed and developed for neurosurgical applications such as deep brain stimulation, stereoelectroencephalography, and brain tumor resection as shown in Figure 2.1. The clinical outcomes of the neuromate and the ROSA have improved the current technology by minimizing the surgical risks and time [13], [14]. These robots have used shared-control by restricting the workspace with the haptic feedback system. For example, the surgical drilling instrument was attached to the end-effector of the neuromate, which resulting in an improvement regarding the safety and stability of the drilling procedure [15]. A miniaturized parallel robot like the Renaissance has been developed to reduce the physical footprint of surgical robots in the operating room [16]. This robot was mounted directly on the skull and was able to guide the surgical tools based on planning software [17].

(a) neuromate®        (b) ROSA®        (c) Renaissance®

Figure 2.1 : Robot arms used in neurosurgery. (a) neuromate® stereotactic robot from Renishaw (Gloucestershire, UK). (b) ROSA® robot from Medtech (France). (c) Renaissance® guidance system from Mazor Robotics (Caesarea, Israel).



(a) Dissector Tool        (b) Craniostar        (c) Micron for microsurgery
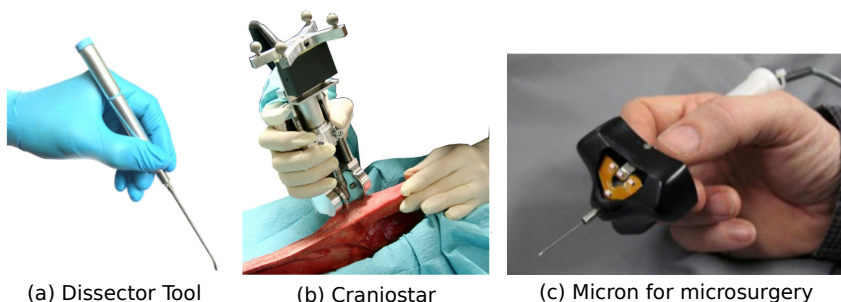
Figure 2.2 : Hand-help surgical robots. (a) A hand-held device for neurosurgical micro-dissection developed at Imperial College London [18]. (b) A hand-held robot for craniotomy developed at University of Heidelberg [19]. (d) An actively stabilized hand-help tool for microsurgery developed at Carnegie Mellon University [20].

### 2.1.2 Hand-held Surgical Robots

Hand-held robotic tools have recently drawn attention due to their compactness, simple manipulation, and easy integration into the surgical workflow [21]. These tools can assist the surgeons to filter out tremor, provide haptic feedback, and constrain motion under shared-control.

Payne *et al.* have developed a hand-held haptic dissector for neurosurgical microdissection task [18], as shown in Figure 2.2 (a). By measuring the tip deflection of the dissection tool, the force applied to the tissue was calculated. When this force exceeds a critical threshold, the hand-held device gives a warning to

(a) neuroArm

(b) da Vinci® Surgical System
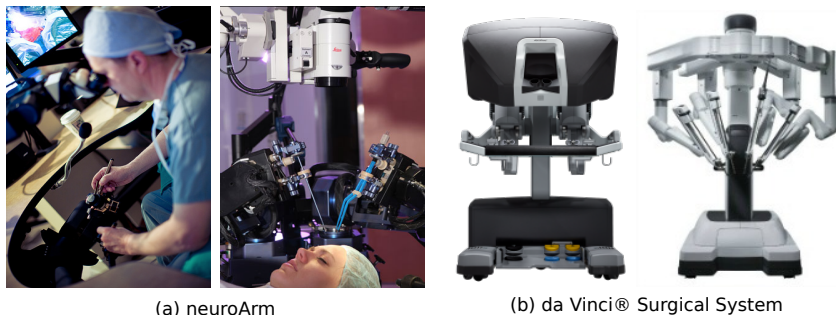
Figure 2.3 : Telesurgical systems. (a) A teleoperated neurosurgical robotic system, neuroArm, developed at University of Calgary [23]. (b) da Vinci® surgical system from Intuitive Surgical (Sunnyvale, CA, USA).

the surgeons by haptic vibration. This enhances the safety of the operating procedure.

To aid neurosurgeons drilling a burr-hole into the skull, hand-held robots like the Craniostar [19] and the STS [22] have been used as shown in Figure 2.2 (b). The Craniostar, integrated with two-wheel drives and a drill, performed craniotomy following the preoperatively planned trajectory under shared control with surgeons. The STS device enhanced the safety of the procedure by monitoring the drilling depth into the skull and comparing its depth with the preoperative CT/MR imaging data.

Hand-held devices such as the Micron[20] shown in Figure 2.2 (c) have reduced the involuntary motion of eye surgeons by imposing piezoelectric actuators that move the tooltip opposite to the tremor direction, thus, it acts as a stabilizer for vibration. These robots were initially developed for ophthalmic microsurgery. Nonetheless, the resulting performance demonstrated their versatility to assist neurosurgical procedures.

### 2.1.3 Telesurgical Robots

Telesurgical robots are used to carry out surgical procedures even when the patient and the surgeons are not in the same location. This enables intraoperative imaging without exposing surgeons to radiation. The robots are mainly teleoperated, however, the control interface between the master and the slave robots provide shared control capabilities. For example, the motion captured

from the master devices is filtered out and scaled down before sending it to the slave robots. The dexterity of the telesurgical robots is highly dependent on their end-effectors, which have evolved from rigid tools to flexible continuum robots [24], [25].

The neuroArm, a teleoperated robotic systems, was developed for microneurosurgery and MR-guided stereotaxy [23], [26] as shown in Figure 2.3 (a). The surgeons manipulate the master devices that have positional and force feedback capabilities. The robotic arms on the slave-side can perform the surgical procedure under the master-slave control architecture. The strength of the neuroArm was to conduct operating procedures such as needle insertion, soft tissue cutting, and irrigation under intraoperative MR guidance. Recent reports have shown the successful clinical outcomes of the neuroArm for microdissections of different tumors [27], [28].

The most established telesurgical robotic system is the *da Vinci* surgical system shown in Figure 2.3 (b). This system was first developed for open abdominal remote telesurgery and has extended to minimally invasive surgery (MIS) in urology and cardiology [29]–[31]. Recently, the feasibility and safety of the *da Vinci* system used in keyhole neurosurgery were examined in a cadaver study [32]. However, researchers have concluded that the system is not optimal for brain surgery since the multiple bulky arms inhibit maneuverability through the burr-hole and limit endoscopic visualization.

### 2.1.4 Flexible Continuum Robots

Continuum robots are structured with infinite degrees of freedom, which is a fundamental difference to conventional manipulators composed of discrete rigid joints [33]. This allows the robots to have an increased dexterity because of their flexible bodies, which allows them to traverse through confined anatomies without harming the patients. Continuum robots can be used as the end-effector of telesurgical systems, and also designed as independent surgical robots.

The NIOBE shown in Figure 2.4 (a) has been developed to guide cardiac ablation catheters using remote magnetic navigation [34], [35]. This system consists of two permanent magnets which actively change their orientation to steer magnetic catheters. According to the direction of the generated uniform magnetic field, the tip of the catheters is aligned along that direction. Krings *et al.* have presented a neuroradiological application of the NIOBE system [36]. The navigation of microguidewires was demonstrated in tortuous vessel anatomy and

(a) NIOBE®

(b) ICH evacuation robot

(c) steerable needles
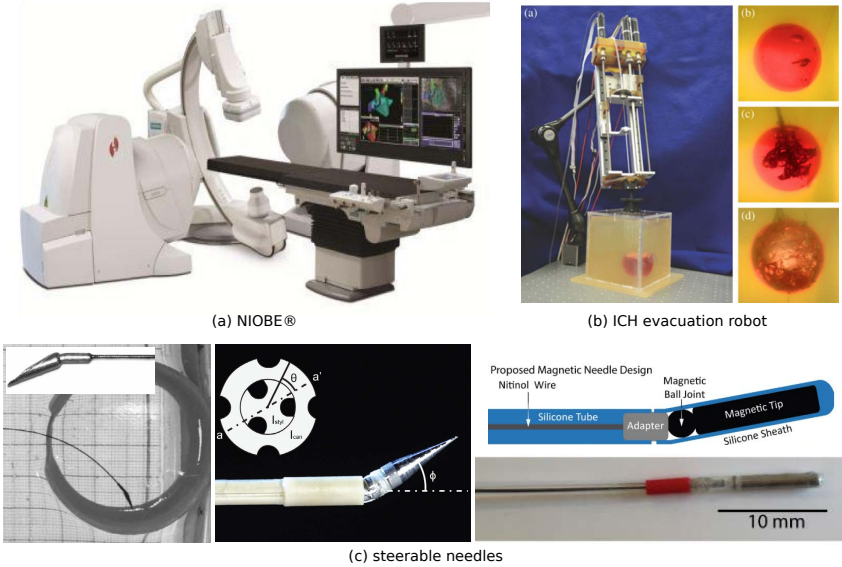
Figure 2.4 : Flexible Continuum Robots. (a) NIOBE® magnetic navigation system from Stereotaxis (St.Louis, MO, USA). (b) A robotic steerable cannula for intracerebral hemorrhage evacuation developed at Vanderbilt University [39]. (c) Steerable needles with a bevel-tip [41], tendon actuation [42] and magnetic guidance [43] developed at Carnegie Mellon University, Delft University of Technology and ETH Zürich, respectively.

*in-vitro* aneurysms. Using custom-made microcatheters and the NIOBE system, Kara *et al.* first demonstrated endovascular guidance into the deep intracerebral venous structure of animal models [37].

Concentric tube robots, which are composed of several precurved tubes, have been suggested for neurosurgical applications such as neuroendoscopy [38] and intracerebral hemorrhage evacuation [39]. Butler *et al.* have utilized the robots to access cerebral ventricles in the brain. Under teleoperated control, the surgeons were able to navigate the robots, more safely and smoothly in the phantom model of ventricles with a shorter learning time. A similar precurved cannula as the one shown in Figure 2.4 (b) was used to treat intracerebral hemorrhage. Additionally, Bergeles *et al.* have proposed a method to optimize the design of concentric tube robots based on their surgical task [40].

As flexible needles traverse through soft tissues, instead of navigating within

blood vessels or anatomical cavities, they interact with tissues which causes tool deflection [44]. The asymmetric geometry of the needle tip creates a moment that deforms the flexible needle following a curved trajectory. This allows obstacle avoidance with motion planning and helps to reach the deep brain region more safely. Examples of flexible needles are shown in Figure 2.4 (c). The bevel-tipped needle was examined to reach multiple targets from one burr hole in a cadaveric brain [41]. To increase the tip dexterity, flexible needles with tip actuation were developed. For example, Berg *et al.* used four cables to connect the needle tip and four actuators at the needle base, respectively [42]. Petruska *et al.* designed a flexible needle with a permanent magnet at the tip to manipulate it under magnetic guidance [43]. Ko *et al.* used four bevel-tipped probes with different tip orientations inspired by an egg-laying channel present in insects [45].

## 2.2 Tracking Technologies

An accurate and efficient tracking method is important to guide neurosurgical robots. This tracking method can be classified in two categories; the first method uses a non-invasive imaging modality available in the operating room, and the second method utilizes position or shape sensors. Among those tracking technologies, the methods proposed and utilized in surgical robots are detailed in the following sections.

### 2.2.1 Intraoperative Imaging Modalities

A few imaging modalities are available in the operating room, such as X-ray fluoroscopy, intraoperative CT/MRI, and ultrasonography. The advantage of implementing these modalities is that the precise location of pathologies along with other anatomical structures are visible in the image simultaneously.

X-ray fluoroscopy is the most used imaging modality in the clinic because it provides sufficient resolution and frame rates, compared to other non-invasive imaging modalities. However, the fluoroscopic method has drawbacks such as harmful radiation exposure to patients and surgeons, which is inevitable, and lack of depth perception [46]. To overcome the 2D nature of single-axis fluoroscopy, multiple views from different angles are taken. For example, Talukdar *et al.* used a rotational C-Arm fluoroscope to visualize the anatomical structures in 3D with tanhe optimized C-Arm geometry [47]. Shirato *et al.* used four fluoroscopic systems to track a gold marker embedded in the tumor lesion for radiotherapy [48].

Fluoroscopic tracking has been recently demonstrated in the tracking of surgical robots. For example, Glozman *et al.* manipulated a flexible needle into a muscle tissue under fluoroscopic guidance [49] and Vandini *et al.* estimated the position and shape of concentric tube robots within a tissue model [50].

Intraoperative MRI provides high-resolution imaging of soft tissues without harmful X-ray radiation, Therefore, it is widely used in image-guided neurosurgery such as in electrophysiology and endovascular procedures [51]. However, the major limitation of MRI is that the surgical procedure must be performed with non-ferromagnetic devices. This requires additional development of surgical tools. For example, an MR-compatible stereotactic device was developed to allow intraoperative visualization of the surgical instrument and the intended target in the brain [52].

Ultrasonography is another commonly used intraoperative imaging modality. An ultrasound device is portable, inexpensive, and can offer images of soft tissues in real-time. However, one drawback of the system is its limited field of view. Therefore, it is difficult to image structures behind bones [53]. This problem could be solved by inserting a small ultrasound probe directly into the resection cavity, which can reduce the influence of artifacts [54]. In surgical robotic applications, ultrasound has been used to track a resection robot in prostate surgery [55] and flexible needles [56], [57].

### 2.2.2 Sensing Technologies

Surgical robots can be localized with embedded sensors, such as electromagnetic sensors and optical fibers. These sensors can provide high precision and acquire data at a high frequency. Since this method only offers information about surgical robots, additional image registration is required to locate the robots with respect to the patient's anatomy.

Electromagnetic sensors have been used to track surgical robots, such as flexible needles and catheters. This tracking method using electromagnetic sensors is available without line-of-sight restrictions, which can easily localize robots inside patients. However, this method has some drawbacks [58], [59]. One is that the tracking accuracy can drop when the sensor is close to any disturbing objects such as other imaging devices in the operating room and pacemakers implanted in the patients. Another drawback is that additional devices such as magnetic field generators are required in the operating room. Currently, tracking methods that integrate electromagnetic sensors with other imaging modalities have been

demonstrated. For example, Tran *et al.* combined 2D information from fluoroscopic images and pose information from electromagnetic sensors to estimate the 3D shape of the catheters. Depending on the type of electromagnetic sensors and magnetic field generators, many commercial products are available for medical applications [60]–[62].

Optical fibers fabricated with fiber-Bragg-grating (FBG) have been proposed to calculate the shape of surgical tools such as colonoscopes [63] and flexible needles [42], [64], [65]. A number of FBG sensors are integrated into the surgical robots and used to measure the axial strain of the placed position when they are elongated or compressed under mechanical loading. Then, the curvature of each position is calculated to estimate the position and shape of the robots. This method fully relies on optics, therefore, it does not interfere with other medical devices that generate electrical and magnetic signals. The sensors can provide accurate and fast shape information of flexible tools, however, the integration into small devices remains a challenge.

## 2.3 Computer-Assisted Surgical Planning

Computer-assisted surgical planning is used to aid surgeons during preoperative planning, and to reduce the time for actual surgery by optimizing the procedures, thus enhancing the clinical outcomes. Planning begins with the understanding of preoperative images of patients. The surgical targets and structures are automatically segmented from images, and surgical procedures are planned with the help of treatment-specific algorithms. In the last stage, surgeons validate the planning results [9]. This surgical planning is specific to the patients, surgical devices, and treatment procedures. Therefore, the involvement of new surgical robots changes the current procedures and requires updates on the planning algorithms, including the development of new planning methods.

Robotic arms are used as tool holding devices in the operating room. Their location and posture should be acquired precisely concerning the patients' anatomy. This can be calculated by registration and intraoperative imaging of fiducial markers mounted on the robotic arms using computer-assisted surgical planning [66].

The *da Vinci* telesurgical system is another example that considerably affected surgical procedures. It brought in new robotic tools and imaging systems which helped to overcome many limitations of minimally invasive surgery. They allowed a full range of manipulation inside the patients and enables a stable

camera platform with depth perception [3]. However, this invention requires extensive training for surgeons. On the other hand, planning algorithms can help to ease this process. For example, Adhami *et al.* optimized the incision sites for minimally invasive tool access and the pose of robots to guarantee a collision-free operation throughout the intervention for coronary heart disease [67]. Furthermore, Sun *et al.* developed a computer-based simulator where the surgeons can virtually try the procedures in advance [68].

Several surgical planners also have been implemented to support current stereotactic surgery such as ablation, biopsy, stimulation, and implantation in the brain. For example, surgical planners automatically suggest the possible trajectories and insertion areas on the skull that minimize the surgical risk based on the preoperative MR scans of the patients [69], [70]. Then the suggested trajectories are accepted upon evaluation by neurosurgeons [71], [72]. As new surgical tools such as flexible needles are incorporated in stereotactic surgery, planning becomes less intuitive. This requires understandings of anatomical constraints as well as robot kinematics and dynamics, which is the subject of current research [73], [74].

# References

[1]  B. Davies, "A review of robotics in surgery," *Proc Inst Mech Eng H*, vol. 214, no. 1, pp. 129–140, 2000.

[2]  R. A. Beasley, "Medical robots: Current systems and research directions," *Journal of Robotics*, vol. 2012, 2012.

[3]  A. R. Lanfranco, A. E. Castellanos, J. P. Desai, and W. C. Meyers, "Robotic surgery: A current perspective," *Ann Surg*, vol. 239, no. 1, p. 14, 2004.

[4]  H. J. Marcus, C. A. Seneci, C. J. Payne, D. Nandi, A. Darzi, and G.-Z. Yang, "Robotics in keyhole transcranial endoscope-assisted microsurgery: A critical review of existing systems and proposed specifications for new robotic platforms," *Oper Neurosurg*, vol. 10, no. 1, pp. 84–96, 2013.

[5]  N. Nathoo, M. C. Çavuşoğlu, M. A. Vogelbaum, and G. H. Barnett, "In touch with robotics: Neurosurgery for the future," *Neurosurgery*, vol. 56, no. 3, pp. 421–433, 2005.

[6]  C. Faria, W. Erlhagen, M. Rito, E. De Momi, G. Ferrigno, and E. Bicho, "Review of robotic technology for stereotactic neurosurgery," *IEEE Rev Biomed Eng*, vol. 8, pp. 125–137, 2015.

[7]  D. F. Louw, T. Fielding, P. B. McBeth, D. Gregoris, P. Newhook, and G. R. Sutherland, "Surgical Robotics: A Review and Neurosurgical Prototype Development," *Neurosurgery*, vol. 54, no. 3, pp. 525–537, Mar. 2004, ISSN: 0148-396X.

[8]  H. Marcus, D. Nandi, A. Darzi, and G.-Z. Yang, "Surgical robotics through a keyhole: From today's translational barriers to tomorrow's disappearing robots," *IEEE Trans Biomed Eng*, vol. 60, no. 3, pp. 674–681, 2013.

[9]  R. D. Howe and Y. Matsuoka, "Robotics for surgery," *Annu Rev Biomed Eng*, vol. 1, no. 1, pp. 211–240, 1999.

[10]  J. J. Doulgeris, S. A. Gonzalez-Blohm, A. K. Filis, T. M. Shea, K. Aghayev, and F. D. Vrionis, "Robotics in neurosurgery: Evolution, current challenges, and compromises," *Cancer Control*, vol. 22, no. 3, pp. 352–359, 2015.

[11]  Y. S. Kwoh, J. Hou, E. A. Jonckheere, and S. Hayati, "A robot with improved absolute positioning accuracy for ct guided stereotactic brain surgery," *IEEE Trans Biomed Eng*, vol. 35, no. 2, pp. 153–160, 1988.

[12]  P. Mazzone, P. Arena, L. Cantelli, G. Spampinato, S. Sposato, S. Cozzolino, P. Demarinis, and G. Muscato, "Experimental new automatic tools for robotic stereotactic neurosurgery: Towards no hands procedure of leads implantation into a brain target," *J Neural Transm*, vol. 123, no. 7, pp. 737–750, 2016.

[13]  D. von Langsdorff, P. Paquis, and D. Fontaine, "In vivo measurement of the frame-based application accuracy of the neuromate neurosurgical robot," *J Neurosurgery*, vol. 122, no. 1, pp. 191–194, 2015.

[14] A. De Benedictis, A. Trezza, A. Carai, E. Genovese, E. Procaccini, R. Messina, F. Randi, S. Cossu, G. Esposito, P. Palma, *et al.*, "Robot-assisted procedures in pediatric neurosurgery," *Neurosurg focus*, vol. 42, no. 5, E7, 2017.

[15] T. Xia, C. Baird, G. Jallo, K. Hayes, N. Nakajima, N. Hata, and P. Kazanzides, "An integrated system for planning, navigation and robotic assistance for skull base surgery," *Int J Med Robot*, vol. 4, no. 4, pp. 321–330, Dec. 2008, ISSN: 14785951.

[16] Mazor Robotics, Available at: http://medical.olympusamerica.com/.

[17] M. Shoham, M. Burman, E. Zehavi, L. Joskowicz, E. Batkilin, and Y. Kunicher, "Bone-mounted miniature robot for surgical procedures: Concept and clinical applications," *IEEE Trans Robot Autom*, vol. 19, no. 5, pp. 893–901, 2003.

[18] C. J. Payne, H. J. Marcus, and G.-Z. Yang, "A smart haptic hand-held device for neurosurgical microdissection," *Ann Biomed Eng*, vol. 43, no. 9, pp. 2185–2195, 2015.

[19] G. Kane, G. Eggers, R. Boesecke, J. Raczkowsky, H. Wörn, R. Marmulla, and J. Mühling, "System design of a hand-held mobile robot for craniotomy," in *Med Image Comput Comput Assist Interv*, Springer, 2009, pp. 402–409.

[20] R. A. MacLachlan, B. C. Becker, J. C. Tabarés, G. W. Podnar, L. A. Lobes Jr, and C. N. Riviere, "Micron: An actively stabilized handheld tool for microsurgery," *IEEE Trans Rob*, vol. 28, no. 1, p. 195, 2012.

[21] C. J. Payne and G.-Z. Yang, "Hand-held medical robots," *Ann Biomed Eng*, vol. 42, no. 8, pp. 1594–1605, 2014.

[22] A. Korff, A. Follmann, T. Fürtjes, D. Habor, S. C. Kunze, K. Schmieder, and K. Radermacher, "Concept and evaluation of a synergistic controlled robotic instrument for trepanation in neurosurgery," in *IEEE Int Conf Robot Autom*, IEEE, 2011, pp. 6258–6263.

[23] G. R. Sutherland, S. Wolfsberger, S. Lama, and K. Zarei-nia, "The evolution of neuroarm," *Neurosurgery*, vol. 72, no. suppl_1, A27–A32, 2013.

[24] M. Cianchetti, T. Ranzani, G. Gerboni, T. Nanayakkara, K. Althoefer, P. Dasgupta, and A. Menciassi, "Soft robotics technologies to address shortcomings in today's minimally invasive surgery: The stiff-flop approach," *Soft Robot*, vol. 1, no. 2, pp. 122–131, 2014.

[25] N. Simaan, R. Taylor, and P. Flint, "High dexterity snake-like robotic slaves for minimally invasive telesurgery of the upper airway," in *Med Image Comput Comput Assist Interv*, Springer, 2004, pp. 17–24.

[26] G. R. Sutherland, P. B. McBeth, and D. F. Louw, "Neuroarm: An mr compatible robot for microsurgery," in *Int Congr Ser*, Elsevier, vol. 1256, 2003, pp. 504–508.

[27] G. R. Sutherland, S. Lama, L. S. Gan, S. Wolfsberger, and K. Zareinia, "Merging machines with microsurgery: Clinical experience with neuroarm," *J Neurosurg*, vol. 118, no. 3, pp. 521–529, 2013.

[28] Y. Maddahi, K. Zareinia, L. S. Gan, C. Sutherland, S. Lama, and G. R. Sutherland, "Treatment of glioma using neuroarm surgical system," *Biomed Res Int*, vol. 2016, 2016.

[29] G. T. Sung and I. S. Gill, "Robotic laparoscopic surgery: A comparison of the da vinci and zeus systems," *Urology*, vol. 58, no. 6, pp. 893–898, 2001.

[30] P. Modi, E. Rodriguez, and W. R. Chitwood Jr, "Robot-assisted cardiac surgery," *Interact Cardiovasc Thorac Surg*, vol. 9, no. 3, pp. 500–505, 2009.

[31] Intuitive Surgical Inc, Available at: https://www.intuitivesurgical.com/.

[32] H. J. Marcus, A. Hughes-Hallett, T. P. Cundy, G.-Z. Yang, A. Darzi, and D. Nandi, "Da vinci robot-assisted keyhole neurosurgery: A cadaver study on feasibility and safety," *Neurosurg Rev*, vol. 38, no. 2, pp. 367–371, 2015.

[33] J. Burgner-Kahrs, D. C. Rucker, and H. Choset, "Continuum robots for medical applications: A survey," *IEEE Trans Rob*, vol. 31, no. 6, pp. 1261–1280, 2015.

[34] StereoTaxis NIOBE, Available at: http://www.stereotaxis.com/.

[35] F. Carpi and C. Pappone, "Stereotaxis niobe® magnetic navigation system for endocardial catheter ablation and gastrointestinal capsule endoscopy," *Expert Rev Med Devices*, vol. 6, no. 5, pp. 487–498, 2009.

[36] T. Krings, J. Finney, P. Niggemann, P. Reinacher, N. Lück, A. Drexler, J. Lovell, A. Meyer, R. Sehra, P. Schauerte, *et al.*, "Magnetic versus manual guidewire manipulation in neuroradiology: In vitro results," *Neuroradiology*, vol. 48, no. 6, pp. 394–401, 2006.

[37] T. Kara, P. Leinveber, M. Vlasin, P. Jurak, M. Novak, Z. Novak, J. Chrastina, K. Czechowicz, M. Belehrad, S. J. Asirvatham, *et al.*, "Endovascular brain intervention and mapping in a dog experimental model using magnetically-guided micro-catheter technology," *Biomed Pap Med Fac Univ Palacky Olomouc Czech Repub*, vol. 158, no. 2, pp. 221–226, 2014.

[38] E. J. Butler, R. Hammond-Oakley, S. Chawarski, A. H. Gosline, P. Codd, T. Anor, J. R. Madsen, P. E. Dupont, and J. Lock, "Robotic neuro-endoscope with concentric tube augmentation," in *IEEE/RSJ Int Conf Intelligent Robots and Systems*, IEEE, 2012, pp. 2941–2946.

[39] J. Burgner, P. J. Swaney, R. A. Lathrop, K. D. Weaver, and R. J. Webster, "Debulking from within: A robotic steerable cannula for intracerebral hemorrhage evacuation," *IEEE Trans Biomed Eng*, vol. 60, no. 9, pp. 2567–2575, 2013.

[40] C. Bergeles, A. H. Gosline, N. V. Vasilyev, P. J. Codd, J. Pedro, and P. E. Dupont, "Concentric tube robot design and optimization based on task and anatomical constraints," *IEEE Trans Rob*, vol. 31, no. 1, pp. 67–84, 2015.

[41] J. A. Engh, D. S. Minhas, D. Kondziolka, and C. N. Riviere, "Percutaneous intracerebral navigation by duty-cycled spinning of flexible bevel-tipped needles," *Neurosurgery*, vol. 67, no. 4, pp. 1117–1123, 2010.

[42] N. J. van de Berg, J. Dankelman, and J. J. van den Dobbelsteen, "Design of an actively controlled steerable needle with tendon actuation and FBG-based shape sensing," *Med Eng Phys*, vol. 37, no. 6, pp. 617–622, 2015.

[43] A. J. Petruska, F. Ruetz, A. Hong, L. Regli, O. Sürücü, A. Zemmar, and B. J. Nelson, "Magnetic needle guidance for neurosurgery: Initial design and proof of concept," in *IEEE Int Conf Robot Autom*, May 2016, pp. 4392–4397.

[44] K. B. Reed, A. Majewicz, V. Kallem, R. Alterovitz, K. Goldberg, N. J. Cowan, and A. M. Okamura, "Robot-assisted needle steering," *IEEE Robot Autom Mag*, vol. 18, no. 4, pp. 35–46, 2011.

[45] S. Y. Ko, L. Frasson, and F. R. y Baena, "Closed-loop planar motion control of a steerable probe with a programmable bevel inspired by nature," *IEEE Trans on Rob*, vol. 27, no. 5, pp. 970–983, 2011.

[46] L. K. Wagner, P. J. Eifel, and R. A. Geise, "Potential biological effects following high X-ray dose interventional procedures," *J Vasc Interv Radiol*, vol. 5, no. 1, pp. 71–84, 1994.

[47] A. Talukdar and D. Wilson, "Modeling and optimization of rotational C-arm stereoscopic X-ray angiography," *IEEE Trans Med Imaging*, vol. 18, no. 7, pp. 604–616, Jul. 1999.

[48] H. Shirato, S. Shimizu, K. Kitamura, T. Nishioka, K. Kagei, S. Hashimoto, H. Aoyama, T. Kunieda, N. Shinohara, H. Dosaka-Akita, *et al.*, "Four-dimensional treatment planning and fluoroscopic real-time tumor tracking radiotherapy for moving tumor," *Int J Radiat Oncol Biol Phys*, vol. 48, no. 2, pp. 435–442, 2000.

[49] D. Glozman and M. Shoham, "Image-guided robotic flexible needle steering," *IEEE Trans Rob*, vol. 23, no. 3, pp. 459–467, 2007.

[50] A. Vandini, C. Bergeles, B. Glocker, P. Giataganas, and G.-Z. Yang, "Unified tracking and shape estimation for concentric tube robots," *IEEE Trans Rob*, vol. 33, no. 4, pp. 901–915, 2017.

[51] S. Nazarian, A. Kolandaivelu, M. M. Zviman, G. R. Meininger, R. Kato, R. C. Susil, A. Roguin, T. L. Dickfeld, H. Ashikaga, H. Calkins, *et al.*, "Feasibility of real-time magnetic resonance imaging for catheter guidance in electrophysiology studies," *Circ Arrhythm Electrophysiol*, vol. 118, no. 3, pp. 223–229, 2008.

[52] P. S. Larson, P. A. Starr, G. Bates, L. Tansey, R. M. Richardson, and A. J. Martin, "An optimized system for interventional magnetic resonance imaging-guided stereotactic surgery: Preliminary evaluation of targeting accuracy," *Operative Neurosurgery*, vol. 70, ons95–ons103, 2011.

[53] M. K. Feldman, S. Katyal, and M. S. Blackwood, "Us artifacts," *Radiographics*, vol. 29, no. 4, pp. 1179–1189, 2009.

[54] T. Selbekk, A. S. Jakola, O. Solheim, T. F. Johansen, F. Lindseth, I. Reinertsen, and G. Unsgård, "Ultrasound imaging in neurosurgery: Approaches to minimize surgically induced image artefacts for improved resection control," *Acta Neurochir*, vol. 155, no. 6, pp. 973–980, 2013.

[55] S. Harris, F. Arambula-Cosio, Q. Mei, R. Hibberd, B. Davies, J. Wickham, M. Nathan, and B. Kundu, "The Probot-an active robot for prostate resection," *Proc Inst Mech Eng H*, vol. 211, no. 4, pp. 317–325, 1997.

[56] T. K. Adebar, A. E. Fletcher, and A. M. Okamura, "3D ultrasound-guided robotic needle steering in biological tissue," *IEEE Trans Biomed Eng*, vol. 61, no. 12, pp. 2899–2910, 2014.

[57] M. Abayazid, G. J. Vrooijink, S. Patil, R. Alterovitz, and S. Misra, "Experimental evaluation of ultrasound-guided 3D needle steering in biological tissue," *Int J Comput Assist Radiol Surg*, vol. 9, no. 6, pp. 931–939, 2014.

[58] A. M. Franz, T. Haidegger, W. Birkfellner, K. Cleary, T. M. Peters, and L. Maier-Hein, "Electromagnetic Tracking in Medicine - a Review of Technology, Validation and Applications," *IEEE Trans Med Imaging*, vol. 33, no. 8, pp. 1702–1725, 2014.

[59] Z. Yaniv, E. Wilson, D. Lindisch, and K. Cleary, "Electromagnetic tracking in the clinical environment," *Med Phys*, vol. 36, no. 3, pp. 876–892, 2009.

[60] Northern Digital Inc., Available at: https://www.ndigital.com/medical/.

[61] Polhemus Inc, Available at: https://polhemus.com/.

[62] Olympus ScopeGuide, Available at: http://medical.olympusamerica.com/.

[63] Z. Lunwei, Q. Jinwu, S. Linyong, and Z. Yanan, "FBG sensor devices for spatial shape detection of intelligent colonoscope," in *IEEE Int Conf Robot Autom*, IEEE, vol. 1, 2004, pp. 834–840.

[64] K. R. Henken, J. Dankelman, J. J. van den Dobbelsteen, L. K. Cheng, and M. S. van der Heiden, "Error analysis of fbg-based shape sensors for medical needle tracking," *IEEE ASME Trans Mechatron*, vol. 19, no. 5, pp. 1523–1531, 2014.

[65] R. J. Roesthuis, N. J. van de Berg, J. J. van den Dobbelsteen, and S. Misra, "Modeling and steering of a novel actuated-tip needle through a soft-tissue simulant using fiber bragg grating sensors," in *IEEE Int Conf Robot Autom*, IEEE, 2015, pp. 2283–2289.

[66] Renishaw NeuroMate, Available at: https://www.renishaw.com/.

[67] L. Adhami and È. Coste-Manière, "Optimal planning for minimally invasive surgical robots," *IEEE Trans Robot Autom*, vol. 19, no. 5, pp. 854–863, 2003.

[68] L.-W. Sun, F. Van Meer, J. Schmid, Y. Bailly, A. A. Thakre, and C. K. Yeung, "Advanced da vinci surgical system simulator for surgeon training and operation planning," *Int J Med Robot*, vol. 3, no. 3, pp. 245–251, 2007.

[69] E. J. Brunenberg, A. Vilanova, V. Visser-Vandewalle, Y. Temel, L. Ackermans, B. Platel, and B. M. ter Haar Romeny, "Automatic trajectory planning for deep brain stimulation: A feasibility study," in *Med Image Comput Comput Assist Interv*, 2007, pp. 584–592.

[70]  C. Essert, C. Haegelen, F. Lalys, A. Abadie, and P. Jannin, "Automatic computation of electrode trajectories for deep brain stimulation: A hybrid symbolic and numerical approach," *Int J Comput Assist Radiol Surg*, vol. 7, no. 4, pp. 517–532, 2012.

[71]  S. Bériault, F. Al Subaie, D. L. Collins, A. F. Sadikot, and G. B. Pike, "A multimodal approach to computer-assisted deep brain stimulation trajectory planning," *Int J Comput Assist Radiol Surg*, vol. 7, no. 5, pp. 687–704, 2012.

[72]  Y. Liu, P. E. Konrad, J. S. Neimat, S. B. Tatter, H. Yu, R. D. Datteri, B. A. Landman, J. H. Noble, S. Pallavaram, B. M. Dawant, *et al.*, "Multisurgeon, multisite validation of a trajectory planning algorithm for deep brain stimulation procedures," *IEEE Trans Biomed Eng*, vol. 61, no. 9, pp. 2479–2487, 2014.

[73]  S. Bano, S. Y. Ko, and F. R. y Baena, "Smooth path planning for a biologically-inspired neurosurgical probe," in *Conf Proc IEEE Eng Med Biol Soc*, IEEE, 2012, pp. 920–923.

[74]  S. Patil, J. Burgner, R. J. Webster, and R. Alterovitz, "Needle steering in 3-D via rapid replanning," *IEEE Trans Rob*, vol. 30, no. 4, pp. 853–864, 2014.

# Chapter 3

# Fluoroscopic Tracking
# for Minimally Invasive Tools

An accurate and efficient tracking method is important to precisely guide minimally invasive tools in real-time. The required accuracy depends on the specific clinical applications. For example, a coil embolization of a small neck aneurysm requires a position resolution better than 4 mm [1], and navigation into the neurological vascular system requires resolution on the order of 1 mm [2]. Among non-invasive imaging techniques such as projective X-ray fluoroscopy, ultrasound, electromagnetic tracking, CT, and MRI, fluoroscopy is a promising solution for remote manipulation for minimally invasive tools because it provides sufficient frame rates and resolution. However, the primary drawbacks of fluoroscopy are that the images are only in 2D and it exposes both the patients and surgeons to radiation [3].

To overcome the 2D nature of single-axis fluoroscopy, C-Arm fluoroscopy offers projections from various angles, and biplanar fluoroscopy provides two perpendicular projections. Talukdar *et al.* [4] modeled stereoscopy with a rotational C-Arm and optimized the geometric parameters for different clinical procedures. Bourantas *et al.* [5], [6] reconstructed the 3D path of a catheter using biplanar fluoroscopy and intravascular ultrasound images. Direct 3D catheter localization from a single fluoroscopic image can be achieved by incorporating catheter size information [7]. Using this technique, Yatziv *et al.* [8] tracked multiple catheters for cardiac ablation in a 3D space.

In this chapter, a fluoroscopic tracking method for minimally invasive tools is proposed. By using sequentially rotated views, the method can improve the

level of position accuracy while reducing the radiation exposure compared to biplanar fluoroscopy. In section 3.1, the procedure to extract the 3D position of the object from a single fluoroscopic image is briefly revisited and the covariance of this estimate is numerically analyzed and discussed. In section 3.2, a solution for combining a series of position estimates from multiple views using a Kalman filter is proposed. The method is validated using sequential fluoroscopic views of cardiac ablation catheters in section 3.3 and DBS electrodes in section 3.4

## 3.1 Localization Using a Single View

### 3.1.1 Position Estimation

It has been shown by Fallavollita [7] that the 3D position of an object can be extracted from a single 2D fluoroscopic image. A direct relationship between catheter's depth and its width or area measured in image is suggested. Given the C-Arm fluoroscopic imaging geometry shown in Figure 3.1, the procedure is as follows. The 3D position in the C-Arm imaging space $\mathbf{P}^c = [x^c \ y^c \ z^c]^T$ of an object is a function of the tip's width $\delta_o$ [mm], the imaged width $\delta_i$ [pixels], and the tip's fluoroscopic image position $\mathbf{P}^I = [u, v]^T$ [pixels]. The horizontal position $(x^c, y^c)$ of the object is given by

$$\begin{bmatrix} x^c \\ y^c \end{bmatrix} = \frac{\delta_o}{\delta_i} \begin{bmatrix} u - \frac{w}{2} \\ v - \frac{h}{2} \end{bmatrix}, \tag{3.1}$$

where the width and the height of the image is $w$ and $h$ in pixels, respectively. The vertical position $z^c$ is also linear to the ratio of object size $\delta_o$ and projected size $\delta_i$

$$z^c = \frac{L}{p_s} \frac{\delta_o}{\delta_i} - L_c, \tag{3.2}$$

where $p_s$ is the physical pixel size in millimeters, $L$ is the distance between the source and image, and $L_c$ is the distance between the source and the origin of the C-arm coordinate frame.

By rotating the C-Arm, the position of the object changes with respect to the C-Arm imaging coordinate system. Taking the origin of the world frame and the fluoroscopic imaging coordinates to be at the center of the rotating axis of the C-Arm, the world frame position $\mathbf{P}$ as a function of the C-Arm rotation matrix $R_c$ and imaging frame position $\mathbf{P}^c$ is

$$\mathbf{P} = R_c \mathbf{P}^c. \tag{3.3}$$
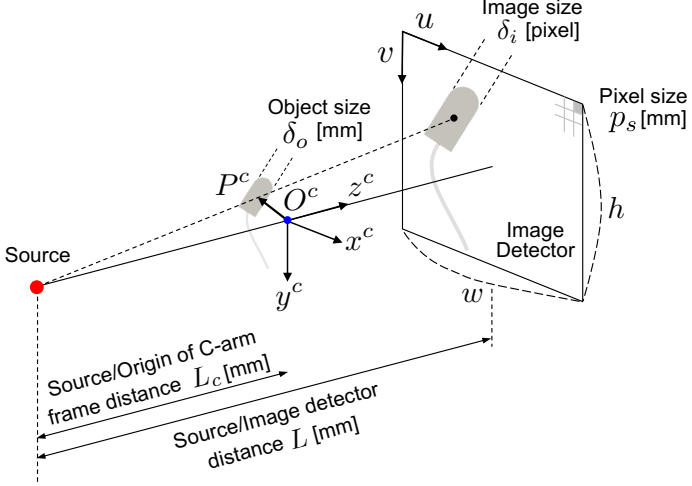
Figure 3.1 : Geometry of a C-Arm fluoroscope with a flat panel detector. The depth $z^c$ can be estimated from the object size $\delta_o$, the projected image size $\delta_i$, the pixel size $p_s$, the distance $L$ between the X-ray source and the detector, and the distance $L_c$ between the source and the origin of the C-Arm frame. The position of the object tip in the fluoroscope image plane is $(u, v)$, and the image width is $w$ and height is $h$.

### 3.1.2 Covariance Estimation

The calculated 3D position $\mathbf{P^c}$ differs from the actual position due to errors in the measured quantities $u$, $v$, and $\delta_i$ arising from noise in the fluoroscopic image, inaccuracies in the C-Arm geometry, and error prone segmentation methods. In this section, we investigate the effect of image-based errors on the uncertainty of 3D position estimation.

Let the covariance matrix of image-based measurements $[u\ v\ \delta_i]$ be denoted by $M^I$ as

$$M^I = \begin{bmatrix} \sigma_u^2 & \sigma_{uv} & \sigma_{u\delta_i} \\ \sigma_{uv} & \sigma_v^2 & \sigma_{v\delta_i} \\ \sigma_{u\delta_i} & \sigma_{v\delta_i} & \sigma_{\delta_i}^2 \end{bmatrix}. \tag{3.4}$$

The measurement variances $\sigma_u^2$, $\sigma_v^2$, and $\sigma_{\delta_i}^2$ can be obtained by analyzing several images taken at the same object's pose and C-Arm configuration. These variances are consistent with the C-Arm configuration. The cross-covariance terms $\sigma_{uv}$, $\sigma_{u\delta_i}$, and $\sigma_{v\delta_i}$ are zero because the three variables are independent and uncorrelated in the image space.

For a given covariance matrix $M^I$ and position $\mathbf{P^c}$ as a function of $(u,\ v,\ \delta_i)$, the covariance matrix $M^{\mathbf{P^c}}$ is calculated from error propagation [9] as

$$M^{\mathbf{P^c}} = JM^I J^T \tag{3.5}$$

where the transformation Jacobian is given as the partial derivatives of (3.1) and (3.2) as

$$J = \begin{bmatrix} \dfrac{\partial \mathbf{P^c}}{\partial u} & \dfrac{\partial \mathbf{P^c}}{\partial v} & \dfrac{\partial \mathbf{P^c}}{\partial \delta_i} \end{bmatrix} = \begin{bmatrix} \dfrac{\delta_o}{\delta_i} & 0 & -\dfrac{\delta_o}{\delta_i^2}(u - \dfrac{w}{2}) \\[2ex] 0 & \dfrac{\delta_o}{\delta_i} & -\dfrac{\delta_o}{\delta_i^2}(v - \dfrac{h}{2}) \\[2ex] 0 & 0 & -\dfrac{L}{p_s}\dfrac{\delta_o}{\delta_i^2} \end{bmatrix}. \tag{3.6}$$

Therefore, the covariance matrix $\Sigma^{\mathbf{P^c}}$ is obtained as

$$M^{\mathbf{P^c}} = \begin{bmatrix} M_{11} & M_{12} & M_{13} \\ M_{12} & M_{22} & M_{23} \\ M_{13} & M_{23} & M_{33} \end{bmatrix} \tag{3.7}$$

where

$$M_{11} = \left(\frac{\delta_o}{\delta_i}\right)^2 \sigma_u^2 + \left(u - \frac{w}{2}\right)^2 \left(\frac{\delta_o}{\delta_i^2}\right)^2 \sigma_{\delta_i}^2$$

$$M_{12} = (u - \frac{w}{2})(v - \frac{h}{2})\left(\frac{\delta_o}{\delta_i^2}\right)^2 \sigma_{\delta_i}^2$$

$$M_{13} = (u - \frac{w}{2})\frac{L}{p_s}\left(\frac{\delta_o}{\delta_i^2}\right)^2 \sigma_{\delta_i}^2$$

$$M_{22} = \left(\frac{\delta_o}{\delta_i}\right)^2 \sigma_v^2 + \left(v - \frac{h}{2}\right)^2 \left(\frac{\delta_o}{\delta_i^2}\right)^2 \sigma_{\delta_i}^2$$

$$M_{23} = (v - \frac{h}{2})\frac{L}{p_s}\left(\frac{\delta_o}{\delta_i^2}\right)^2 \sigma_{\delta_i}^2$$

$$M_{33} = \left(\frac{L}{p_s}\right)^2 \left(\frac{\delta_o}{\delta_i^2}\right)^2 \sigma_{\delta_i}^2.$$

The position of the object with respect to the world frame is obtained using a linear equation (3.3) and the covariance matrix $M$ becomes

$$M = R_c M^{\mathbf{P^c}} R_c^T. \tag{3.8}$$
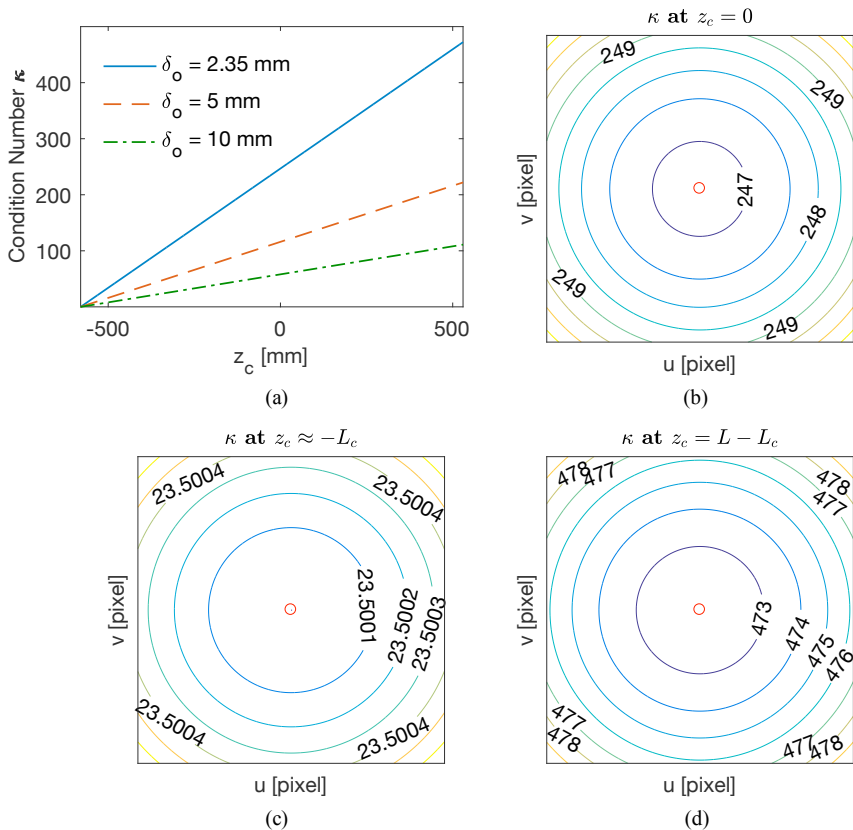
Figure 3.2 : Effects of an object position on condition number $\kappa$ of the covariance matrix $M^{\mathbf{P^c}}$. (a) Condition number $\kappa$ following various objects with different physical sizes. (b-d) Distribution of $\kappa$ in image plane at differenct $z_c$.

The 3D position is extracted from a single fluoroscopic image, and its uncertainties are related to the errors in image-based measurements. It is natural to have higher uncertainties in the out-of-image direction than the in-image direction. To study the directional uncertainties of final 3D position estimates, the condition number $\kappa$ is defined as

$$\kappa = \sqrt{\frac{\lambda_{\max}(M^{\mathbf{P^c}})}{\lambda_{\min}(M^{\mathbf{P^c}})}} \tag{3.9}$$

indicating the ratio of the largest to the smallest standard deviations of the estimates.

Suppose the object is at the center of the image, therefore, $(u, \ v) = (\frac{w}{2}, \ \frac{h}{2})$ and the variances $\sigma_u^2$, $\sigma_v^2$, and $\sigma_{\delta_i}^2$ are the same as $\sigma^2$. The covariance matrix becomes

$$M^{\mathbf{Pc}} = \left(\frac{\delta_o}{\delta_i}\right)^2 \begin{bmatrix} 1 & 0 & 0 \\ 0 & 1 & 0 \\ 0 & 0 & \frac{L^2}{\delta_i^2 p_s^2} \end{bmatrix} \sigma^2, \tag{3.10}$$

and $\kappa$ exhibits linear growth with $\frac{L}{p_s \delta_i}$. Using the system parameters reported later in section 3.3, the estimation error in the out-of-image direction is about 250 times larger than the error in the imaging plane when the object is located near the center of the C-Arm frame. The condition number varies depending on object's physical size and the distance $z_c$ shown in Figure 3.2 (a). As the object gets closer to the X-ray source and its physical size gets bigger, X-ray projects a larger area in the detector which results in a better estimation of $\delta_i$.

This condition number also depends on the object's location in the image plane as shown in Figure 3.2 (b-d). The estimation errors in the depth direction are smaller when the object is closer to the center of the image plane. As $z_c$ increases, the difference of the condition number within the image plane gets larger. Therefore, the condition number depends highly on the depth of the object, and slightly on the location of the object in the image plane.

## 3.2 Combining Multiple Views

The depth calculation is significantly more sensitive to noise than the horizontal position estimate. Thus, the uncertainty in that world frame direction can be significantly larger than the other two directions. Rotating the C-Arm changes the direction of the most uncertain axis, as depicted in Figure 3.3, and allows for a sequentially refined estimate. To fuse position estimates from sequential images, we propose using a Kalman filter, and acknowledge that the Gaussian noise assumption is violated. The actual distribution cannot be Gaussian because of the nonlinear transformation between the image space and the world position, and because the object's projected width cannot be negative. The inaccuracy in this assumption will primarily affect our estimate covariance but should not significantly affect our estimated position, because the actual probability distributions are fundamentally monomodal. Since the Kalman filter is a
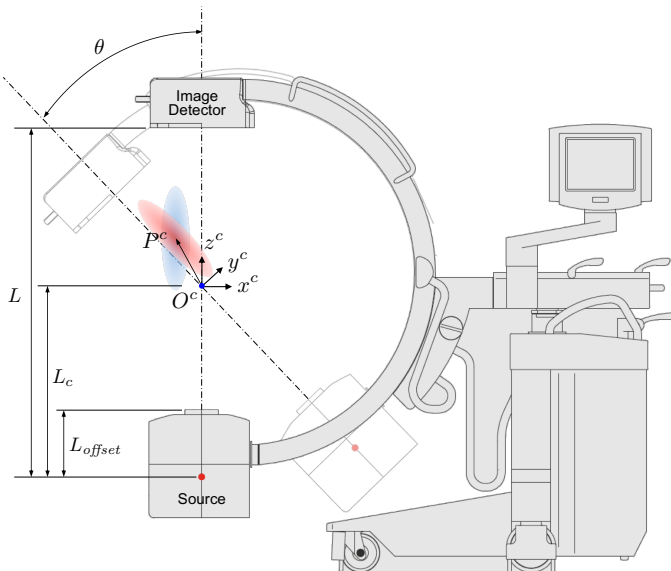
Figure 3.3 : Uncertainty ellipsoids of the position estimates at different C-Arm configurations. Image adapted from Ziehm Imaging (Nürnberg, Germany).

least squares-based method [10], it will eventually converge to the correct values even if the individual sample weightings are slightly inaccurate.

Posing our problem in a Kalman filter sense, we take the system state as **P**, which is the position of a catheter tip in world frame, and assume it evolves quasi-statically. Specifically, we assume the state transition matrix is the identity and there is no command input. Thus, any deviation between the measurement and the estimate are solely due to the measurement noise $m$. The process noise $n$ is taken to be small (approximately 1 mm) to account for any accidental disturbance of the catheter pose while rotating the C-Arm. The measured output **Q** is obtained from (3.3) and the measurement noise $m$ with covariance matrix $M$ is obtained from (3.8).

The Kalman filter is a recursive estimation method and works with two steps, the prediction step and the update step [11]. In the prediction step, the current state of the system is predicted with the previous state along with the uncertainties. Then in the update step, the current prediction is combined with the

current observation to update the state estimate.

For our system, the Kalman filter equations are described as follows:

$$\text{prediction:} \quad \hat{\mathbf{P}}_k^{\dagger} = \hat{\mathbf{P}}_{k-1} \tag{3.11}$$

$$\Sigma_k^{\dagger} = \Sigma_{k-1} + N \tag{3.12}$$

$$\text{update:} \quad \mathbf{K}_k = \Sigma_k^{\dagger}(\Sigma_k^{\dagger} + M)^{-1} \tag{3.13}$$

$$\hat{\mathbf{P}}_k = \hat{\mathbf{P}}_k^{\dagger} + \mathbf{K}_k(\mathbf{Q}_k - \hat{\mathbf{P}}_k^{\dagger}) \tag{3.14}$$

$$\Sigma_k = \Sigma_k^{\dagger} - \mathbf{K}_k \Sigma_k^{\dagger}. \tag{3.15}$$

Here, $\hat{\mathbf{P}}_k^{\dagger}$ and $\Sigma_k^{\dagger}$ are the estimates of the state and the covariance matrix, respectively, before the measurement is incorporated. The Kalman gain $\mathbf{K}_k$ must be recalculated at each step because the measurement covariance is not constant since the C-Arm rotates. With the updated gain, the estimate of the current sate $\hat{\mathbf{P}}_k$ and the covariance matrix $\Sigma_k$ are updated.

## 3.3 Tracking Ablation Catheters

### 3.3.1 Experimental Setup

We use a C-Arm fluoroscope from Ziehm Imaging (Nürnberg, Germany [12]) which offers images free of magnetic distortion due to its flat-panel detector. The catheter used in the experiments is designed for cardiac ablation from Biosense Webster (Irvine, CA, USA [13]). The physical parameters for fluoroscope and catheter are provided in Table 3.1.

Table 3.1 : PHYSICAL PARAMETERS OF THE EXPERIMENTAL SETUP

| Geomety | | Calibration | |
|---|---|---|---|
| $L$ | 1110 mm | $L/p_s$ | 5830 pixel |
| $L_{\text{offset}}$ | 215 mm | $L_{\text{offset}}$ | 217 mm |
| $L_c$ | 580 mm | | |
| $w$, $h$ | 1024 pixel | | |
| $p_s$ | 0.195 mm/pixel | | |
| $\delta_o$ | 2.35 mm | | |

### 3.3.2 Calibration

To calibrate the constants in (3.2) for our system, we used fluoroscopic images of the asymmetrical circle pattern at different distances from the X-ray source shown in Figure 3.4 (a). The depth is measured from the top of the generator to the object, which is $z_m^c = z^c + L_c - L_{offset}$. Based on the geometry of the C-Arm and (3.2), the fitting curve follows

$$z_m^c = \frac{L}{p_s} \frac{\delta_o}{\delta_i} - L_{offset}. \tag{3.16}$$

The least-squares fit of (3.16) to the data is shown in Figure 3.4 (b), and the fit curve is found to be

$$z^c = 5830 \frac{\delta_o}{\delta_i} - 217 \tag{3.17}$$

with an $R^2$ value of 0.9999. The coefficients $\frac{L}{p_s}$ and $L_{offset}$ have a 2.58% and 0.93% error, respectively, as compared to the expected values from the reported C-Arm geometry. We use (3.17) to estimate the depth of the object in the tracking experiments.

To find the image position $\mathbf{P}^I$ and the width $\delta_i$, the tip is segmented with an empirically determined threshold. Then, $\mathbf{P}^I$ is computed as the centroid of the segmented catheter tip and the width is estimated by using the covariance of the tip points. To characterize the measurement noise of this method, ten images are taken at each of eight distinct poses for a total of eighty fluoroscopic images. The covariance of $u$, $v$, and $\delta_i$ are calculated based on this sample set. The measurement covariance for the image parameters $M^I$, measured in pixels, is

$$cov([u \ v \ \delta_i]^T) = \begin{bmatrix} 0.0241 & 0.0046 & -0.0006 \\ 0.0046 & 0.0241 & -0.0006 \\ -0.0006 & -0.0006 & 0.0796 \end{bmatrix}. \tag{3.18}$$

The off-diagonal covariances are negligible as discussed in 3.1.2, and the variances are

$$\sigma_u^2 = \sigma_v^2 = 0.024 \text{ and } \sigma_{\delta_i}^2 = 0.080. \tag{3.19}$$

Because the dynamics of the system is not considered, we assume the process
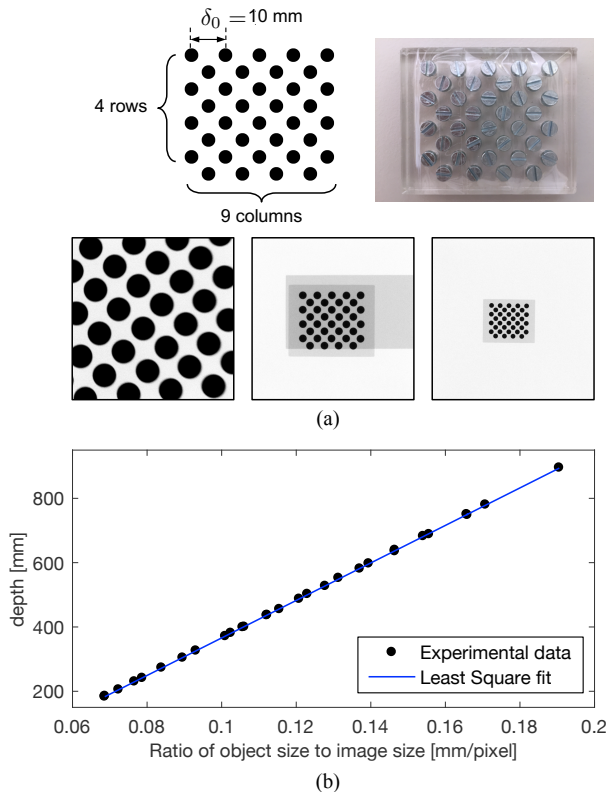
Figure 3.4 : Depth Calibration with an asymmetrical circle pattern. (a) Asymmetrical $4\times9$ circle pattern for calibration, with the object size $\delta_o=10$ mm. Fluoroscope images of the pattern at different distances from the X-ray source, $z_m^c = \{0, 455, 895\}$ mm from left to right. (b) Measured depth as a function of object-size to image-size ratio $\frac{\delta_o}{\delta_i}$. The blue line shows the least squares linear fit and the average error of $\frac{\delta_o}{\delta_i}$ was $9.65 \times 10^{-4}$.

noise, measured in millimeters, is as small as

$$N = \begin{bmatrix} 1 & 0 & 0 \\ 0 & 1 & 0 \\ 0 & 0 & 1 \end{bmatrix}. \tag{3.20}$$

To initialize the filter, the first measured position and measurement covariance are taken as the initial state $\mathbf{P}_0$ and the initial estimate covariance as $\Sigma_0$,

Table 3.2 : Measured Ground-Truth Position.

|  | Reference Position $\mathbf{P}^r$ [mm] | | |
|---|---|---|---|
|  | **x** | **y** | **z** |
| **pose 1** | -17.5 | -10.0 | -21.0 |
| **pose 2** | -16.0 | 2.0 | 58.0 |
| **pose 3** | -3.6 | 26.9 | 126.2 |
| **pose 4** | -3.6 | 25.5 | 73.2 |
| **pose 5** | -4.4 | 26.5 | 39.2 |

respectively.

### 3.3.3 Results

#### 3.3.3.1 Tracking performance with a rotating C-Arm

Five catheter positions were estimated to demonstrate the proposed approach. Fluoroscope images of the catheter tip were obtained with different configurations of the C-Arm, by rotating about the C-Arm's $x$-axis from $-45°$ to $45°$ (see Figure 3.5). Images for the poses 1 and 2 were obtained with 15° increments, and for the poses 3 to 5 increments of 7.5° were used. In some configurations, the catheter tip left the field of view of the imaging system as the C-Arm rotated. The number of sequential poses used to calculate the position for these positions was reduced accordingly.

The estimated position, using the proposed localization approach is shown in Table 3.4. The standard deviations for the estimates are calculated from the covariance matrix $\Sigma_k$, and we consider the diagonal entries as variances in the world frame. The square root of these values are the standard deviations.

The results were compared with the manually measured position of the catheter tip $\mathbf{P}^r$ in Table 3.2 and the estimated position $\mathbf{P}^c$ with a single image at $\theta = 0°$ in Table 3.3. The standard deviation of the estimated position $\mathbf{P}^c$ was computed as the square root of singular values for $M^{\mathbf{P^c}}$ in (3.7).

The proposed approach gives the mean estimation error for five poses as 13.9 mm in 3D space and 8.8 mm in depth compared to the manually measured position, while $\mathbf{P}^c$ from a single image gives 14.7 mm mean error in 3D and 14.4 mm in depth. These uncertainties are similar to the values reported by Fallavollita [7]. As discussed in 3.2, the error in the initial out-of-image-plane
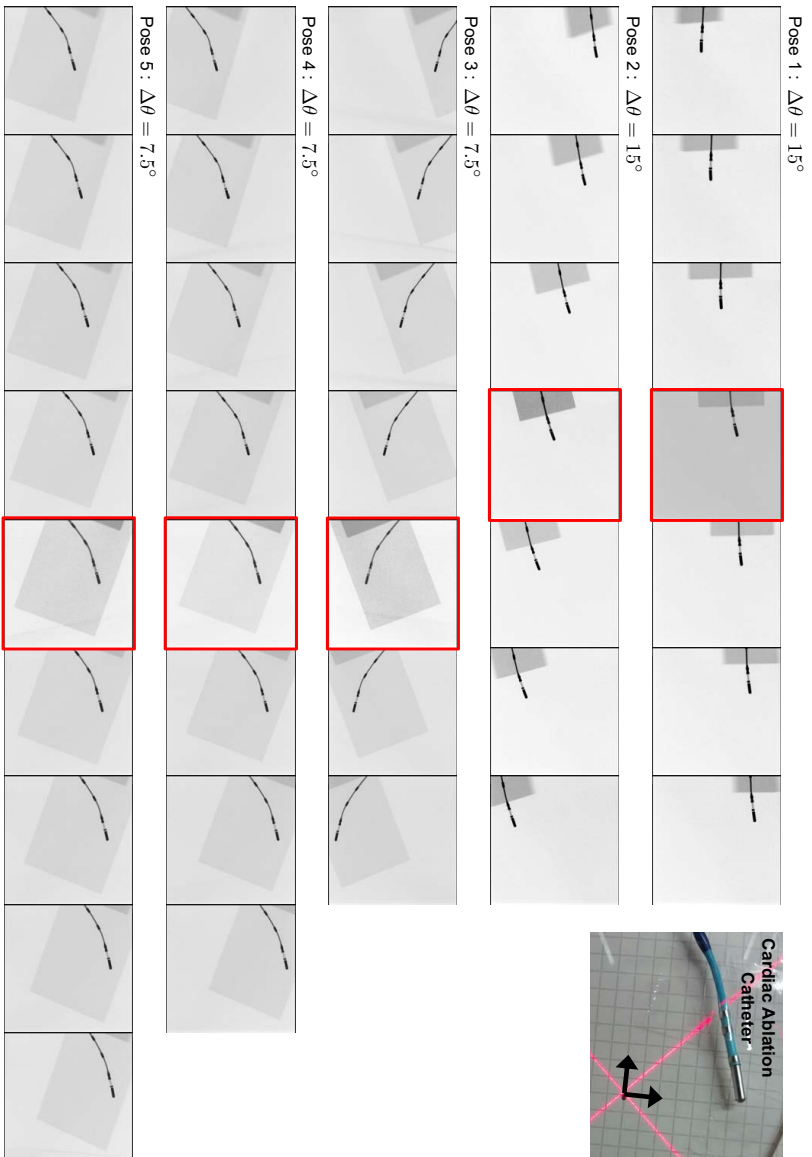
Figure 3.5 : Fluoroscope images of the catheter tip in five different poses captured at different configurations of the C-Arm. The catheter remains at its stationary position while the C-Arm rotates. Images captured at $\theta = 0$ is indicated with a red box.

Table 3.3 : ESTIMATED POSITION $P^c$ USING A SINGLE IMAGE AT $\theta = 0°$.

| | Estimated Position $\mathbf{P}^c$ [mm] | | | Error $\|\mathbf{P}^c - \mathbf{P}^r\|$ [mm] |
|---|---|---|---|---|
| | **x** | **y** | **z** | |
| **pose 1** | -17.7 ± 0.20 | -14.6 ± 0.16 | -31.8 ± 6.09 | 11.7 |
| **pose 2** | -15.8 ± 0.20 | 1.5 ± 0.03 | 29.6 ± 7.53 | 28.4 |
| **pose 3** | -3.4 ± 0.05 | 25.1 ± 0.37 | 136.6 ± 10.39 | 10.6 |
| **pose 4** | -3.6 ± 0.05 | 24.5 ± 0.33 | 61.8 ± 8.34 | 11.4 |
| **pose 5** | -3.6 ± 0.05 | 24.7 ± 0.31 | 28.1 ± 7.49 | 11.3 |

Table 3.4 : ESTIMATED POSITION $\hat{P}$ COMBINING MULTIPLE IMAGES WITH A KALMAN FILTER.

| pose | $\mathbf{\Delta\theta}$ [°] | Estimated Position $\hat{\mathbf{P}}$ [mm] | | | Error $\|\hat{\mathbf{P}} - \mathbf{P}^r\|$ [mm] |
|---|---|---|---|---|---|
| | | **x** | **y** | **z** | |
| 1 | 15 | -18.1 ± 0.06 | -17.4 ± 0.98 | -24.8 ± 1.53 | 8.3 |
| 2 | 15 | -14.8 ± 0.05 | -6.9 ± 0.93 | 52.2 ± 1.78 | 10.7 |
| 3 | 7.5 | -3.1 ± 0.03 | 17.0 ± 0.25 | 139.9 ± 3.18 | 16.8 |
| 4 | 7.5 | -3.2 ± 0.02 | 14.7 ± 0.54 | 84.1 ± 2.71 | 15.3 |
| 5 | 7.5 | -3.2 ± 0.02 | 10.7 ± 0.83 | 49.2 ± 2.39 | 18.7 |

direction is reduced by combining multiple views using a Kalman filter. However, the estimation error in the initial in-image-plane direction increases by adding additional views. This is because the most uncertain axis of the rotated view is no longer orthogonal to the least uncertain axis of the current estimate. The variance of the estimation slightly increases in that direction when the new measurement is added, and, since the measurement is noisy, the position error may slightly increase as well. The results show that the error and standard deviation in the $x$-axis is much smaller than the standard deviation in the $y$- and $z$-axes because the C-Arm was rotated about the $x$-axis and remained orthogonal to the most uncertain measurement direction for all images. As expected, the total estimation error and total standard deviation improves with each successive view.
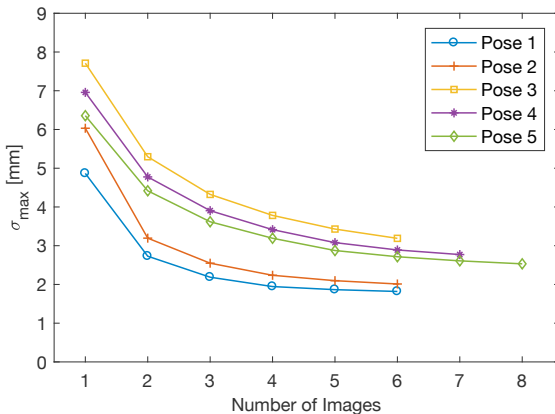
Figure 3.6 : The maximum standard deviation of the position estimate $\sigma_{\max}$ by imposing multiple views. The variation in initial errors is mainly due to differences in the imaged width of the catheter, which is a function of the distance from the X-ray source.

### 3.3.3.2  Convergence of error covariance

The square root of the maximum singular value of the updated covariance matrix $\Sigma_k$ is shown in Figure 3.6 for different poses of the catheter. As discussed in section 3.1, the singular values of the covariance matrix give the variances of the estimated position and the square root is the standard deviation of estimates. The length of the major axis of the uncertainty ellipse in the estimated position is $\sigma_{max}$. This maximum uncertainty decreases quickly as the iteration proceeds and multiple views are combined. The initial uncertainty starts between 4.8 mm and 7.7 mm and converges to less than 3.2 mm, which implies the estimated positions after the iterations have an estimate standard deviation of less than 3.2 mm. The initial errors are not equal because the position and width of the catheter in the fluoroscopic image affects the measurement covariance, as shown in Figure 3.2. As is the nature of the Kalman filtering, $\sigma_{max}$ will asymptotically decrease to a steady state value, which is a function of both the measurement noise and process noise by incorporating new measurements.

## 3.4  Tracking DBS Electrodes

In DBS procedure, a position verification for electrodes is performed using 2D fluoroscopy at first in the operating room and then a postoperative CT scan val-

idates the final location afterwards. To enable full 3D localization in the operating room, intraoperative fluoroscopic guidance was suggested utilizing fiducial markers. The intraoperative DBS electrode tracking has been demonstrated by using biplanar orthogonal fluoroscopy with four fiducial markers mounted on a stereotactic frame [14]. Recent work has proposed an image segmentation and optimization method to localize DBS electrodes in fluoroscopic images using two fiducial markers [15].

The method proposed in [15] is used to segment the fiducial markers in a fluoroscopic image and localize them in three dimensions with respect to the fluoroscope. The DBS electrode is localized using its physical size and the projected area, also with respect to the fluoroscopic geometry. These two segmentation results derive the 3D electrode position relative to the fiducial markers. The proposed method in 3.2 is then employed to combine multiple fluoroscopic views. The final localization result is compared to the postoperative CT scans.

### 3.4.1 Surgical Procedure

A preoperative CT/MR imaging and surgical planning were performed before operations without changes. At the beginning of surgery, custom-made fiducial markers were fixed to both sides of the stereotactic frame as shown in Figure 3.7 (b). These markers were sterilized before surgery to allow handling in the operating room without risk of contamination. The steps of intraoperative microelectrode targeting, neurological testing, and electrodes implantation followed the current surgical procedure.

After the permanent electrodes were placed, fluoroscopic images were taken from several different perspectives. The images could capture the electrodes and fiducial markers in the field of view as shown in Figure 3.7 (a). The postoperative CT scan validated the final position of electrodes which was later used as the reference position to compare the tracking results.

All the fluoroscopic images were taken with the informed consent from patients, and the study protocol was approved by the ethics committee of the University Hospital of Zurich. The fluoroscopic images and CT data were collected anonymously.
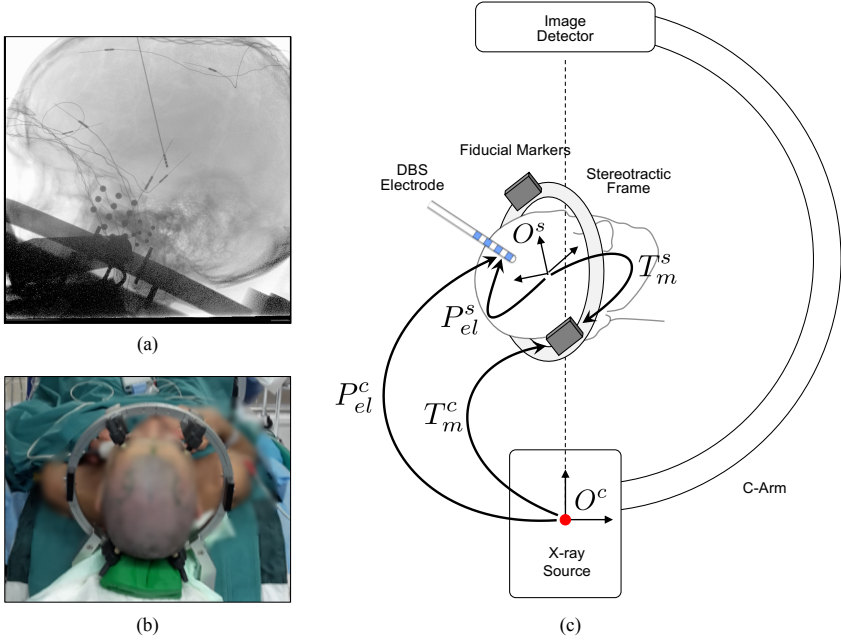
Figure 3.7 : *In vivo* experimental setup. (a) A fluoroscopic image capturing two fiducial markers and a DBS electrode in the scene. (b) The markers were fixed to both sides of the stereotactic frame, which was mounted to the skull before the surgery. (c) Equipment used in the experiment.

### 3.4.2 Localization from a Single Fluoroscopic Image

A fluoroscopic image captures electrodes and a pair of fiducial markers as shown in Figure 3.7 (a). From this image, the pixel position of the markers is segmented using the method proposed in [15]. A blob detector is first used to segment any circular objects in the scene. Among those detected blobs, the set of points which gives minimum errors relative to the projection of the fiducial markers is chosen as the matching set. Using least squares interpolation, the transformation of the markers with respect to the C-Arm frame is measured as $T_m^c$.

For electrode segmentation, the image position is first obtained using a fast feature detector [16] that determines the region of interest. An alpha matting approach is then used to segment the electrode from the background. The center and orientation is obtained by calculating the center of mass and the principal

axis of the segmented image using the covariance matrix, respectively. The width of the electrode is measured from the intensity profile along the short axis. Then the 3D pose of the electrode is obtained comparing the center and width information in pixels to the physical size of the electrode, which measures $P_{el}^c$.

From the calculated transformations $T_m^c$ and the position of the electrode in the C-Arm frame $P_{el}^c$, the position of the electrodes in the stereotactic frame is obtained as shown in Figure 3.7 (c) as

$$P_{el}^s = T_m^s (T_m^c)^{-1} P_{el}^c \tag{3.21}$$

where the transformation of the markers to the stereotactic frame, $T_m^s$, is given from its geometry.

To characterize the measurement noise of the above segmentation method, the same fluoroscopic device in section 3.3 is used. Ten images are taken at each of nine different poses for a total of ninety fluoroscopic images. To calculate the covariance of $u$, $v$, and $\delta_i$, the mean value of four leads' center and width are used. The measurement covariance $M_I$ for the image parameters, measured in pixels, is

$$M^I = \begin{bmatrix} 0.0498 & -0.0177 & -0.0087 \\ -0.0177 & 0.0498 & -0.0087 \\ -0.0087 & -0.0087 & 0.1603 \end{bmatrix}, \tag{3.22}$$

which results in the variances as $\sigma_u^2 = \sigma_v^2 = 0.0498$ and $\sigma_{\delta_i}^2 = 0.1603$. The process noise is again assumed as small as $N = [1\ 0\ 0,\ 0\ 1\ 0,\ 0\ 0\ 1]$, measured in millimeters.

### 3.4.3 Results

Three electrode positions were estimated to demonstrate the proposed approach. Figure 3.8 and Table 3.5 show the estimation results for one electrode from patient I as an example. During the operation, four electrodes were implanted into this patient and the first implanted electrode which targeted the left subthalamic nucleus was localized. The three fluoroscopic images were taken at different C-Arm configurations and used to estimate the 3D position as shown in Figure 3.8 (a). Each image resulted in the position estimate, $\mathbf{Q_0}$, $\mathbf{Q_1}$, and $\mathbf{Q_2}$, respectively. The position estimates and the estimation uncertainties are depicted in Figure 3.8 (b) and they are compared to the reference position $\mathbf{P}^r$, which was
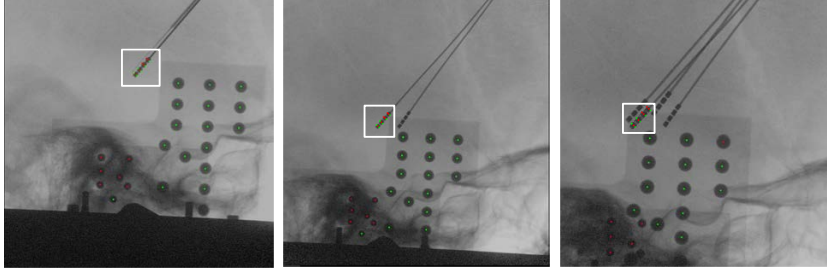
(a)
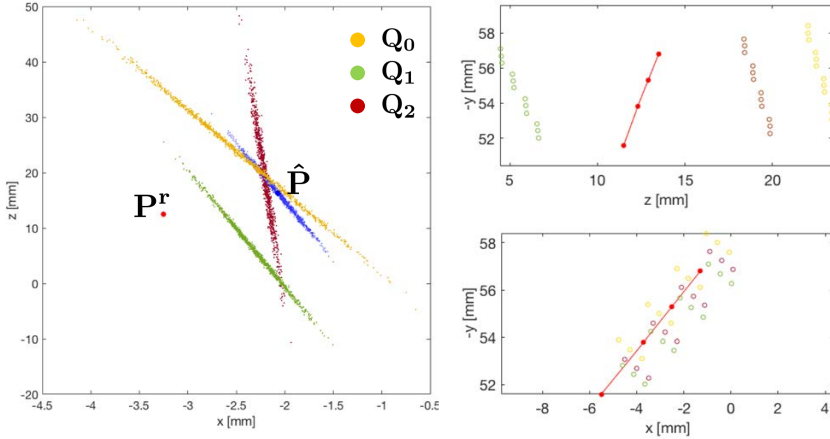


(b)

Figure 3.8 : Position estimation results for the DBS electrode implanated in patient I. (a) Fluoroscopic images capturing the electrode and fiducial markers taken at three different C-Arm configurations. The segmentation results for the electrode are presented in the white boxes. (b) Position estimates from each fluoroscopic image depicted with its uncertainty. Note that the scale of the axis is not equal in x- and z-axis.

manually measured from the postoperative CT scan.

The proposed approach gives the mean estimation error for three poses as 3.66 mm in 3D space and 3.32 mm in the stereotactic frame's z-direction. The maximum standard deviation of the position estimates ($\sigma_{\max}$) were decreased to 5.17 mm, which is about 64 percent compared to the initial estimate $\mathbf{P_0}$. Since the fluoroscopic images were taken in the operation room, the eligible number of images were limited to minimize the radiation exposure to the patients. Also,

Table 3.5 : ESTIMATED POSITION **Q** USING A SINGLE IMAGE AND THE COMBINED POSITION ESTIMATE $\hat{\mathbf{P}}$ FROM PATIENT I.

|  | **x** | **y** | **z** | **Error** [mm] |
|---|---|---|---|---|
| **P**$^r$ | -3.25 | -54.38 | 12.55 | - |
| **Q$_0$** | -2.42 ± 0.57 | -55.75 ± 0.31 | 22.73 ± 8.42 | 10.31 |
| **Q$_1$** | -2.29 ± 0.29 | -54.55 ± 0.23 | 5.54 ± 6.10 | 7.07 |
| **Q$_2$** | -2.20 ± 0.07 | -54.97 ± 0.34 | 19.13 ± 8.34 | 6.69 |
| $\hat{\mathbf{P}}$ | -2.07 ± 0.23 | -55.08 ± 0.16 | 16.28± 4.28 | 3.98 |
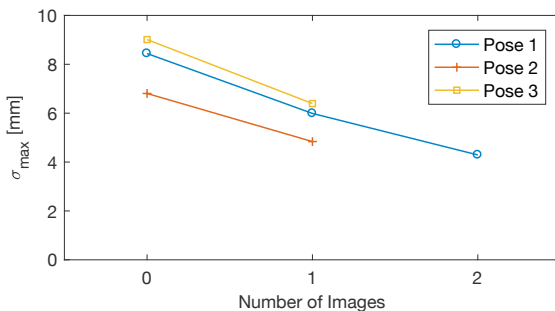


Figure 3.9 : The maximum standard deviation of the position estimate $\sigma_{\max}$ by imposing multiple views.

the C-Arm configurations were restricted and thus the most uncertain axis of the estimates did not change largely. These factors led to a similar estimation error in 3D space and in the depth direction. Compared to previous experimental results of cardiac ablation catheter, the estimation errors are relatively smaller, which were attributed to the reference position measured with a higher accuracy using the CT scan. However, the estimates are still suboptimal. This could be caused by any segmentation errors occurred when calculating the transformation matrix $T_m^c$.

## 3.5 Discussion

A fluoroscopic tracking method is herein proposed to assess localization uncertainties associated with a single fluoroscopic image and combine sequential

position estimates using a Kalman filter. The method is evaluated using two different minimally invasive surgical tools, the cardiac ablation catheter and the DBS electrode. Using a calibrated C-Arm fluoroscope for tracking cardiac ablation catheters, the estimated standard deviation was reduced by 62 percent compared to a single image. The absolute accuracy was within the uncertainty of our manual measurements. The validation was extended to the case *in situ* in the operating room. A DBS electrode was localized using a pair of custom-made fiducial markers which was attached on the stereotactic frame. This experiment resulted in a 36 percent decrease in the estimated standard deviation.

The estimation uncertainty is analyzed based on a condition number in (3.9), which indicates the ratio of the largest to the smallest standard deviations of the estimates. The condition number is a function of the physical size of an object and its location with respect to the fluoroscopic imaging system. When an object is closer to the X-ray source and its physical size gets bigger, the X-ray projection occupies a larger area in the detector, and this helps to attain a better image segmentation. Therefore, it is possible to estimate the 3D position of an object with higher precision.

This method can be expanded to any number of minimally invasive surgical tools in the field of view. Additionally, the method can be directly extended to non-stationary objects because a Kalman filter approach is used. However, one thing to note is that the C-Arm should be configured carefully to avoid an overlap of surgical tools.

# References

[1] F. Viñuela, G. Duckwiler, and M. Mawad, "Guglielmi detachable coil embolization of acute intracranial aneurysm: Perioperative anatomical and clinical outcome in 403 patients," *J Neurosurg*, vol. 86, no. 3, pp. 475–482, 1997.

[2] S. K. Hilai, W. Jost Michelsen, J. Driller, and E. Leonard, "Magnetically guided devices for vascular exploration and treatment: Laboratory and clinical investigations 1," *Radiology*, vol. 113, no. 3, pp. 529–540, 1974.

[3] L. K. Wagner, P. J. Eifel, and R. A. Geise, "Potential biological effects following high X-ray dose interventional procedures," *J Vasc Interv Radiol*, vol. 5, no. 1, pp. 71–84, 1994.

[4] A. Talukdar and D. Wilson, "Modeling and optimization of rotational C-arm stereoscopic X-ray angiography," *IEEE Trans Med Imaging*, vol. 18, no. 7, pp. 604–616, Jul. 1999.

[5] C. V. Bourantas, I. C. Kourtis, M. E. Plissiti, D. I. Fotiadis, C. S. Katsouras, M. I. Papafaklis, and L. K. Michalis, "A method for 3D reconstruction of coronary arteries using biplane angiography and intravascular ultrasound images," *Comput Med Imaging Graph*, vol. 29, no. 8, pp. 597–606, 2005.

[6] M. S. Grady, M. A. Howard III, R. G. Dacey Jr, W. Blume, M. Lawson, P. Werp, and R. C. Ritter, "Experimental study of the magnetic stereotaxis system for catheter manipulation within the brain," *J Neurosurg*, vol. 93, no. 2, pp. 282–288, 2000.

[7] P. Fallavollita, "Is single-view fluoroscopy sufficient in guiding cardiac ablation procedures?" *Int J Biomed Imaging*, vol. 2010, p. 1, 2010.

[8] L. Yatziv, M. Chartouni, S. Datta, and G. Sapiro, "Toward multiple catheters detection in fluoroscopic image guided interventions," *IEEE Trans Inf Technol Biomed*, vol. 16, no. 4, pp. 770–781, 2012.

[9] P. R. Bevington and D. K. Robinson, *Data reduction and error analysis for the physical sciences*. McGraw-Hill New York, 1969, vol. 336.

[10] H. W. Sorenson, "Least-squares estimation: From gauss to kalman," *IEEE Spectr*, vol. 7, no. 7, pp. 63–68, 1970.

[11] R. E. Kalman, "A new approach to linear filtering and prediction problems," *J Fluids Eng*, vol. 82, no. 1, pp. 35–45, 1960.

[12] Ziehm Imaging Inc, Available at: http://www.ziehm.com.

[13] I. Biosense Webster, Available at: https://www.biosensewebster.com/.

[14] S. Derrey, D. Maltête, N. Chastan, B. Debono, F. Proust, E. Gérardin, J. Weber, B. Mihout, and P. Fréger, "Deep brain stimulation of the subthalamic nucleus in parkinson's disease: Usefulness of intraoperative radiological guidance," *Stereotact Funct Neurosurg*, vol. 86, no. 6, pp. 351–358, 2008.

[15] D. Kasper, "DBS electrode localization," Master's thesis, ETH Zürich, 2016.

[16]  M. Muja and D. G. Lowe, "Fast approximate nearest neighbors with automatic algorithm configuration.," *VISAPP (1)*, vol. 2, no. 331-340, p. 2, 2009.

# Chapter 4

# Magnetic Guidance of a Flexible Needle

A rigid straight needle is currently utilized in the clinic to access deep brain regions, while providing a stable insertion. However, this confines the feasible paths only to straight trajectories, which can not be adjusted during needle insertion. In contrast, a flexible needle can achieve curved trajectories using a bending force around an asymmetric tip. The trajectories can then be corrected based on intra-operative imaging. Therefore, this flexible needle acts as a substitute for rigid straight needles.

There are several designs and actuation methods for steering flexible needles [1]–[3]. A bevel-tipped needle was driven using a combined motion of needle insertion and spinning where the asymmetric needle tip naturally induced a bending motion depending on its fabricated angle [4], [5]. To design paths with different curvatures, a duty-cycled spinning control was previously used. However, it may cause additional damage to the tissue surrounding the needle [6], [7]. Steering of these needles passively relies on tissue interaction forces, which displace the tip angle. Additionally, active needles have been introduced to control the tip angle and thus increase the tip dexterity. This includes flexible needles with a tendon-driven tip joint [8]–[10], optically actuated shape memory alloys [11], and offset adjustable parallel segments [12]. Recently, a flexible needle with a permanent magnetic tip was designed to reduce tissue damage due to its blunted tip. The feasibility of this strategy was demonstrated using phantom tissues with a high curvature path [13].

In this chapter, a flexible needle is steered under magnetic guidance. To improve its clinical relevance, a projective X-ray fluoroscope is utilized as an

imaging modality. Section 4.1 starts with an introduction to magnetic manipulation followed by the kinematic model that is developed for the magnetically guided flexible needles. A control strategy for steering the needle is described in section 4.2. Section 4.3 describes the experimental setups and their calibration method. This includes the calibration of parameters that are related to the kinematic model and to the fluoroscopic imaging systems. Finally, section 4.4 describes the experimental results of steering magnetic needle in the brain phantom tissue and *ex vivo* pig brain.

## 4.1 Modeling of a Magnetic Needle

A magnetic needle is modeled with a rigid magnetic tip connected to a non-magnetic flexible body which follows the trajectory of the tip. A simple mechanism for steering this magnetic needle through soft tissue is used. The external magnetic field controls the direction of the magnetic tip, and the linear motion at the distal end of the needle actuates the needle insertion. Due to asymmetric stress surrounding the tip, the needle penetrates through tissue in a preferential direction. A detailed description of the magnetic needle model followed by a brief introduction of magnetic manipulation is given in the next sections.

### 4.1.1 Magnetic Manipulation

Magnetic manipulation systems generate magnetic fields and gradients to guide a magnetized object while permeating non-magnetic environment such as the human body. One way of generating magnetic fields and gradients is to use electromagnets which usually consist of a ferromagnetic core and a wire winding up the core. The magnetic field is produced by the electric current through the wire.

The externally applied field is expressed as the magnetic flux density $\mathbf{B}$ [T] as

$$\mathbf{B} = \mu_0 \mathbf{H} \tag{4.1}$$

where $\mu_0 = 4\pi \times 10^{-7}$ [T·m/A] is the permeability of vacuum and $\mathbf{H}$ [A/m] is the external magnetic field strength. This magnetic field exerts the magnetic torque

and force on the object as [14]

$$\tau = v\mathbf{M} \times \mathbf{B}$$

$$\mathbf{F} = v(M \cdot \boldsymbol{\nabla})\mathbf{B} = v \left[ \frac{\partial \mathbf{B}}{\partial x} \quad \frac{\partial \mathbf{B}}{\partial y} \quad \frac{\partial \mathbf{B}}{\partial z} \right] M \tag{4.2}$$

where $v \, [\mathrm{m}^3]$ is the volume of the magnetic material in the object, $\mathbf{M} \, [\mathrm{A/m}]$ is the remnant magnetization vector, and $\boldsymbol{\nabla}$ is the vector-gradient operator. The induced magnetic torque and force can control the position and orientation of the object. The torque $\tau$ aligns the magnetization direction of the object to the applied field direction, and the force $\mathbf{F}$ creates a translational motion in the direction of the magnetic field gradients.

A magnetic manipulation system can be configured with a number of electromagnets. Each of them generates a magnetic field throughout the workspace, and the total magnetic field can be assumed as the sum of the contributions of all individual electromagnets.

At a given point $\mathbf{P}$, a $k$-th electromagnet generates a magnetic field as $\mathbf{B}_k(\mathbf{P})$. This is linearly proportional to the current $I_k$ with constant matrix $\tilde{\mathbf{B}}_k$, which denotes the contribution of the $k$-th electromagnet by unit current. The total magnetic field is then expressed as

$$\mathbf{B}(\mathbf{P}) = \sum_{k=1}^{n} \tilde{\mathbf{B}}_k(\mathbf{P})I_k = \mathcal{B}(\mathbf{P})\mathbf{I} \tag{4.3}$$

where $\mathcal{B}(\mathbf{P})$ is a $3 \times n$ unit field contribution matrix, and $\mathbf{I}$ is a $n \times 1$ vector imposing the currents in each magnet.

Using (4.2) and (4.3), the magnetic force and torque applied to the object can be expressed with the input current $\mathbf{I}$ as

$$\begin{bmatrix} \tau \\ \mathbf{F} \end{bmatrix} = \mathcal{A}(\tilde{\mathbf{B}}, \mathbf{P})\mathbf{I} \tag{4.4}$$

where $\mathcal{A}(\tilde{\mathbf{B}}, \mathbf{P})$ is a $6 \times n$ actuation matrix that maps the current of $n$ electromagnets to a field and gradient at a given point $\mathbf{P}$. For a desired torque and force vector $[\tau_{\mathrm{des}} \, \mathbf{F}_{\mathrm{des}}]^T$, the required currents in the electromagnets can be found by using the pseudo-inverse of $\mathcal{A}$ as

$$\mathbf{I} = \mathcal{A}(\tilde{\mathbf{B}}, \mathbf{P})^{\dagger} \begin{bmatrix} \tau_{\mathrm{des}} \\ \mathbf{F}_{\mathrm{des}} \end{bmatrix}. \tag{4.5}$$
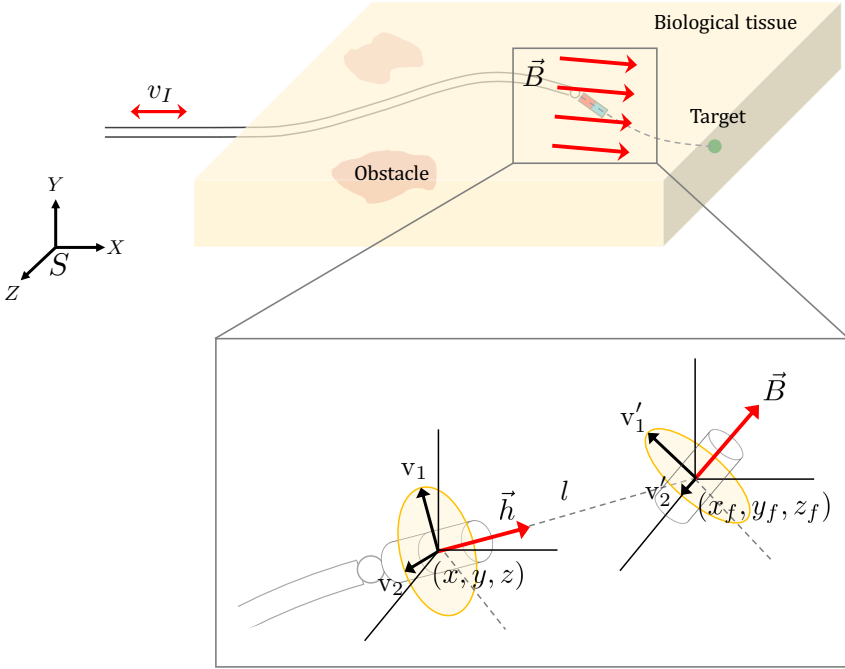
Figure 4.1 : Schematics of a magnetic flexible needle steered in soft tissue. The direction of the magnetic tip is steered with the external magnetic field and the flexible needle body follows the trajectory of the tip with the linear motion at the distal end.

## 4.1.2 Kinematic Model of a Magnetic Needle

Using an external magnetic field, the direction of a magnetic tip is actively steered. The insertion of the needle body is actuated using a motorized linear advancer at the distal end of the needle as shown in Figure 4.1. To simplify the model of a magnetically steerable needle, several assumptions were made. First, the external magnetic field is large enough to guide the needle tip direction in a short time, which allows to consider the orientation of the applied magnetic field as the steering direction of the needle. Second, the flexible needle body follows the trajectory of the magnetic needle tip, which allows to neglect any damage coming from the needle cutting through tissue.

The kinematics of the magnetically guided flexible needle can be similar to that of a bicycle model, which was adapted previously for flexible needles.

Webster *et al.* showed that a bevel tip needle could be considered as a bicycle model with a fixed steering angle [15], and Ko *et al.* adapted the same model but with a steerable angle [12]. In our case, the external magnetic field is actively steering the front wheel at a virtual point in front of the needle tip, and the magnetic tip and the flexible body follow the bending motion without slipping.

Figure 4.1 shows a schematic drawing of a magnetically guided flexible needle. A virtual point in front of the needle tip is assigned at $\mathbf{P}_f$ which serves as a steering wheel in the bicycle model. The orientation of the external magnetic field $\mathbf{B}$ steers the virtual front wheel direction. Then, the needle tip acts as the rear wheel of a bicycle model following its front wheel with an orientation defined by $\mathbf{h}$. Therefore, the configuration of the magnetic needle is denoted with the heading direction $\mathbf{h} = [h_x \, h_y \, h_z]^T$ at position $\mathbf{P} = [x \, y \, z]^T$ and the steering magnetic field direction $\mathbf{B} = [B_x \, B_y \, B_z]^T$ at position $\mathbf{P}_f = [x_f \, y_f \, z_f]^T$. Here $\mathbf{h}$ and $\mathbf{B}$ are unit vectors. By letting the distance between the needle tip and the front wheel be a positive number $l$ and using a rigid-body constraint, the 3D position of the steering front wheel can be obtained as

$$\mathbf{P}_f = \mathbf{P} + l\mathbf{h}. \tag{4.6}$$

A non-slipping condition in the bicycle model constrains the velocity of the two wheels in the direction perpendicular to their orientation. This is applied to our model as

$$\begin{aligned} h_y \dot{x} - h_x \dot{y} &= 0 \\ h_z \dot{x} - h_x \dot{z} &= 0 \\ B_y \dot{x}_f - B_x \dot{y}_f &= 0 \\ B_z \dot{x}_f - B_x \dot{z}_f &= 0. \end{aligned} \tag{4.7}$$

Using (4.6), these constraints can be expressed compactly as

$$\omega(\mathbf{q}) \cdot \dot{\mathbf{q}} = 0 \tag{4.8}$$

where

$$\mathbf{q} = \begin{bmatrix} x & y & z & h_y & h_z & B_y & B_z \end{bmatrix}^T$$

$$\omega = \begin{bmatrix} h_y & -h_x & 0 & 0 & 0 & 0 & 0 \\ h_z & 0 & -h_x & 0 & 0 & 0 & 0 \\ B_y & -B_x & 0 & \dfrac{-l(B_x h_x + B_y h_y)}{h_x} & \dfrac{-l B_y h_z}{h_x} & 0 & 0 \\ B_z & 0 & -B_x & \dfrac{-l h_y B_z}{h_x} & \dfrac{-l(B_x h_x + B_z h_z)}{h_x} & 0 & 0 \end{bmatrix}.$$

Here, the target is assumed to be posed ahead of the initial position to maintain $h_x = (1 - h_y^2 - h_z^2)^{1/2} > 0$ and $B_x = (1 - B_y^2 - B_z^2)^{1/2} > 0$. Note that $h_x$ and $B_x$ are excluded from the state vector because they are redundant variables.

A system with nonholonomic constraints in (4.8) can be represented as a control system with the input $\mathbf{u} = [u_1 \, u_2 \, u_3]^T$ as

$$\dot{\mathbf{q}} = \mathbf{g_1}(\mathbf{q})u_1 + \mathbf{g_2}(\mathbf{q})u_2 + \mathbf{g_3}(\mathbf{q})u_3 \tag{4.9}$$

where

$$\mathbf{g}_1 = \begin{bmatrix} h_x & h_y & h_z & \dfrac{h_z C_2 - h_x C_1}{l(\mathbf{B} \cdot \mathbf{h})} & \dfrac{h_x C_3 - h_y C_2}{l(\mathbf{B} \cdot \mathbf{h})} & 0 & 0 \end{bmatrix}^T$$

$$\mathbf{g}_2 = \begin{bmatrix} 0 & 0 & 0 & 0 & 0 & 1 & 0 \end{bmatrix}^T$$

$$\mathbf{g}_3 = \begin{bmatrix} 0 & 0 & 0 & 0 & 0 & 0 & 1 \end{bmatrix}^T$$

$$C_1 = B_x h_y - B_y h_x, \quad C_2 = B_y h_z - B_z h_y, \quad C_3 = B_z h_x - B_x h_z.$$

Here, $\mathbf{g}_1$, $\mathbf{g}_2$, $\mathbf{g}_3$ are chosen so that the input $u_1$ corresponds to the needle insertion velocity at the distal end which is $v_I$, and $u_2, u_3$ correspond to the change rates of the steering direction which are $\dot{B}_y, \dot{B}_z$. The forth and fifth elements of $\mathbf{g}_1$ are the second and third elements of the vector $\dfrac{\mathbf{h} \times (\mathbf{B} \times \mathbf{h})}{l(\mathbf{B} \cdot \mathbf{h})}$. This vector holds the time-derivative of the heading direction $\dot{\mathbf{h}}$ in the plane containing $\mathbf{h}$ and $\mathbf{B}$, and its magnitude is correspondent to the tangent value of the angle between two vectors, $\mathbf{h}$ and $\mathbf{B}$. To avoid model singularity, the steering direction relative to the current needle tip direction is restricted to be less than $\pi/2$, i.e., $\mathbf{h} \cdot \mathbf{B} \neq 0$.

The parameter $l$ is strictly positive, implying that the distance offset between the steering wheel and the tip always exists. Physical properties such as stiffness

and the damping coefficient of the soft tissue, as well as the magnitude of the external magnetic field, decide the virtual offset distance $l$. For example, when the reaction force from soft tissue is large, it demands more efforts to align the magnetic tip to the input field direction, which can be incorporated with a larger $l$. In the same manner, an external magnetic field with large magnitude causes a large torque on the tip. It requires less time to align the tip, thus resulting in a smaller $l$. This value of $l$ can be experimentally determined with a specific soft tissue phantom.

## 4.2 Feedback Control

The nonholonomic system in (4.9) is controllable according to Chow's theorem [16]. However, the stability of this system is not guaranteed by only using time-invariant feedback [17]. Murray and Sastry introduced a method to transform nonholonomic systems into chained form systems [18] which is analogous to the exact linearization of a nonlinear system described in [19]. Bushnell *et al.* further expanded and generalized the previous work to deal with nonholonomic systems with more than three inputs [20]. Our kinematic model of a magnetic needle can be understood as the system described in [20].

### 4.2.1 Chained System

According to the Proposition I in [20], a drift-free, nonholonomic system with three inputs can be converted to a two-chain, single-generator chained form as

$$
\begin{aligned}
&\dot{z}_1 = v_1 & &\dot{z}_2 = v_2 & &\dot{z}_5 = v_3 \\
& & &\dot{z}_3 = z_2 v_1 & &\dot{z}_6 = z_5 v_1 \\
& & &\dot{z}_4 = z_3 v_1 & &\dot{z}_7 = z_6 v_1
\end{aligned}
\tag{4.10}
$$

with a coordinate change and an invertible input transformation

$$
\begin{aligned}
\mathbf{z} &= \begin{bmatrix} z_1 & z_2 & z_3 & z_4 & z_5 & z_6 & z_7 \end{bmatrix}^T = \mathbf{\Phi}(\mathbf{q}) \\
\mathbf{v} &= \begin{bmatrix} v_1 & v_2 & v_3 \end{bmatrix}^T = \beta(\mathbf{q})\mathbf{u}
\end{aligned}
\tag{4.11}
$$

if there exists a basis $\mathbf{f}_1, \mathbf{f}_2, \mathbf{f}_3$ for $\Delta = \mathrm{span}\{\mathbf{g}_1, \mathbf{g}_2, \mathbf{g}_3\}$ such that the distributions

$$
\mathbf{G}_i := \mathrm{span}\{\mathrm{ad}^i_{\mathbf{f}_1}\mathbf{f}_2, \mathrm{ad}^i_{\mathbf{f}_1}\mathbf{f}_3\} \quad \text{for} \quad 0 \le i \le n-1
\tag{4.12}
$$

have constant dimensions and are all involutive. Here, the Lie bracket of the vector fields $\mathbf{f}$ and $\mathbf{g}$ are defined as

$$[\mathbf{f}, \mathbf{g}](\mathbf{x}) = \frac{\partial \mathbf{g}}{\partial \mathbf{x}} \mathbf{f}(\mathbf{x}) - \frac{\partial \mathbf{f}}{\partial \mathbf{x}} \mathbf{g}(\mathbf{x})$$

$$\mathrm{ad}_{\mathbf{f}}^0 \mathbf{g}(\mathbf{x}) = \mathbf{g}(\mathbf{x})$$

$$\mathrm{ad}_{\mathbf{f}}^k \mathbf{g}(\mathbf{x}) = [\mathbf{f}, \mathrm{ad}_{\mathbf{f}}^{k-1} \mathbf{g}](\mathbf{x}), \quad k \leq 1$$

and the Lie Derivative of a vector field $\mathbf{h}$ along $\mathbf{f}$ is defined as

$$L_{\mathbf{g}} L_{\mathbf{f}} \mathbf{h}(\mathbf{x}) = \frac{\partial (L_{\mathbf{f}} \mathbf{h})}{\partial \mathbf{x}} \mathbf{g}(\mathbf{x})$$

$$L_{\mathbf{f}}^k \mathbf{h}(\mathbf{x}) = L_{\mathbf{f}} L_{\mathbf{f}}^{k-1} = \frac{\partial (L_{\mathbf{f}}^{k-1} \mathbf{h})}{\partial \mathbf{x}} \mathbf{f}(\mathbf{x})$$

$$L_{\mathbf{f}}^0 \mathbf{h}(\mathbf{x}) = \mathbf{h}(\mathbf{x}).$$

This condition is used to find the chained form system for the magnetic needle model in (4.9). The vector fields $\mathbf{f}_1$, $\mathbf{f}_2$, $\mathbf{f}_3$ can be chosen as

$$\mathbf{f}_1 = \frac{\mathbf{g}_1}{h_x} \quad \mathbf{f}_2 = \mathbf{g}_2 \quad \mathbf{f}_3 = \mathbf{g}_3 \tag{4.13}$$

which describes the same system as in (4.9) with a new input vector $\mathbf{u}' = [h_x v_I \ \dot{B}_y \ \dot{B}_z]^T$. The corresponding distributions are constructed as

$$\mathbf{G}_0 = \mathrm{span}\{\mathbf{f}_2, \mathbf{f}_3\}$$

$$\mathbf{G}_1 = \mathrm{span}\{\mathbf{f}_2, \mathrm{ad}_{\mathbf{f}_1}\mathbf{f}_2, \mathbf{f}_3, \mathrm{ad}_{\mathbf{f}_1}\mathbf{f}_3\} \tag{4.14}$$

$$\mathbf{G}_2 = \mathrm{span}\{\mathbf{f}_2, \mathrm{ad}_{\mathbf{f}_1}\mathbf{f}_2, \mathrm{ad}_{\mathbf{f}_1}^2\mathbf{f}_2, \mathbf{f}_3, \mathrm{ad}_{\mathbf{f}_1}\mathbf{f}_3, \mathrm{ad}_{\mathbf{f}_1}^2\mathbf{f}_3\}$$

where the distribution $\mathbf{G}_2$ has dimension $n - 1 = 6$ and $\mathbf{G}_0, \mathbf{G}_1, \mathbf{G}_2$ are all involutive. With the function $h_1 = x$, $h_2 = y$, $h_3 = z$, the chained form coordinates can be transformed from the state variables as

$$
\begin{aligned}
&z_1 = h_1 = x \\
&z_2 = L_{\mathbf{f}_1}^2 h_2 = \frac{-C_1}{lh_x^3(\mathbf{B} \cdot \mathbf{h})} \quad z_5 = L_{\mathbf{f}_1}^2 h_3 = \frac{C_3}{lh_x^3(\mathbf{B} \cdot \mathbf{h})} \\
&z_3 = L_{\mathbf{f}_1} h_2 = \frac{h_y}{h_x} \qquad\qquad z_6 = L_{\mathbf{f}_1} h_3 = \frac{h_z}{h_x} \\
&z_4 = h_2 = y \qquad\qquad\qquad z_7 = h_3 = z
\end{aligned}
\tag{4.15}
$$

and the corresponding input transformation is determined as

$$\mathbf{v} = \beta(\mathbf{q})\mathbf{u}$$

$$= \begin{bmatrix} 1 & 0 & 0 \\ \beta_{21} & \beta_{22} & \beta_{23} \\ \beta_{31} & 0 & \beta_{33} \end{bmatrix} \mathbf{u}$$

$$= \begin{bmatrix} 1 & 0 & 0 \\ L_{\mathbf{f}_1}^3 h_2 & L_{\mathbf{f}_2} L_{\mathbf{f}_1}^2 h_2 & L_{\mathbf{f}_3} L_{\mathbf{f}_1}^2 h_2 \\ L_{\mathbf{f}_1}^3 h_3 & 0 & L_{\mathbf{f}_3} L_{\mathbf{f}_1}^2 h_3 \end{bmatrix} \mathbf{u}$$

(4.16)

where

$$\beta_{21} = \frac{(B_x h_x + B_y h_y)(h_x C_1 - h_z C_2) + B_y h_z(h_y C_2 - h_x C_3)}{l^2 h_x^4 (\mathbf{B} \cdot \mathbf{h})^2}$$
$$+ \frac{3C_1(h_y C_1 - h_z C_3)}{l^2 h_x^4 (\mathbf{B} \cdot \mathbf{h})^2} + \frac{C_1^2(h_x C_1 - h_z C_2) - C_1 C_3(h_y C_2 - h_x C_3)}{l^2 h_x^4 (\mathbf{B} \cdot \mathbf{h})^3}$$

$$\beta_{22} = \frac{B_x h_x + B_y h_y}{l h_x^3 B_x (\mathbf{B} \cdot \mathbf{h})} + \frac{C_1^2}{l h_x^3 B_x (\mathbf{B} \cdot \mathbf{h})^2}$$

$$\beta_{23} = \frac{B_z h_y}{l h_x^3 B_x (\mathbf{B} \cdot \mathbf{h})} - \frac{C_1 C_3}{l h_x^3 B_x (\mathbf{B} \cdot \mathbf{h})^2}$$

$$\beta_{31} = \frac{(B_x h_x + B_z h_z)(h_y C_2 - h_x C_3) + B_z h_y(h_x C_1 - h_z C_2)}{l^2 h_x^4 (\mathbf{B} \cdot \mathbf{h})^2}$$
$$+ \frac{3C_3(h_z C_3 - h_y C_1)}{l^2 h_x^4 (\mathbf{B} \cdot \mathbf{h})^2} + \frac{C_3^2(h_y C_2 - h_x C_3) - C_1 C_2(h_x C_1 - h_z C_2)}{l^2 h_x^4 (\mathbf{B} \cdot \mathbf{h})^3}$$

$$\beta_{32} = \frac{B_y h_z}{l h_x^3 B_x (\mathbf{B} \cdot \mathbf{h})} - \frac{C_1 C_3}{l h_x^3 B_x (\mathbf{B} \cdot \mathbf{h})^2}$$

$$\beta_{33} = \frac{B_x h_x + B_z h_z}{l h_x^3 B_x (\mathbf{B} \cdot \mathbf{h})} + \frac{C_3^2}{l h_x^3 B_x (\mathbf{B} \cdot \mathbf{h})^2}.$$

### 4.2.2 Nonlinear Error Equation

For the chained form system in (4.15) and (4.16), the state and input errors can be denoted as

$$
\begin{aligned}
e_i &= z_{id} - z_i & i = 1 \cdots 7 \\
\tilde{v}_j &= v_{jd} - v_j & j = 1 \cdots 3
\end{aligned}
\tag{4.17}
$$

where $z_{id}$ is the desired state trajectory and $v_{jd}$ is the desired input trajectory. These can be obtained by transforming the predefined trajectory given in the cartesian coordinates as $\mathbf{P}_d = [x_d \, y_d \, z_d]^T$ to the desired trajectory in the chained form as described in [21]:

$$
\begin{aligned}
z_{1d} &= x_d \\
z_{2d} &= \frac{\dot{x}_d \ddot{y}_d - \ddot{x}_d \dot{y}_d}{\dot{x}_d^3} & z_{5d} &= \frac{\dot{x}_d \ddot{z}_d - \ddot{x}_d \dot{z}_d}{\dot{x}_d^3} \\
z_{3d} &= \frac{\dot{y}_d}{\dot{x}_d} & z_{6d} &= \frac{\dot{z}_d}{\dot{x}_d} \\
z_{4d} &= y_d & z_{7d} &= z_d
\end{aligned}
\tag{4.18}
$$

$$
\begin{aligned}
v_{1d} &= \dot{x}_d \\
v_{2d} &= \frac{\dot{x}_d^2 \dddot{y}_d - \dot{x}_d \dddot{x}_d \dot{y}_d - 3\dot{x}_d \ddot{x}_d \ddot{y}_d + 3\ddot{x}_d^2 \dot{y}_d}{\dot{x}_d^4} \\
v_{2d} &= \frac{\dot{x}_d^2 \dddot{z}_d - \dot{x}_d \dddot{x}_d \dot{z}_d - 3\dot{x}_d \ddot{x}_d \ddot{z}_d + 3\ddot{x}_d^2 \dot{z}_d}{\dot{x}_d^4}.
\end{aligned}
\tag{4.19}
$$

From (4.17), the nonlinear error equation can be obtained as

$$
\begin{aligned}
\dot{e}_1 &= \tilde{v}_1 \\
\dot{e}_2 &= \tilde{v}_2 \\
\dot{e}_3 &= z_{2d} v_{1d} - z_2 v_1 \\
\dot{e}_4 &= z_{3d} v_{1d} - z_3 v_1 \\
\dot{e}_5 &= \tilde{v}_3 \\
\dot{e}_6 &= z_{5d} v_{1d} - z_5 v_1 \\
\dot{e}_7 &= z_{6d} v_{1d} - z_6 v_1.
\end{aligned}
\tag{4.20}
$$

The Lyapunov-like function is chosen as $V = \dfrac{1}{2} \mathbf{e}^T \mathbf{e}$ which gives the time

derivative as

$$\dot{V} = \dot{\mathbf{e}}^T \mathbf{e}$$
$$= a_1 v_1 + b_1 v_{1d} + a_2 v_2 + b_2 v_{2d} + a_3 v_d + b_3 v_{3d} \tag{4.21}$$

where

$$a_1 = -e_1 - z_2 e_3 - z_3 e_4 - z_5 e_6 - z_6 e_7$$

$$a_2 = -e_2$$

$$a_3 = -e_5$$

$$b_1 = e_1 + z_{2d} e_3 + z_{3d} e_4 + z_{5d} e_6 + z_{6d} e_7$$

$$b_2 = e_2$$

$$b_3 = e_5.$$

With positive definite constants $k_1$, $k_2$, $k_3$ and the control input $\mathbf{v}$ as

$$v_1 = \frac{b_1}{a_1}(-v_{1d} - k_1 b_1)$$

$$v_2 = \frac{b_2}{a_2}(-v_{2d} - k_2 b_2) \tag{4.22}$$

$$v_3 = \frac{b_3}{a_3}(-v_{3d} - k_3 b_3),$$

the time-derivative of $V$ becomes $\dot{V} = -b_1^2 k_1 - b_2^2 k_2 - b_3^2 k_3 \leq 0$ showing that the function $V$ is negative semi-definite. The control input in (4.22) can be rewritten as

$$v_1 = \frac{e_1 + z_{2d} e_3 + z_{3d} e_4 + z_{5d} e_6 + z_{6d} e_7}{e_1 + z_2 e_3 + z_3 e_4 + z_5 e_6 + z_6 e_7}$$
$$\cdot (v_{1d} + (e_1 + z_{2d} e_3 + z_{3d} e_4 + z_{5d} e_6 + z_{6d} e_7) k_1) \tag{4.23}$$

$$v_2 = v_{2d} + k_2 e_2$$

$$v_3 = v_{3d} + k_3 e_5.$$

The overall block diagram for steering a magnetic needle is shown in Figure 4.2. The reference trajectory is obtained prior to the needle insertion from path planning algorithms. When the desired trajectory is given in cartesian coordinates, the desired state and input trajectory is calculated as in (4.18) and (4.19). Using the desired trajectory together with the state in chained form,
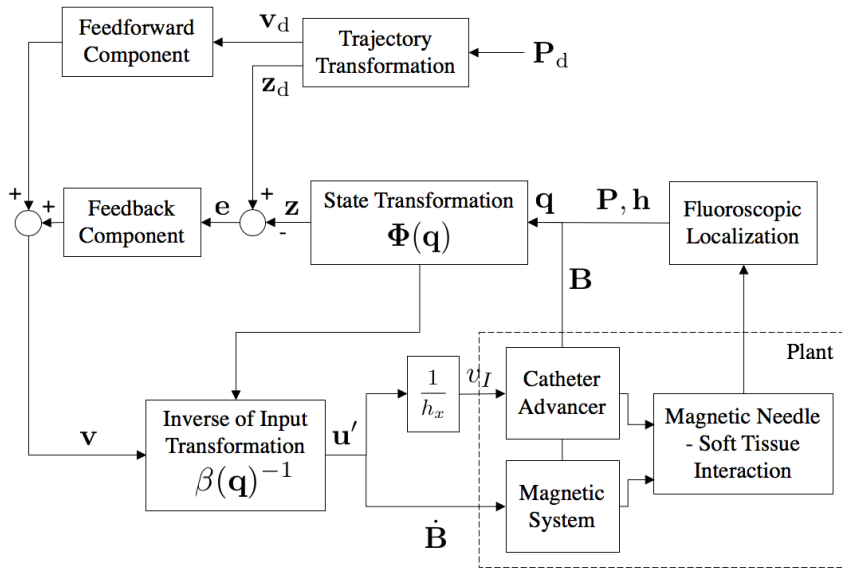
Figure 4.2 : Block diagram of steering a magnetic needle.

the feed-forward and feedback inputs are calculated following the control law in (4.23). The inverse of (4.16) calculates the velocity inputs to the catheter advancer and magnetic system. The resultant motion of the magnetic needle interacting with soft tissue is captured using a real-time fluoroscopic image. The state variables are transformed into the chained form using (4.15) which then close the control-loop.

## 4.3 Experimental Setup

The experimental setup that was used to test the performance of the proposed closed-loop trajectory controller is shown in Figure 4.3. The magnetic needle designed in [13] was tested using agarose gel as a brain phantom tissue and *ex vivo* pig brain. The linear motion i.e., insertion of the needle was actuated by a custom wire feeder, and the direction of the magnetic tip was controlled by an electromagnetic system. A C-Arm fluoroscope was employed to measure the needle's tip position. In the following section, each component of the experimental setup is described in detail, including the experimental calibration process.
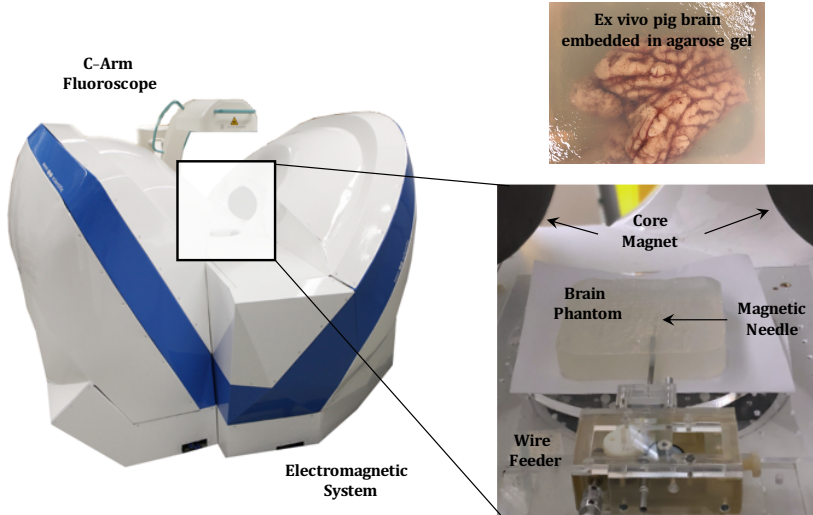
Figure 4.3 : Experimental setup for steering a flexible needle under the magnetic and fluoroscopic guidance.

### 4.3.1 Magnetic Needle Design and Fabrication

The magnetic needle used in this work consists of a cylindrical and a spherical NdFeB permanent magnet (both with a diameter of 1 mm and the cylindrical one with a height of 7 mm), a 0.25 mm diameter Nitinol wire, a stainless steel adapter and a silicone tubing. The needle is assembled as shown in Figure 4.4. The stainless steel adapter is used to attach the magnetic tip and the Nitinol wire with a better alignment. The silicone tubing is utilized to avoid the thin Nitinol wire from slicing through the soft tissue. Two separate silicone tubes are used to encapsulate the tip and the adapter, and the adapter and Nitinol wire to ease the fabrication. The fabricated magnetic needle has 1.3 mm diameter at the tip and 0.7 mm diameter along the flexible body. The magnetic tip and the spherical joint are clearly visible in the fluoroscopic image as shown in Figure 4.4 (c).
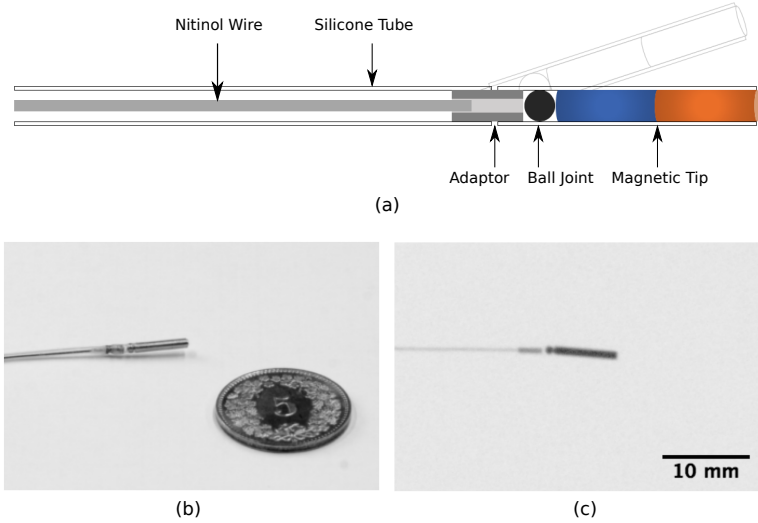
Figure 4.4 : Magnetic needle design. (a) Sketch of the magnetic needle. The needle tip consists of one cylindrical and one spherical NdFeB permanent magnet which is encased in a silicone tube. The adapter ring connects the spherical joint and the Nitinol wire. (b) The fabricated prototype of the magnetic needle. (c) The fluoroscopic image of the designed needle.

## 4.3.2 Brain Phantom Tissue

Agarose gel at a 0.6 % by weight concentration is commonly used as brain phantom because it closely resembles the brain with respect to its mechanical properties. It shows a similar force profile during needle insertion at slow insertion speeds [22].

The agarose gels used in the experiments were prepared by mixing agarose powder (Duchefa Biochemie B.V) and deionized water. The mixture was heated until all the powder had dissolved and then boiled for another 5 minutes. The solution was then poured into a rectangular container with dimensions of $15 \times 15 \times 5$ cm. The agarose gel was cooled down at room temperature for at least five hours.
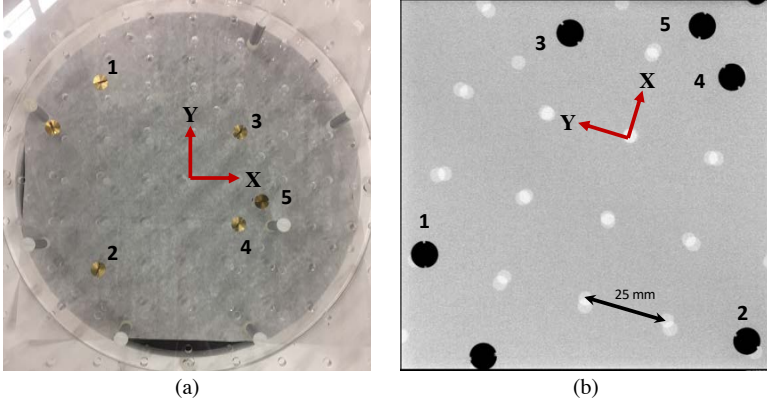
Figure 4.5 : Markers used for obtaining the transformation between the fluoroscopic device and the electromagnetic system. (a) Five bronze markers in the workspace of magnetic system. (b) A fluoroscopic image capturing the markers.

### 4.3.3 X-ray Fluoroscopic Visual Feedback

The same C-Arm fluoroscope described in Chapter 3 is used to provide visual feedback. The physical parameters for the fluoroscope device are provided in Table 3.1. The fluoroscopic images were taken at 8 Hz. A real-time image is displayed in one of the screens connected to the fluoroscope. This screen image with a resolution of $1280 \times 1024$ is captured and transmitted by connecting its display output port to a workstation PC where the APIs of Video4Linux kernel [23] was used.

To obtain a transformation matrix of a C-Arm fluoroscope with respect to our electromagnetic system, five bronze markers were embedded in the experimental stand as shown in Figure 4.5 (a). These markers are not affected by the magnetic system because bronze is a non-magnetic material, but are visible in the fluoroscopic image as shown in Figure 4.5 (b). The position of the markers is measured using a custom stereo vision system that was used for magnetic calibration. Using the calibration process that was utilized in Chapter 3, the transformation matrix between the fluoroscopic frame and the magnetic system frame is obtained. Under the current system configuration, the fluoroscopic field of view was limited to $75 \times 75$ mm in the XY-plane with an offset. In further experiments, the transformation matrix is automatically measured by the implemented program at the beginning of software run.

### 4.3.4 Magnetic Manipulation

An eight-coil configuration electromagnetic system is used for the experiment. The system allows for magnetic fields up to 90 mT. The magnetic workspace is a $10 \times 10 \times 10 \, \text{cm}^3$ cube. The magnetic field is calibrated to obtain a unit field contribution matrix $\mathcal{B}(\mathbf{P})$ in (4.3). The insertion of the magnetic needle is controlled by a custom wire feeder consisting of a DC motor (Maxon Motor 451095), two drive wheels, and the corresponding gearing.

The electromagnetic system and the needle advancer are controlled by a workstation PC (2.8 GHz Intel Xeon W3530 processor at 12GB RAM) running a custom control program written in C++.

### 4.3.5 Experimental Calibration

#### 4.3.5.1 Magnetic Needle Tip Flexibility

The flexibility of the magnetic needle tip is affected by a ball joint and an adapter that connect the tip and the needle shaft. The tissue reaction forces also influence the tip flexibility. In this section, the tip flexibility is characterized under the magnetic field at different directions and magnitudes. The needle was first inserted into the brain phantom and the magnetic field was applied. The tip direction was measured at a steady state when further rotation of the needle was no longer observed. Here, the direction of the needle tip and the magnetic field was measured from the Y-axis. The magnetic field with the magnitude of 40, 60, and 80 mT and the direction of $-90°$ to $90°$ was applied.

Figure 4.6 shows the fluoroscopic images of the needle under different magnetic fields at $-90°$, $0°$, and $90°$. The bending of the tip was clearly visible from 40 mT, and did not show any tip deflection variation as the field was changed from 60 mT to 80 mT. Therefore, 60 mT was chosen for further experiments. The magnetic torque was measured using (4.2). This torque tells the value of any reaction forces coming from the needle joint or the phantom tissues, which the magnetic torque could not overcome.

#### 4.3.5.2 Magnetic Needle Calibration

A kinematic model in (4.9) involves a parameter $l$, which is the distance offset between the steering wheel and the needle tip. This value is determined based on the physical properties of the soft tissue as well as on fabricated needle design.

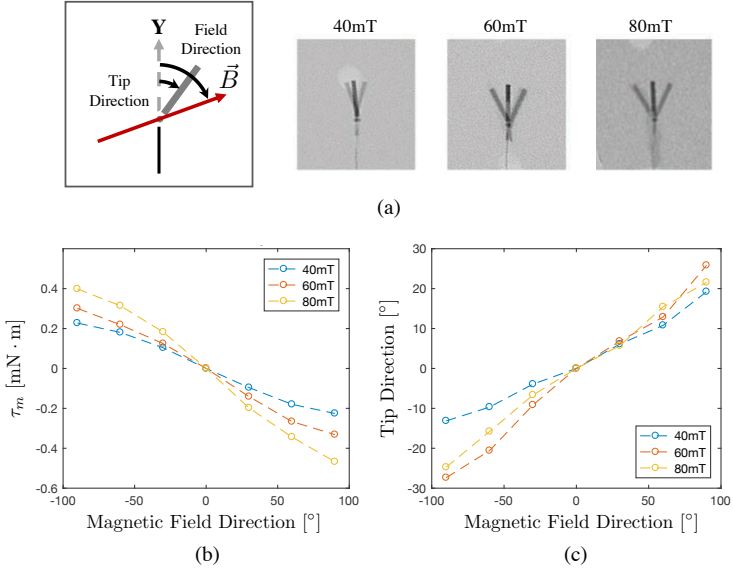The simulated trajectories of the magnetic needle are shown in Figure 4.7

(a)



(b)

(c)

Figure 4.6 : Magnetic tip deflection under the constant magnetic field at different direction and magnitude. (a) Composite fluoroscopic images of the magnetic tip. (b) The magnetic torque and (c) the tip direction as a function of the external magnetic field direction.

(a). The system required more time and insertion depth to align the needle tip direction to the field direction as $l$ increased. The needle trajectories with a determined parameter $l$ are also presented as a function of the field direction. This simulation has demonstrated the effect of the parameter $l$ and the magnetic field direction on the needle trajectory.

The distance offset $l$ can be experimentally estimated as follows. The magnetic needle was advanced into the brain phantom with the magnetic field directed along the insertion direction, which was in the Y-axis. Then, a magnetic field was set to a constant direction with a magnitude of 60 mT, while the needle was inserted with a velocity of 1 mm/s. This linear velocity was arbitrarily chosen within a range commonly used in the brain [24]. The needle was inserted with different magnetic field directions from −45° to 45° with increments of 15°. These experiments were repeated for five sets in three blocks of the brain phantom. For each insertion point, the order of the applied field direction was randomly chosen to minimize any biased results. Figure 4.7 (b) shows the composite fluoroscopic
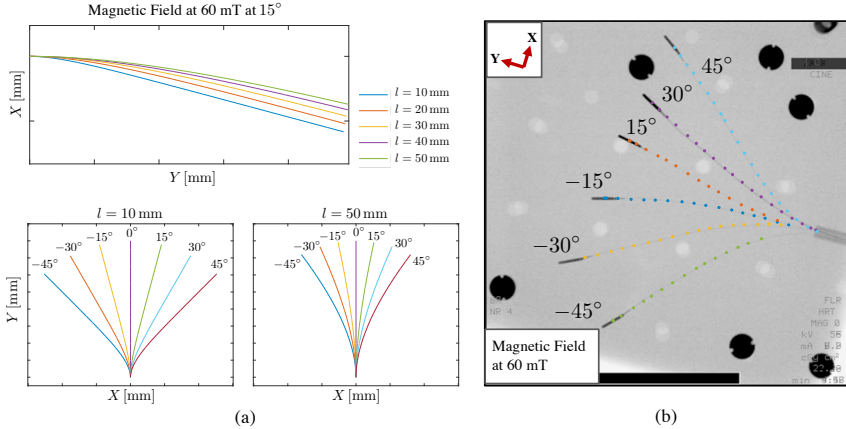
Figure 4.7 : Needle trajectories under different magnetic field direction. (a) Simulation results for the needle trajectories as a function of the distance parameter $l$ and the direction of the magnetic field. (b) The composite fluoroscopic images of the needle after insertion. Tracking results of the tip are shown with color dots for every ten frames, i.e., for every 1.2 s.

images of the needle after insertion for one experimental set. It shows the final needle paths at different magnetic field direction, and the tracking results are also presented with color dots for every ten frames, i.e., for every 1.2 seconds. It is worthy to note that the overlaid tracking results are synchronized with the final needle paths. This implies that the needle shaft had followed the trajectory of the needle tip, which was one of the assumptions in the kinematic model.

In (4.9), the time-derivative of the heading vector $\mathbf{h}$ corresponds to the field direction $\mathbf{B}$ and the distance offset $l$. This is also a function of the angular velocity, as

$$\dot{\mathbf{h}} = \frac{\mathbf{h} \times (\mathbf{B} \times \mathbf{h})}{l(\mathbf{B} \cdot \mathbf{h})} v_I = \omega \times \mathbf{h}. \tag{4.24}$$

From that relation, the parameter $l$ is estimated as $l \approx r \dfrac{\|\mathbf{B} \times \mathbf{h}\|}{\mathbf{B} \cdot \mathbf{h}}$ where $r$ is the radius of the circle fitted to the trajectory. Figure 4.8 shows the needle calibration results for a run with the magnetic field at $-45°$. The measured needle tip trajectory was fitted with a window size of 16 mm, resulted in a maximum curvature of $0.0286 \, \text{mm}^{-1}$ at the beginning of the insertion. The insertion started with the maximum directional difference between the needle tip and the magnetic field. The directional change of the needle mostly occurred
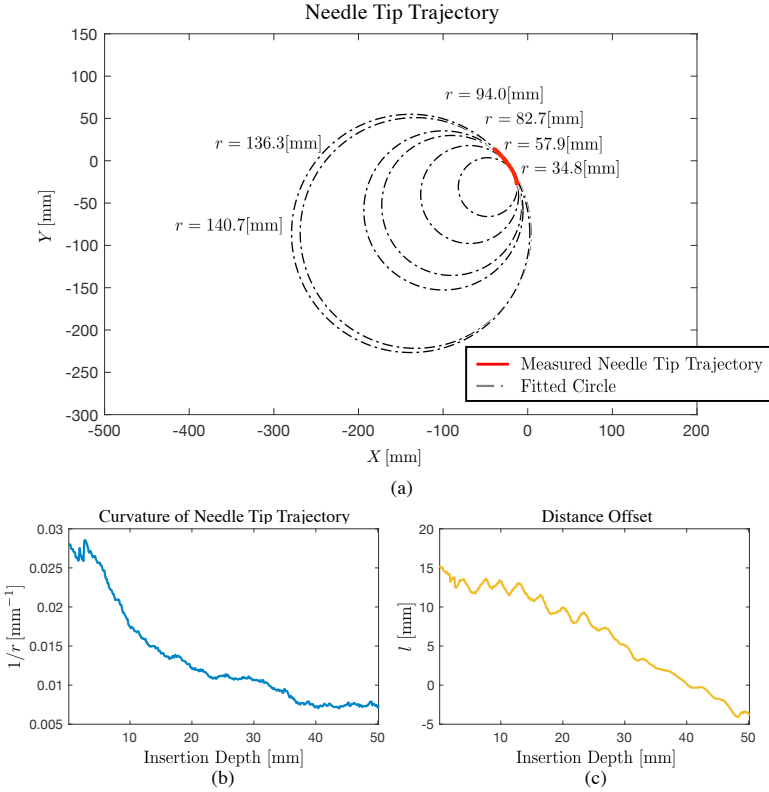
Figure 4.8 : Magnetic needle calibration for the distance parameter $l$. (a) Measured needle tip trajectory depicted with fitted circles for every eighty measurements. The 16 mm size of a circle was used for circular fitting. (b) Curvatures of the trajectory as a function of the insertion depth. (c) The resultant value of the parameter $l$, estimated using the trajectory curvatures and the directions of the magnetic tip and the external field.

at the beginning. Within this range, the distance offset was measured around 15 mm as shown in Figure 4.8 (c). As the insertion proceeded and the needle tip aligned to the magnetic field, further changes on the needle direction nor on the curvature were observed. This led to a decrease in the estimated distance offset. Since the value of $l$ corresponds to the maneuverability of the magnetic needle, the most conservative value should be chosen for the model. Therefore, the maximum value was selected. From five sets of the experiments (in total,

69

thirty insertions), the distance offset was chosen as 19.07 mm.

## 4.4 Experimental Results for Trajectory Following

### 4.4.1 Experiments with Brain Phantom

The calibrated magnetic needle was steered to follow the predefined trajectories, using the experimental setup discussed in the previous section. First, the experiments were performed in the agarose brain phantom. The magnetic needle was inserted along the Y-axis of the setup, therefore, the coordinate system was 90° transformed in the Z-axis to adapt the control strategy where the X-axis was assumed to be the insertion direction. The magnitude of the external magnetic field was set to 60 mT, and the maximum insertion velocity was limited to 1 mm/s. The control gains that were used in the experiments are $(k_1, k_2, k_3) = (0.1, 0.05, 0.05)$. In the experiment, the trajectories were determined by using the relative position to the initially measured tip position, and restrained in the XY-plane. At each time step, the target position was defined by determining the closest position from the measured tip position and setting ahead of a certain threshold from that position.

First, the proposed magnetic needle steering approach was tested for straight paths. The experimental results are shown in Figure 4.9. Three figures in the first row describe the measured tip position compared to the desired path. These graphs present the relative position to the initial position, therefore, all the trajectories start from zero. The final shapes of the flexible needle are shown in the bottom row, which are overlaid with the measured tip position for every 10 s. The first column shows the results of zero offset at its initial position. Three repetition of the experiments resulted in a root mean square error of 0.91 mm with standard deviation of 0.38 mm along the trajectories. The same experiments were performed when the initial position is off by 5 mm and 10 mm in the X-axis to the desired trajectory. The flexible needle could reach the straight path within ten percent of its initial discrepancy after 29 mm and 32 mm insertion. Furthermore, overshoots of 0.43 mm and 1.52 mm we observed for initial offsets of 5 mm mm and 10 mm, respectively. The steady-state errors due to this initial discrepancy were observed. This may converge to the desired trajectory, however, it was not visible within the fluoroscopic field of view.

The experimental results for the following curved trajectories are shown in Figure 4.10. Three paths with constant curvatures of 0.0015, 0.0038, and
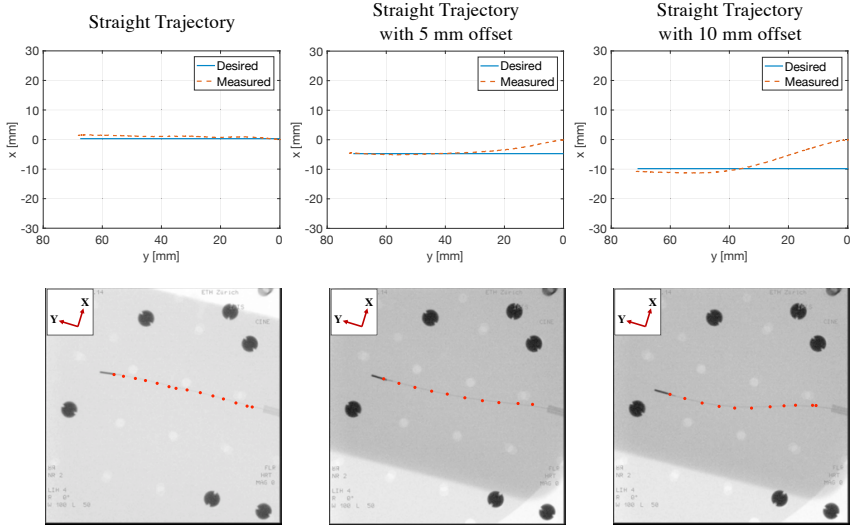
Figure 4.9 : Experimental results for following straight paths with 0, 5, and 10 mm initial offset in the X-axis. The plots in the first row describe the measured tip trajectories and the desired straight path. The images in the bottom row show the fluoroscopic images after insertion. The measured tip position is shown for every 80 frames, i.e., for every 10 s.

$0.0085\,\mathrm{mm}^{-1}$ and two paths with double-bend trajectories were tested. These experiments on average resulted in a root mean square error of 0.59 mm with a standard deviation of 0.53 mm. NB: In the second experiment for the constant curvature path, the initial heading direction was off by 7.47° from the Y-direction, which may cause errors in the beginning of the insertion.

Figure 4.10 : Experimental results for following constant curvature paths and double-bend paths. The plots describe the measured tip trajectories and the desired path and the images show the fluoroscopic images after insertion. The measured tip position is shown for every 80 frames, i.e., for every 10 s.
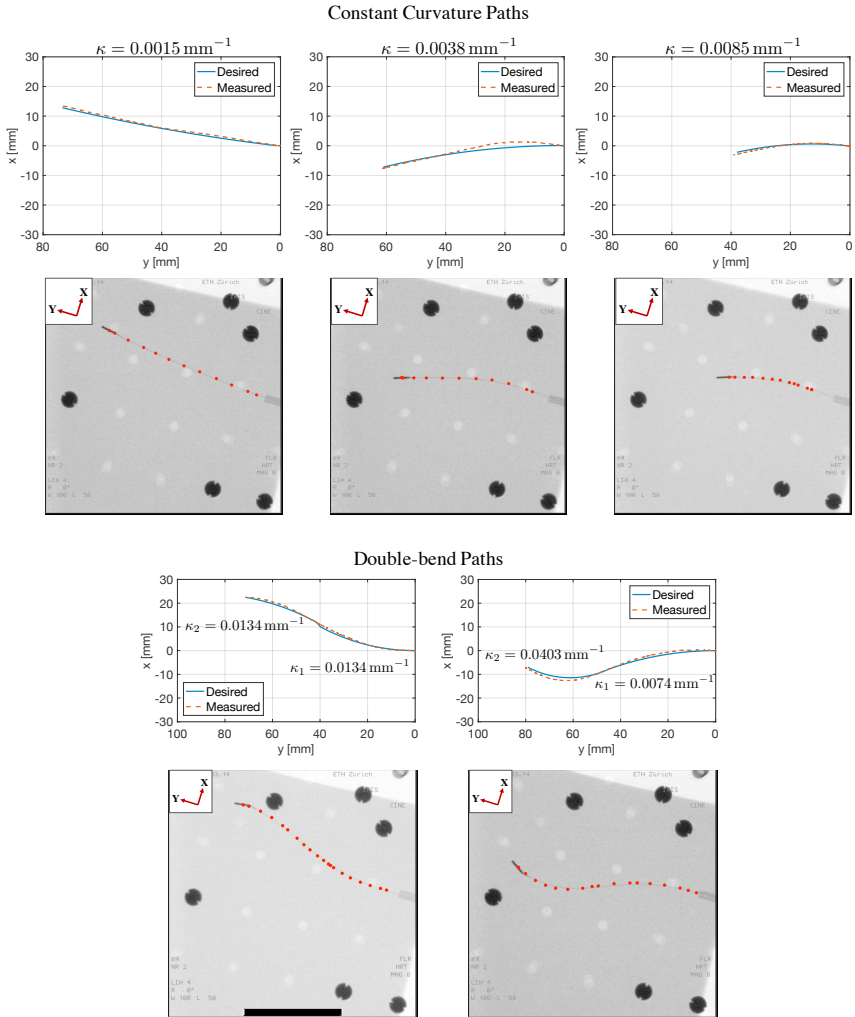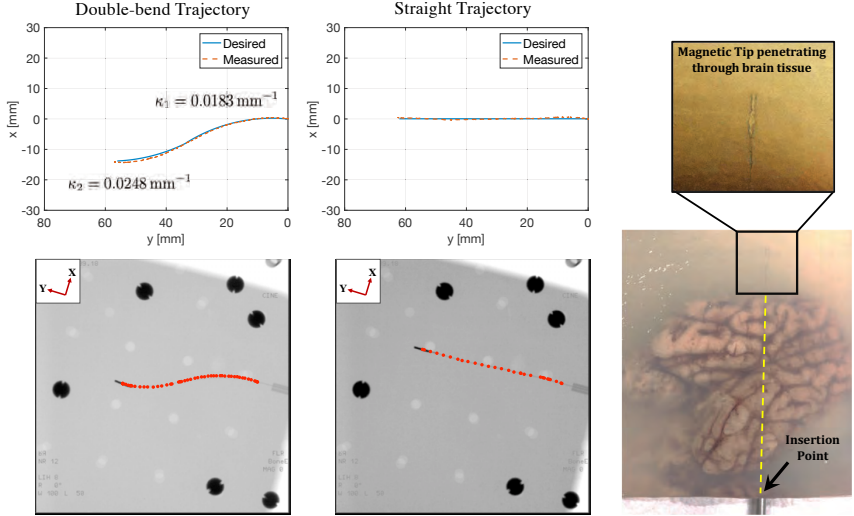
Figure 4.11 : Experimental results for following trajectories in biological tissue. The magnetic needle was first guided for a double-bend trajectory and second for a straight trajectory. The images in the bottom row show the fluoroscopic images after insertion. The measured tip position is shown for every 40 frames, i.e., for every 5 s. The third column of plots shows the camera image of the magnetic needle penetrating through brain tissue after the straight insertion.

### 4.4.2 Experiments with *ex vivo* Pig Brain

An *ex vivo* pig brain was utilized to show the feasibility of steering a magnetic needle in an inhomogeneous environment. The dissected pig brain was embedded in 0.6% agarose gel to fixate it during the experiments as shown in Figure 4.3. The same control gains in 4.4.1 were utilized. The magnetic needle was first guided to a double-bend trajectory with curvatures of 0.0183 and $0.0248\,\mathrm{mm}^{-1}$, retracted to the initial position, and then steered to follow a straight trajectory. The experiments resulted in an accuracy of $0.37 \pm 0.29\,\mathrm{mm}$ and $0.27 \pm 0.25\,\mathrm{mm}$, for the curved and straight paths, respectively. This is comparable to the experimental results in a homogeneous phantom. As shown in Figure 4.11, the brain tissue and its embedded agarose gel were not clearly distinguishable in the fluoroscopic image. The camera image confirmed that the magnetic needle actually penetrated through the brain tissue while following the desired straight path.

## 4.5 Discussion

Navigation of the magnetic flexible needle within soft tissue environment was investigated in this chapter. The kinematic model for guiding magnetic needles was adapted from a nonholonomic bicycle model. The magnetic needle tip tries to align its direction to the external magnetic field. However, due to tissue interaction forces and the stiffness of the needle joint, there is a discrepancy between two different directions. This is imposed in the nonholonomic bicycle model as the virtual front wheel that steers the needle tip. Since this model does not guarantee system stability by using a time-invariant feedback, it was transformed to a two-chain, single-generator chained form.

The proposed approach was validated with experiments using *in vitro* brain phantom and *ex vivo* pig brain. The X-ray fluoroscopy and electromagnetic manipulation were utilized as the imaging and actuating devices, which eased the clinical feasibility of the method. In agarose brain phantom, it was possible to navigate the magnetic needle by following straight paths, constant curvature paths, and double-bend paths within a millimeter tracking errors along the trajectory. In biological tissue such as dissected pig brain, the magnetic needle was able to follow the straight path and curved path with a comparable accuracy. The control strategy was also tested for a small discrepancy at its initial position. This experiment showed the convergence of the needle path to the desired trajectory after a certain time. However, some overshoot and steady-state errors were also observed. There are two approaches that could improve this issue. One approach is to optimize the control gains in (4.23). The control gains $k_1$ is mainly correspondent to the insertion speed, while $k_2$ and $k_3$ are in charge of steering the tip angles. The different combination of these gains, thus, places various emphasis on the insertion speed and the tip steering rate. The other approach is to better select a target position. The target position is chosen along the trajectory with a certain threshold ahead of the current closest point. With a small threshold, the desired trajectory could be reached in a short time though it may cause an overshoot or oscillations, which are not desirable in surgical applications. However, a large threshold on the target selection could reduce the accuracy of the trajectory following.

The experiments described in this chapter targeted paths in the XY-plane. However, the fluoroscopic tracking and the control scheme were implemented in three dimensions. As investigated in Chapter 3, the poor localization accuracy of using a fluoroscopic image can be overcome by combining sequential images from

different views. Future work can include the implementation of the method which requires freely rotated fluoroscope and validate the magnetic needle steering in 3D.

## References

[1] R. J. Webster and B. A. Jones, "Design and kinematic modeling of constant curvature continuum robots: A review," *Int J Rob Res*, vol. 29, no. 13, pp. 1661–1683, 2010.

[2] G. Dogangil, B. Davies, and F. Rodriguez y Baena, "A review of medical robotics for minimally invasive soft tissue surgery," *Proc Inst Mech Eng H*, vol. 224, no. 5, pp. 653–679, 2010.

[3] N. J. Cowan, K. Goldberg, G. S. Chirikjian, G. Fichtinger, R. Alterovitz, K. B. Reed, V. Kallem, W. Park, S. Misra, and A. M. Okamura, "Robotic needle steering: Design, modeling, planning, and image guidance," in *Surgical Robotics*, Springer, 2011, pp. 557–582.

[4] A. M. Okamura, C. Simone, and M. D. O'Leary, "Force modeling for needle insertion into soft tissue," *IEEE Trans Biomed Eng*, vol. 51, no. 10, pp. 1707–1716, 2004.

[5] J. A. Engh, D. S. Minhas, D. Kondziolka, and C. N. Riviere, "Percutaneous intracerebral navigation by duty-cycled spinning of flexible bevel-tipped needles," *Neurosurgery*, vol. 67, no. 4, pp. 1117–1123, 2010.

[6] D. S. Minhas, J. A. Engh, M. M. Fenske, and C. N. Riviere, "Modeling of needle steering via duty-cycled spinning," in *Conf Proc IEEE Eng Med Biol Soc*, IEEE, 2007, pp. 2756–2759.

[7] P. J. Swaney, J. Burgner, H. B. Gilbert, and R. J. Webster, "A flexure-based steerable needle: High curvature with reduced tissue damage," *IEEE Transac Biomed Eng*, vol. 60, no. 4, pp. 906–909, 2013.

[8] N. J. van de Berg, J. Dankelman, and J. J. van den Dobbelsteen, "Design of an actively controlled steerable needle with tendon actuation and FBG-based shape sensing," *Med Eng Phys*, vol. 37, no. 6, pp. 617–622, 2015.

[9] T. K. Adebar, J. D. Greer, P. F. Laeseke, G. L. Hwang, and A. M. Okamura, "Methods for improving the curvature of steerable needles in biological tissue," *IEEE Trans Biomed Eng*, vol. 63, no. 6, pp. 1167–1177, 2016.

[10] S. Pattanshetti and S. C. Ryu, "Design and fabrication of laser-machined hinge joints on miniature tubes for steerable medical devices," *J Mech Robot*, vol. 10, no. 1, p. 011 002, 2018.

[11] S. C. Ryu, Z. F. Quek, J.-S. Koh, P. Renaud, R. J. Black, B. Moslehi, B. L. Daniel, K.-J. Cho, and M. R. Cutkosky, "Design of an optically controlled mr-compatible active needle," *IEEE Trans Rob*, vol. 31, no. 1, pp. 1–11, 2015.

[12] S. Y. Ko, L. Frasson, and F. R. y Baena, "Closed-loop planar motion control of a steerable probe with a programmable bevel inspired by nature," *IEEE Trans on Rob*, vol. 27, no. 5, pp. 970–983, 2011.

[13] A. J. Petruska, F. Ruetz, A. Hong, L. Regli, O. Sürücü, A. Zemmar, and B. J. Nelson, "Magnetic needle guidance for neurosurgery: Initial design and proof of concept," in *IEEE Int Conf Robot Autom*, May 2016, pp. 4392–4397.

[14]   E. P. Furlani, *Permanent magnet and electromechanical devices: materials, analysis, and applications*. Academic press, 2001.

[15]   R. J. Webster, J. S. Kim, N. J. Cowan, G. S. Chirikjian, and A. M. Okamura, "Nonholonomic modeling of needle steering," *Int J Rob Res*, vol. 25, no. 5-6, pp. 509–525, 2006.

[16]   R. M. Murray, Z. Li, and S. S. Sastry, *A mathematical introduction to robotic manipulation*. CRC press, 1994.

[17]   R. W. Brockett, "Asymptotic stability and feedback stabilization," *Differential geometric control theory*, vol. 27, no. 1, pp. 181–191, 1983.

[18]   R. M. Murray and S. S. Sastry, "Steering nonholonomic systems in chained form," in *Proc IEEE Conf Decis Control*, IEEE, 1991, pp. 1121–1126.

[19]   A. Isidori, *Nonlinear control systems*. Springer Science & Business Media, 2013.

[20]   L. G. Bushnell, D. M. Tilbury, and S. Sastry, "Steering three-input nonholonomic systems: The fire truck example," *Int J Rob Res*, vol. 14, no. 4, pp. 366–381, 1995.

[21]   A. De Luca, G. Oriolo, and C. Samson, "Feedback control of a nonholonomic car-like robot," *Robot motion planning and control*, pp. 171–253, 1998.

[22]   M. A. Howard, B. A. Abkes, M. C. Ollendieck, M. D. Noh, C. Ritter, and G. T. Gillies, "Measurement of the force required to move a neurosurgical probe through in vivo human brain tissue," *IEEE Trans Biomed Eng*, vol. 46, no. 7, pp. 891–894, 1999.

[23]   LinuxTV, Available at: https://www.linuxtv.org/.

[24]   K. Miller, K. Chinzei, G. Orssengo, and P. Bednarz, "Mechanical properties of brain tissue in-vivo: Experiment and computer simulation," *J Biomech*, vol. 33, no. 11, pp. 1369–1376, 2000.

# Chapter 5

# Neurosurgical Planning
for Flexible Needles

This chapter proposes a surgical planning approach for flexible needles, including the magnetically guided needle discussed in the previous chapter. Computer-assisted planning methods have been suggested to support neurosurgeons by saving planning time and improving insertion safety [1], [2]. The suggested trajectories from automatic planning algorithms are accepted upon evaluation by the neurosurgeon [3], [4]. However, the planning methods currently available in clinics are only focused on straight paths. For a curved path, the planning becomes less intuitive and needs to account for different surgical and physical constraints. Furthermore, the motion interaction of flexible needles with soft tissues and the control efforts to guide them should be considered.

The motion planning problem for flexible needles has been previously analyzed in the literature. A Markov decision process has been adapted to compute discretized inputs to steer a flexible bevel-tip needle [5] and sampling-based algorithms like rapidly-exploring random tree (RRT) combined with the reachability-guided strategy has been presented in three-dimensional environments [6]. An RRT-based algorithm was also suggested to deal with nonholonomic constraints of flexible needles by using a distance metric approach [7]. In addition, a continuous curvature model is proposed to find the optimal path for flexible needles in neurosurgical application [8]. However, it was only demonstrated in 2D. The full 3D neurosurgical planning method for flexible needles has yet to be developed.

In this chapter, an RRT$^*$ sampling-based approach proposed in [9] is adopted to incorporate the physical constraints coming from the magnetic flexible nee-

dle. The planning approach with its algorithmic method and cost function is introduced in section 5.1. The surgical constraints in deep brain stimulation are presented in section 5.2. In section 5.3, the proposed path planning method is simulated on a realistic 3D CAD model of the brain for two scenarios. The first explores the common case of the Parkinson's disease treatment which targets the subthalamic nucleus. The second scenario is the treatment of mild Alzheimer's disease which targets the fornix.

## 5.1 Planning Approach

### 5.1.1 Algorithm

The overall planning algorithm is described in Algorithm 1. For a given entry point and a target region, the algorithm computes feasible paths by optimizing the cost function while satisfying surgical constraints discussed.

First, it is evaluated if there exists a linear or a constant curvature path directly reaching the target region from the entry point (line 2–7 in Algorithm 1) without penetrating the obstacles. Then, an RRT* based planning algorithm [9] is used to perform a reachability test, which considers the minimum bend radius of the flexible needle (line 8–32 in Algorithm 1). The tree $T$ is explored iteratively until it reaches the goal region $Q_{\text{goal}}$. The tree is structured with $V$ which is the set of vertices $q$ and edges $E$ connecting the vertices. Each vertex includes the information about its three-dimensional (3D) position and heading direction, cost, and parent vertex as $q_{\text{pos}}$, $q_{\text{head}}$, $q_{\text{cost}}$, and $q_{\text{parent}}$, respectively. The heading information is important since later it is considered in the reachability test. The cost of vertices or edges is defined by `Cost`. `Cost`$(q)$ defines the minimum cost to reach the vertex $q$ from the initial entry point or returns $q_{\text{cost}}$ and `Cost`$(E(q_1, q_2))$ determines the cost of the edge connecting two vertices $q_1$ and $q_2$. The cost function will be discussed in details later in section 5.1.2.

At each iteration, the 3D position of $q_{\text{rand}}$ is randomly sampled in the obstacle free space by `SampleFree`. Then the function `NearestReachable` determines the closest vertex from $q_{\text{rand}}$ to $q_{\text{nearest}}$ among the existing vertices (see Figure 5.1). Prior to considering its closeness, $q_{\text{rand}}$ should be reachable from the existing vertices which implies that the edge connecting two vertices has a curvature $\kappa$ smaller than $\frac{1}{r_{\text{min}}}$ as

$$\kappa = \frac{2\|(q_{\text{rand.pos}} - q_{\text{reach.pos}}) \times q_{\text{reach.head}}\|}{\|q_{\text{rand.pos}} - q_{\text{reach.pos}}\|^2} < \frac{1}{r_{\text{min}}}. \tag{5.1}$$

---

**Algorithm 1:** Motion Planning Algorithm

---

**1** $V \leftarrow \{q_{\text{init}}\}, E \leftarrow \emptyset, c_{\text{min}} \leftarrow 0, P \leftarrow \emptyset$

**2** **if** *LinearPath*$(q_{\text{init}}, Q_{\text{goal}})$ **then**        /* check a linear path */

**3**    $P \leftarrow P \cup \texttt{Line}(q_{\text{init}}, Q_{\text{goal}})$

**4** **end**

**5** **if** *ArcPath*$(q_{\text{init}}, Q_{\text{goal}})$ **then** /* check a constant curvature path */

**6**    $P \leftarrow P \cup \texttt{Arc}(q_{\text{init}}, Q_{\text{goal}})$

**7** **end**

**8** **while** $T \cap Q_{\text{goal}} = \emptyset$ **and** $k < N$ **do**

**9**    $q_{\text{rand}} \leftarrow \texttt{SampleFree}$

**10**    $q_{\text{nearest}} \leftarrow \texttt{NearestReachable}(T, q_{\text{rand}})$

**11**    $q_{\text{new}} \leftarrow \texttt{Steer}(q_{\text{nearest}}, q_{\text{rand}})$

**12**    **if** *CollisionFree*$(q_{\text{nearest}}, q_{\text{new}})$ **then**

**13**       $Q_{\text{near}} \leftarrow \texttt{NearReachable}(T, q_{\text{new}}, r)$

**14**       $V \leftarrow V \cup \{q_{\text{new}}\}$

**15**       $q_{\text{min}} \leftarrow q_{\text{nearest}}$

**16**       $c_{\text{min}} \leftarrow \texttt{Cost}(q_{\text{nearest}}) + \texttt{Cost}(E(q_{\text{nearest}}, q_{\text{new}}))$

**17**       **foreach** $q_{\text{near}} \in Q_{\text{near}}$ **do**   /* connect through a minimum-cost path */

**18**          **if** *CollisionFree*$(q_{\text{near}}, q_{\text{new}})$ **and** $Cost(q_{\text{near}}) + Cost(E(q_{\text{near}}, q_{\text{new}})) < c_{\text{min}}$ **and** $\kappa(q_{\text{near}}, q_{\text{new}}) < \frac{1}{r_{\text{min}}}$ **then**

**19**             $q_{\text{min}} \leftarrow q_{\text{near}}$

**20**             $c_{\text{min}} \leftarrow \texttt{Cost}(q_{\text{near}}) + \texttt{Cost}(E(q_{\text{near}}, q_{\text{new}}))$

**21**          **end**

**22**       **end**

**23**       $E \leftarrow E \cup \{q_{\text{min}}, q_{\text{new}}\}$

**24**       **foreach** $q_{\text{near}} \in Q_{\text{near}}$ **do**             /* rewire the tree */

**25**          **if** *CollisionFree*$(q_{\text{new}}, q_{\text{near}})$ **and** $Cost(q_{\text{new}}) + Cost(E(q_{\text{new}}, q_{\text{near}})) < Cost(q_{\text{near}})$ **and** $\kappa(q_{\text{near}}, q_{\text{new}}) < \frac{1}{r_{\text{min}}}$ **then**

**26**             $q_{\text{parent}} \leftarrow \texttt{Parent}(q_{\text{near}})$

**27**             $E \leftarrow (E \setminus \{(q_{\text{parent}}, q_{\text{near}})\}) \cup \{(q_{\text{new}}, q_{\text{near}})\}$

**28**          **end**

**29**       **end**

**30**    **end**

**31**    $k \leftarrow k + 1$

**32** **end**

**33** $P \leftarrow P \cup \texttt{Path}(T)$

**34** $P_{\text{goal}} \leftarrow \texttt{OptimalPath}(P)$

---

- Determine $q_{new}$



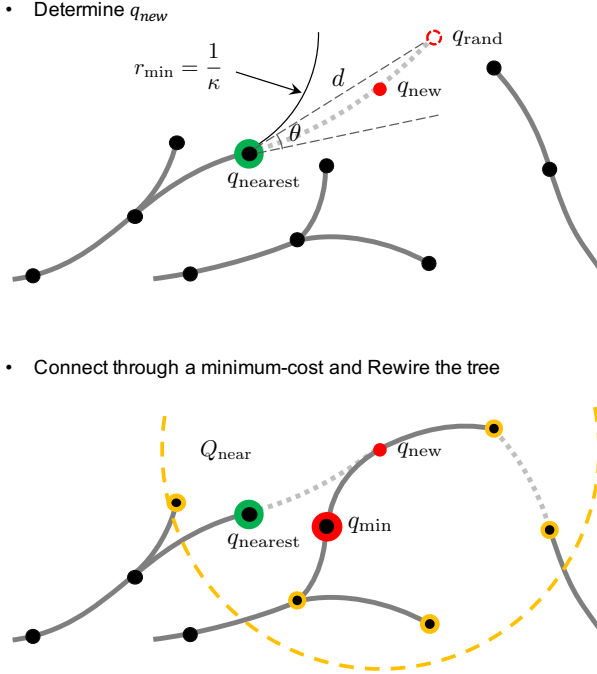- Connect through a minimum-cost and Rewire the tree



Figure 5.1 : Scheme of RRT$^*$ based path planning. Black spheres represent the existing vertices $q \in V$ and the lines indicate the edges. Yellow spheres show the vertices in the set $Q_{near}$. (top) Determine $q_{nearest}$ to $q_{rand}$ among the existing vertices using the distance measure. Steer to $q_{new}$ with a reachability test regarding the minimum bend radius of the flexible needle. (bottom) Connect $q_{new}$ through $q_{min}$ which gives the minimum cost among the vertices nearby $q_{new}$. Rewire $q_{near}$ through $q_{new}$ if it gives better cost than through its parent.

Once the set of reachable vertices from $q_{rand}$ is obtained, the nearest one is obtained by using the distance measure $\rho$ as [10]

$$\rho = w_d d^2 + w_\theta (1 - |\cos \theta|)^2 \tag{5.2}$$

where $d$ and $1 - |\cos \theta|$ are measures in Euclidean distance and orientation and $w_d$ and $w_\theta$ are the weights for each measure satisfying $w_d + w_\theta = 1$. Here the distance measure is normalized by the maximum distance between two vertices available in the space. By incorporating the position and orientation in the distance measure, it is possible to penalize the vertex which is near but requiring

a large effort to curve.

The vertex bringing the minimum distance measure is selected for $q_{\text{nearest}}$. Then the new vertex $q_{\text{new}}$ is decided by steering the nearest one to the random vertex with a certain distance $\eta > 0$ by `Steer`. Since the feasible path for the flexible needle can only be a continuous and smooth path, $q_{\text{nearest}}$ and $q_{\text{new}}$ is connected with a straight line or a constant curvature curve. The straight line is first checked if it is feasible. If not, then the path with a constant curvature is considered. Then, the heading direction $q_{\text{new.head}}$ is obtained following the determined path.

If this edge avoids collisions with obstacles by `CollisionFree`, it becomes one candidate for the path. Then the steps in RRT$^*$ are followed to decide the optimal path. The set of vertices near to $q_{\text{new}}$ is defined as $Q_{\text{near}}$ using `Near` which is the set of vertices in $V$ being contained in a ball of radius $r$ centered at $q_{\text{new}}$. The radius is defined as

$$r = \min\left\{\gamma(\log(\text{card}(V))/\text{card}(V))^{(1/d)}, \eta\right\} \tag{5.3}$$

where $\text{card}(V)$ is the number of vertices in the tree, $d$ is the dimension of the space, and $\gamma$ is a constant [9].

If there exists a vertex giving lower cost than the current nearest one in $Q_{\text{near}}$, then $q_{\text{new}}$ is connected to that one (line 18–23 in Algorithm 1). Also, if any vertex in $Q_{\text{near}}$ gives lower cost through $q_{\text{new}}$ than through its parent, it is rewired to $q_{\text{new}}$ (line 24–29 in Algorithm 1). Here the vertices are connected only if they satisfy the curvature condition in (5.1). These procedures suggested in RRT$^*$ algorithm provide solutions converging to an optimal solution with reasonable computational complexity. As the number of vertexes increases, the best path from the initial configuration to the target region changes toward having minimal cost. Lastly, the path is determined by searching backward from the goal region to the initial point. Among the feasible paths derived from the algorithm, the final best path is determined as the one with the minimum cost.

### 5.1.2 Cost Function

The goal of planning algorithm is to find the safest path with the least effort to steer the flexible needle to the target region. This criterion is determined using a cost function in the planning algorithm. Two different cost terms are considered to penalize the path length and the distance from obstacles.

For a given edge $E$ connecting two vertices $q_1$ and $q_2$, the cost term $f_L$ is
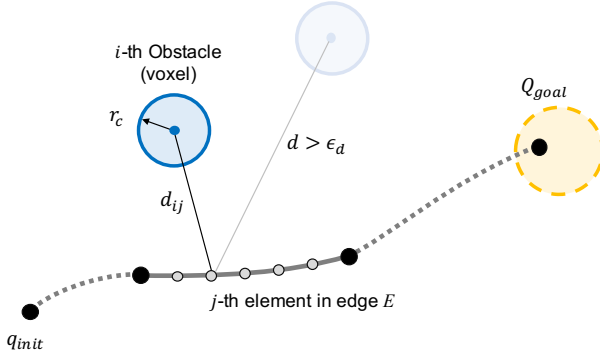
Figure 5.2 : The edge connecting two vertices satisfying the collision-free condition, $d_{ij} > r_c$. In the cost function, $f_D$ measures the safety of the path. The obstacles located further than $\epsilon_d$ from the path is not taken into consideration.

defined as

$$f_L = \frac{L}{L_{min}} \qquad (5.4)$$

where $L$ is the length of the edge and $L_{min}$ is the minimum distance between $q_1$ and $q_2$. When the path is straight, $f_L$ is minimum. On the contrary, as the path gets toward a circuitous one, it results in a larger cost. This presents the efficiency of the path since it relates to the insertion time of the needle. Also, it indicates the effort necessary to steer the needle.

On the other hand, the cost term $f_D$ incorporates the safety of the path by considering the distance from the path to the obstacles as

$$f_D = \frac{1}{N_o N_E} \sum_i^{N_o} \sum_j^{N_E} \frac{\epsilon_d - r_c}{d_{ij} - r_c}$$

$$d_{ij} = \begin{cases} d_{ij} & \text{if } r_c < d_{ij} \le \epsilon_d \\ \epsilon_d & \text{if } \epsilon_d < d_{ij} \end{cases} \qquad (5.5)$$

where $N_o$ and $N_E$ are the number of obstacles and elements in the edge, and $r_c$ is the hard limit for obstacle avoidance. Therefore, paths approaching obstacles with distances inferior to $r_c$ are rejected by `CollisionFree`. On the other hand, obstacles located farther than $\epsilon_d$ are not penalized. The distance $d_{ij}$ is measured for each obstacle $i$ to each element $j$ in the edge described in Figure 5.2.

By adjusting the positive weights $a_1$ and $a_2$, the cost function regulates the
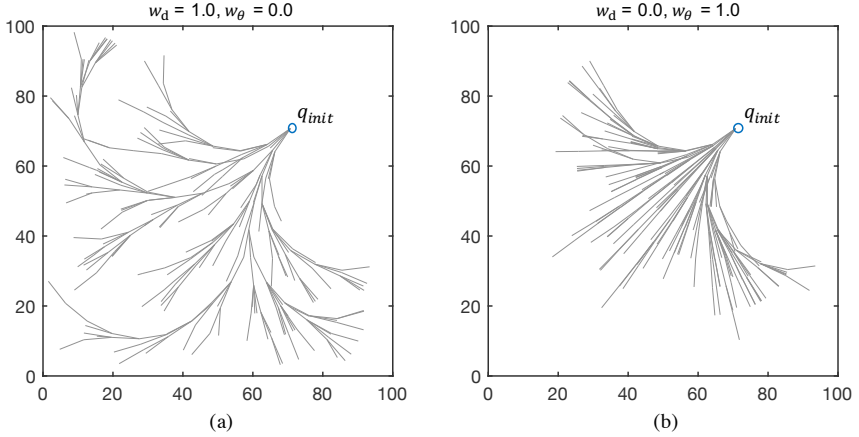
Figure 5.3 : A comparison of tree structures with different coefficients for the distance measure (a) $w_d = 1.0$, $w_\theta = 0.0$ and (b) $w_d = 0.0$, $w_\theta = 1.0$. The grey edges formed by the algorithm are shown for $N = 500$. The steering distance $\eta$ and the minimum radius $r_{\min}$ is set to 8 and 20, respectively.

relative importance of each measure as

$$\mathbf{cost}(E) = a_1 f_L + a_2 f_D \tag{5.6}$$

with the sum of weights equal to 1. Different weighting coefficients lead to different optimal paths. However, the choice of weights is highly dependent on the clinical cases and the surgeons' preference.

### 5.1.3 Discussion

The choice of the path planner parameters, namely, the weights for the distance measure $w_d$ and $w_\theta$ in (5.2), the cost coefficients $a_1$ and $a_2$ in (5.6), and the number of iterations $N$, have an influence on the determined final paths.

The tree structure grows depending on how to choose the nearest vertex, which is mainly determined by the distance measure. As the Euclidean distance is only considered in Figure 5.3 (a), the algorithm chooses the vertex which is closest to the vertex $q_{\mathrm{rand}}$ as $q_{\mathrm{nearest}}$. This results in a circuitous tree map compared to the one explored with the distance measure only considering orientation in Figure 5.3 (b).

The cost in (5.6) also affects the growth of RRT*-tree by rewiring the existing
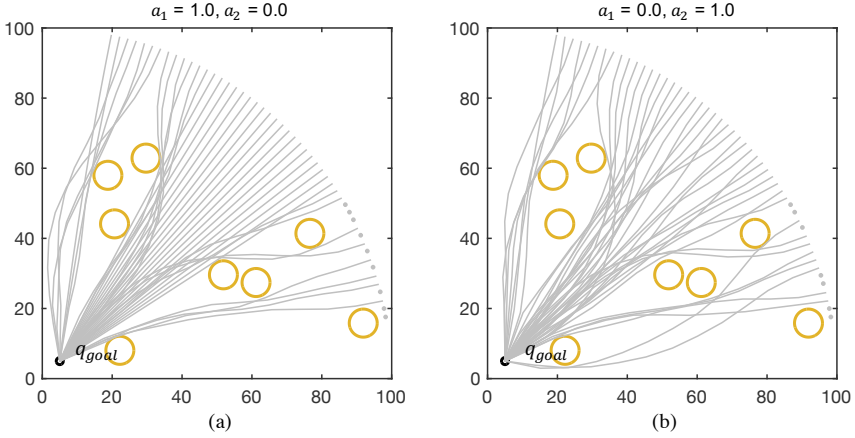
Figure 5.4 : A comparison of path planning results by using different cost weights (a) $a_1 = 0$, $a_2 = 1$ and (b) $a_1 = 1$, $a_2 = 0$. The algorithm was ran for $N = 500$, $\eta = 8$, $r_{\min} = 40$, $w_d = 0.5$, and $w_\theta = 0.5$. The grey dots indicate the initial configurations that the algorithm could not find the feasible path within iterations. The grey paths present the best trajectory for every initial configurations.

edge with the one giving minimal cost. Figure 5.4 shows the path planning result from several initial configurations to the same goal position using different cost coefficients. Fifty different initial configurations are equally spaced along the circle and obstacles are randomly selected. Each grey line shows the best path, the one with the minimal cost for each initial configuration. The cost weights not only affect the exploration of the tree, but also the selection of the best path among a set of feasible paths and entry points. When the cost coefficient for path length $a_1$ is set to one, the shortest path is selected as long as the path avoids collision with obstacles in Figure 5.4 (a). Mostly the straight path directly connecting the initial point to the goal is selected. On the contrary, the safest path is chosen when the cost coefficient for obstacle avoidance $a_2$ is set to one in Figure 5.4 (b). In this case, the iterative method brings primarily the best path. These parameters, however, do not affect the feasibility of the generated paths but only the length of the path and the distance to obstacles.

The choice of the number of iterations is a trade-off between the optimality of the path and the computing time. This number should be high enough to figure out at least one feasible path. For example, the edges formed by the iterative method cannot reach the goal region within 50 iterations and thus fails
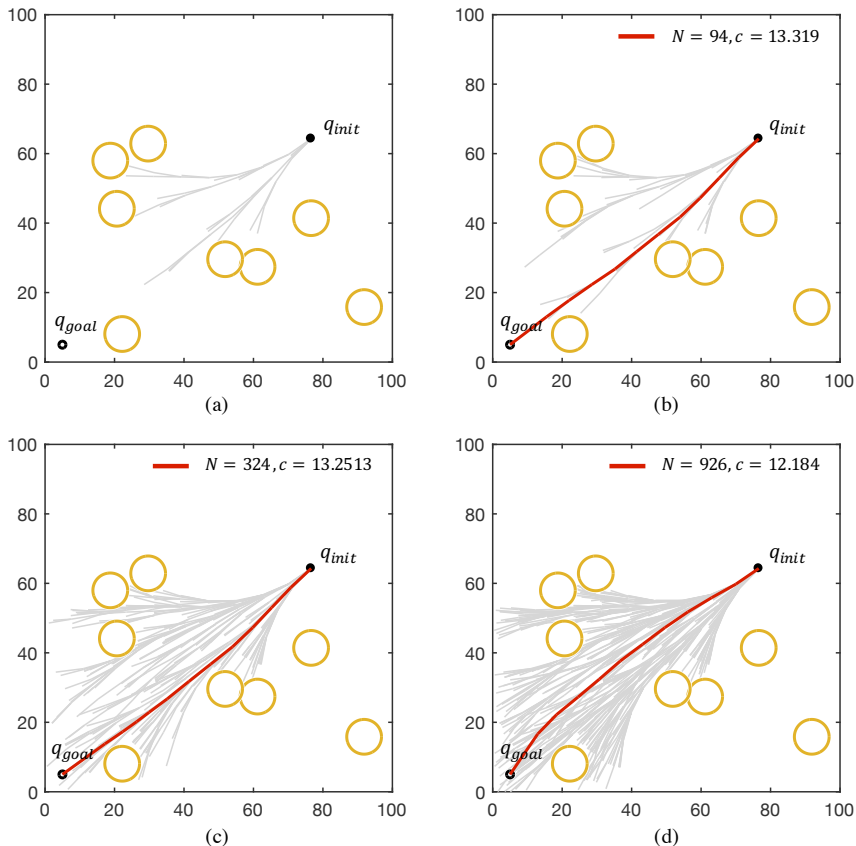
Figure 5.5 : Path planning results as a function of the number of iterations (a) $N = 50$, (b) $N = 100$, (c) $N = 500$, and (d) $N = 1000$. The best paths that reach the target from the iterative method are described with red line. The algorithm was ran for $\eta = 8$, $r_{\min} = 40$, $w_d = 0.5$, $w_\theta = 0.5$, $a_1 = 0.1$, and $a_2 = 0.9$.

to determine the feasible path in Figure 5.5 (a). As the algorithm was allowed to run for a large number of iterations, it determines the best path with a decreased cost albeit at an increased computing time.

## 5.2 Surgical Constraints

The most common targets for Parkinson's disease are subthalamic nucleus and the internal division of globus pallidus. While anterior thalamus is the main target for epilepsy, fornix is for mild Alzheimer's. To attain a successful surgical outcome, these target regions should be reached within the planned path but not penetrating critical structures in the brain. The following anatomical constraints as well as physical constraints of the flexible needle are considered in the algorithm. These constraints are used as hard constraints in the planning algorithm, which must be satisfied [2]. The optimal paths are obtained by using the cost function related to these constraints.

### 5.2.1 Anatomical Constraints

The entry point is selected in a certain region not to penetrate the midline. This confines the entry point only in the ipsilateral region to the target. For cosmetic reasons, it is preferred to have an entry point posterior to the hairline. This is incorporated in the algorithm by restraining the range of initial configurations. It is also important to avoid the sulci because there are often small blood vessels at their base in the subarachnoid space. This creates an additional constraint for possible entry points.

To avoid leakage of cerebrospinal fluid or hemorrhage, ventricles and large blood vessels should be avoided. Note that many adverse effects have been reported when the surgical trajectories cut across the brain ventricles. The function `CollisionFree` incorporated in the algorithm ensures that the path does not penetrate ventricles or blood vessels. This also includes the distance measure of the path to anatomical obstacles to minimize the risk of hemorrhage.

These anatomical constraints for the entry points can be further extended by accommodating the functional anatomy of the brain. Some highly eloquent cortical regions such as the central lobe and Brocas area should for instance be avoided [11]. The precentral gyrus which is the site of the primary motor cortex is also to be prohibited [12]. The proposed algorithm allows for any additional obstacles that can be added by neurosurgeons pre-operatively.

### 5.2.2 Physical Constraints

The flexible needle can only be steered along a continuous and smooth path. This restricts the choice of available path to be the set of linear lines or constant

curvature curves.

The needle has a minimum bend radius based on its mechanical properties and interactions with brain tissue. The final determined paths, therefore, should not include edges having a larger curvature than $\frac{1}{r_{\min}}$.

Since the stereotactic frame is considered to position the insertion point, the initial condition is restricted with an orientation perpendicular to the hemisphere frame though it is determinant of a specific type of the frame.

## 5.3 Results

### 5.3.1 Anatomical Obstacles

It is assumed that the preoperative MRI is accessible that the geometry of the brain, including the target region and obstacles to be avoided, are specified. The automatic segmentation method to extract the geometry of anatomical constraints from medical images are not discussed in this thesis.

To simulate the realistic environment in planning DBS procedure, a 3D model of the brain parts is utilized including ventricles, arteries and veins. The models of subthalamic nucleus and fornix are also included as the target region for the planning algorithm. The 3D model is voxelized with a resolution of $2 \times 2 \times 2$ mm$^3$, simulating the data set acquired from MRI. The voxels are used for collision detection in the algorithm with the radius of $2\,\mathrm{mm}$. The resolution of the voxel affects the speed of the planning algorithm because the collision detection and its computational cost are required iteratively.

### 5.3.2 Path Planning for Targeting Subthalamic Nucleus

The proposed path planning algorithm is used to determine the feasible trajectories by considering the anatomical constraints and the cost regulating its efficiency and safety. The maximum curvature allowed for the flexible needle was $0.025\,\mathrm{mm}^{-1}$. The distance $\epsilon_d$ was set to $20\,\mathrm{mm}$ implying that the obstacles from the path further than this distance are not reflected in the cost. The parameters used are $a_1 = 0.1$, $a_2 = 0.9$, $w_d = 0.9$, $w_\theta = 0.1$, $\eta = 8$. The planning result in Figure 5.6 visualizes the feasible trajectory from the predefined single entry point to the goal region located at the subthalamic nucleus, which is the target region for Parkinson's. The algorithm determined the feasible trajectory using the iterative method (red) with a lower cost than the trajectory with a constant curvature (green).
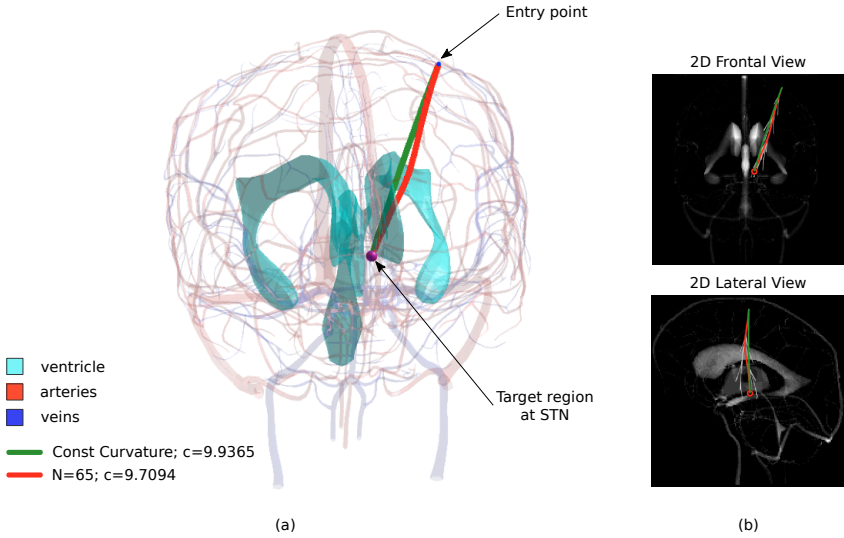
Figure 5.6 : Path planning results for targeting subthalamic nucleus from a single entry point with anatomical obstacles including ventricles, arteries and veins. (a) 3D trajectory with a constant curvature (green) and the one from iterative method (red). (b) 2D frontal and lateral views with the edges formed by the algorithm (grey).
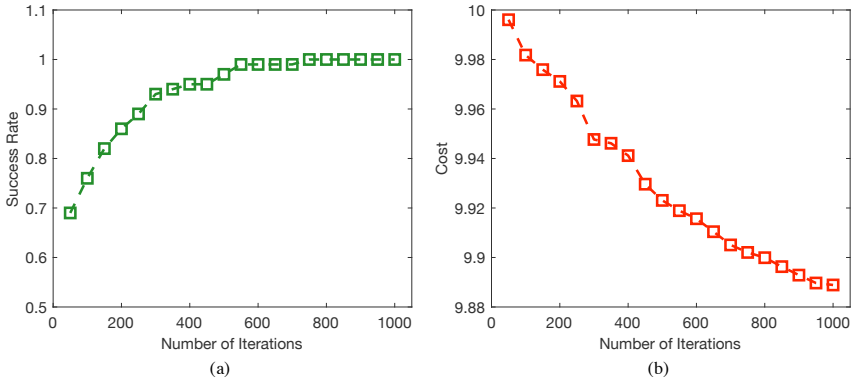


Figure 5.7 : Performance of the planning approach. (a) The cost of the best paths as a function of iterations averaged over 100 trials. (b) The success rate of algorithm as a function of iterations.

On average, the feasible path was first determined after 85 iterations. Table 5.1 summarizes the mean and standard deviation of the number of iterations and its cost until the determination of the first feasible path.

Table 5.1 : Performance of the proposed approach to the given single entry point.

| No. Trials | Average No. Iterations | Average Cost |
|:---:|:---:|:---:|
| 100 | 85.14± 134.88 | 10.0003± 0.1064 |

As the algorithm was allowed to run until $N = 1000$, it further improved the paths in the trees to lower cost as described in Fig 5.7. The algorithm had a 69% success rate with a small number of iterations $N = 50$, and it improves to 100% as $N$ becomes larger than 750.

The planning algorithm to optimize the entry point is tested in the same environment to reach the subthalamic nucleus. To avoid an insertion point near the sulci, feasible entry points are determined using the structure of the cerebrum as shown in Figure 5.8. For a given set of available insertion points, the initial configuration is decided with an exhaustive search within the area. In the planning algorithm, the blood vessels and the ventricles are incorporated as the obstacles to be avoided with a minimum distance of 2 mm. These constraints were confirmed by the minimal distance from the determined path to the obstacles for each initial configuration. The color-coded maps in Figure 5.8 show the minimal distance to vessels and ventricles which ranges from 2 mm to 8.1 mm and 5.6 mm, respectively. Only the entry points which could provide feasible paths were represented in the map. Although most of the selected entry points result in a good distance to the vessels, the minimal distance gets larger toward the center of the gyri. On the other hand, as the entry point gets closer to the midline, it becomes harder to reach the target nuclei with a simple trajectory because of the ventricles in between. The determined path has a safer trajectory against ventricles when it gets further away from midline. The total cost map demonstrated in the last column is obtained using the cost function discussed in 5.1.2, concerning the distance from obstacles together with its associated path length. Overall, the algorithm prefers the entry point toward the center of the gyri and lateral to the midline.

(a) Feasible entry point

(b) Cost

(c) Distance to vessels
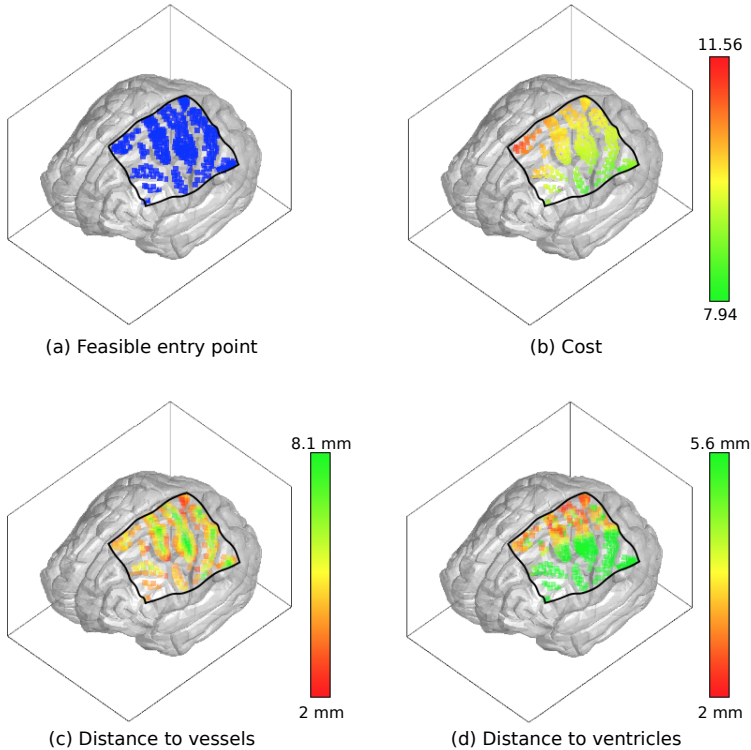
(d) Distance to ventricles

Figure 5.8 : Path planning results for optimizing entry points. (a) Feasible entry point considering the distance to sulci. (b) Total cost of the best path from the algorithm. (c,d) Color-coded maps showing the minimal distance to vessels and ventricles from the best path determined for each initial configuration.

## 5.3.3 Path Planning for Targeting the Fornix

The proposed planning approach is also tested for a different target. In the scenario of treating Alzheimer's disease, the goal is to bring the electrodes sufficiently close to the fornix, usually the descending limbs of it, but still avoiding it. Reaching the fornix is more demanding since it is surrounded by lateral ventricles. Here, the results of the proposed planning algorithm is compared to the straight path. It was possible to reach the target through 57% of the given entry points which is considerably larger than the straight path which was only available from 23%. Figure 5.9 shows this difference projected on the surface
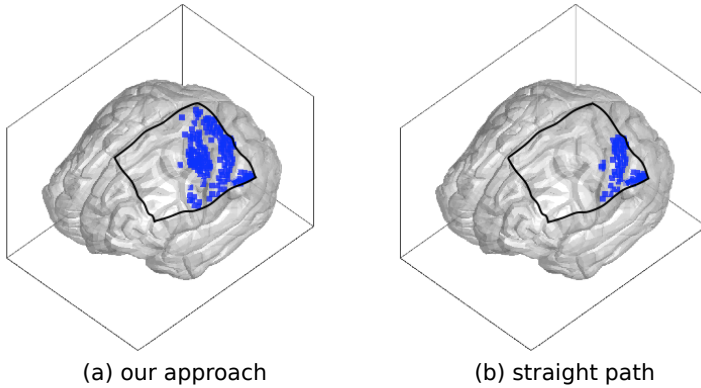
(a) our approach          (b) straight path

Figure 5.9 : Feasible entry points from (a) the proposed approach including curved paths compared to (b) the straight path. The target region is fornix.

of cerebrum. For each entry points, the minimal distance to ventricle through the determined path is analyzed. The straight path avoids ventricles within the range between $2.02\,\text{mm}$ and $2.69\,\text{mm}$, whereas the curved path proposed in the approach could perform from $2.00\,\text{mm}$ to $6.00\,\text{mm}$. Overall, the algorithm herein suggested gives more choice of entry points with a safer surgical trajectory.

Most of the straight paths started from the precentral gyrus, while the curved paths provided entry points in the superior and medial frontal gyrus. Ultimately, this rejects most of the straight paths to target the fornix and makes the proposed approach of great interest to provide safer paths to access this region.

## 5.4 Discussion

The path planning method is introduced to guide flexible needles along curved paths for DBS applications. An RRT$^*$ based planning algorithm is adopted to account for anatomical and physical constraints coming from the flexible needle. The path length and distance to obstacles are both considered in a dedicated cost function used in the exploration of the tree, and in the selection of the best path among a set of feasible paths and entry points. The method is evaluated in simulation using realistic anatomical obstacles from a human brain CAD model and shows the ability to find multiple curved paths from a set of predetermined feasible entry points to the target region.

As compared to current DBS techniques, steering needles along curved paths

using the proposed path planner presents several advantages. First, much more entry points can be considered, as well as safer paths for a given entry point (i.e. further from the obstacles). To this extent, the method makes it possible to reach the target nuclei with low-risk path by not interfering with ventricle or caudate nuclei, which could otherwise cause some decline in verbal fluency and memory performance [13], [14]. Future work could also include adding different weights on the obstacles depending on their criticality regarding safety. As the path planning is performed automatically using segmented anatomical features, one can also consider to provide better inputs to the surgeon to evaluate a potential path. This includes representing the closeness to obstacles along the path, or propose alternative paths for the entry point under consideration.

# References

[1]   E. J. Brunenberg, A. Vilanova, V. Visser-Vandewalle, Y. Temel, L. Ackermans, B. Platel, and B. M. ter Haar Romeny, "Automatic trajectory planning for deep brain stimulation: A feasibility study," in *Med Image Comput Comput Assist Interv*, 2007, pp. 584–592.

[2]   C. Essert, C. Haegelen, F. Lalys, A. Abadie, and P. Jannin, "Automatic computation of electrode trajectories for deep brain stimulation: A hybrid symbolic and numerical approach," *Int J Comput Assist Radiol Surg*, vol. 7, no. 4, pp. 517–532, 2012.

[3]   S. Bériault, F. Al Subaie, D. L. Collins, A. F. Sadikot, and G. B. Pike, "A multimodal approach to computer-assisted deep brain stimulation trajectory planning," *Int J Comput Assist Radiol Surg*, vol. 7, no. 5, pp. 687–704, 2012.

[4]   Y. Liu, P. E. Konrad, J. S. Neimat, S. B. Tatter, H. Yu, R. D. Datteri, B. A. Landman, J. H. Noble, S. Pallavaram, B. M. Dawant, *et al.*, "Multisurgeon, multisite validation of a trajectory planning algorithm for deep brain stimulation procedures," *IEEE Trans Biomed Eng*, vol. 61, no. 9, pp. 2479–2487, 2014.

[5]   R. Alterovitz, A. Lim, K. Goldberg, G. S. Chirikjian, and A. M. Okamura, "Steering flexible needles under markov motion uncertainty," in *IEEE/RSJ Int Conf Intelligent Robots and Systems*, IEEE, 2005, pp. 1570–1575.

[6]   S. Patil and R. Alterovitz, "Interactive motion planning for steerable needles in 3d environments with obstacles," in *Proc IEEE RAS EMBS Int Conf Biomed Robot Biomechatron*, 2010, pp. 893–899.

[7]   S. Patil, J. Burgner, R. J. Webster, and R. Alterovitz, "Needle steering in 3-D via rapid replanning," *IEEE Trans Rob*, vol. 30, no. 4, pp. 853–864, 2014.

[8]   S. Bano, S. Y. Ko, and F. R. y Baena, "Smooth path planning for a biologically-inspired neurosurgical probe," in *Conf Proc IEEE Eng Med Biol Soc*, IEEE, 2012, pp. 920–923.

[9]   S. Karaman and E. Frazzoli, "Sampling-based algorithms for optimal motion planning," *Int J Rob Res*, vol. 30, no. 7, pp. 846–894, 2011.

[10]   S. M. LaValle and J. J. Kuffner Jr, "Randomized kinodynamic planning," *Int J Rob Res*, vol. 20, no. 5, pp. 378–400, 2001.

[11]   T. Frigeri, E. Paglioli, E. de Oliveira, and A. L. Rhoton Jr, "Microsurgical anatomy of the central lobe," *J Neurosurg*, vol. 122, no. 3, pp. 483–498, 2015.

[12]   E. F. Chang, K. P. Raygor, and M. S. Berger, "Contemporary model of language organization: An overview for neurosurgeons," *J Neurosurg*, vol. 122, no. 2, pp. 250–261, 2015.

[13]   M. K. York, E. A. Wilde, R. Simpson, and J. Jankovic, "Relationship between neuropsychological outcome and DBS surgical trajectory and electrode location," *J Neurol Sci*, vol. 287, no. 1, pp. 159–171, 2009.

[14]  K. Witt, O. Granert, C. Daniels, J. Volkmann, D. Falk, T. van Eimeren, and G. Deuschl, "Relation of lead trajectory and electrode position to neuropsychological outcomes of subthalamic neurostimulation in parkinson's disease: Results from a randomized trial," *Brain*, vol. 136, no. 7, pp. 2109–2119, 2013.

# Chapter 6

# Conclusion

In this thesis, a new robotic-based approach for navigating flexible needles was investigated. Specifically, this work aimed to ease neurosurgical procedures through the development of minimally invasive surgical tools, which enables accessing lesions in the brain in a precise and safe manner. To achieve precise navigation of surgical instruments in biological tissues, fluoroscopy, and magnetic manipulation are used for imaging and actuating devices, respectively. To ensure the safety of this approach, surgical constraints are introduced as variables in the sampling-based planning algorithm.

Chapter 3 investigates the feasibility of using a C-Arm fluoroscope for the 3D localization of small surgical devices in the body. A single-axis fluoroscope provides high resolution in the image plane. However, the resolution in the depth direction is poor and unsuitable for surgical applications. By changing the configuration of the fluoroscopic device relative to the targeted tools, the fluoroscopic images are taken at different views. Consequently, the direction of the most uncertain axis is changed, as a result of 3D position estimation. Then, a Kalman filter is used to assess localization uncertainties associated with a single fluoroscopic image. In parallel, the same filter reduces measurement errors by combining sequential position estimates. To validate the effectiveness of this approach, two minimally invasive surgical instruments of different sizes and targeted applications were employed. When using the suggested strategy with ablation catheters and neurostimulation electrodes, the uncertainties of the position estimates decreased by 62 and 32 percent, respectively.

Chapter 4 addresses the feasibility of navigating a flexible needle with fluoro-

scopic imaging and magnetic steering in soft tissue environments. The kinematic model is derived based on a nonholonomic bicycle model, and a closed-loop control strategy is implemented using a chained-form transformation. To validate the control strategy, the experimental work was performed using *in vitro* brain phantom and *ex vivo* pig brain. In agarose brain phantom, the magnetic flexible needle could reach straight paths and curved paths with the accuracy of $0.91 \pm 0.38$ mm and $0.59 \pm 0.53$ mm, respectively. The proposed control strategy enables to converge the needle path to the desired one with a small discrepancy at its initial position. In *ex vivo* pig brain, the experimental results demonstrated the accuracy of $0.37 \pm 0.29$ mm and $0.27 \pm 0.25$ mm, for the curved and straight paths.

Chapter 5 pushes the idea of using flexible needles in a neurosurgical procedure, such as deep brain stimulation (DBS). As such, a computer-aided surgical planning approach is developed, resulting in a safety enhancement, and increasing the choices of the feasible paths, compared to the current strategies using straight needles. An RRT$^*$ sampling-based approach is adapted to incorporate the physical constraints derived from the flexible needle and the anatomical constraints from the brain. In two different scenarios, targeting the subthalamic nucleus and the fornix, multiple feasible paths are determined. Especially when targeting the fornix, the result demonstrates 34 percent more feasible paths compared to when a straight needle is used.

The strategy developed in this work represents a comprehensive approach for tracking, navigating, and planning paths for the actuation of minimally invasive surgical tools. The use of this approach in neurosurgical procedures could considerably enhance its safety and success rate while minimizing potential side effects. The capability of targeting specific locations in the brain region demonstrated in this work could be extended to other brain-related applications, such as needle biopsy for brain tumors, and seed implantation for radiotherapy.

# Appendix A

# Holographic Tracking for Microrobots

In this chapter, digital in-line holography (DIH) techniques are used to track the 3D position of magnetic microrobot maneuvered in real-time by means of an electromagnetic manipulation system. As this method does not require magnification, microrobots can be tracked in significantly larger working volumes than conventional optical methods. The tracking performance is demonstrated by visually servoing a micro-sized magnetic object submerged in silicone oil.

## A.1 Motivation

Microrobots have been proposed as dexterous machinery for lab-on-a-chip devices in applications ranging from single cell mechanical characterization, to mobile localized mixing and assembly, targeted drug delivery, and microassembly [6]–[9]. While many aspects of microrobotics, such as locomotion, fabrication, and functionalization, have been thoroughly addressed, visual servoing of mobile microrobots has been only currently demonstrated in 3D [10], [11].

The stereo vision system is mostly used to extract the 3D position of a microrobot during manipulation. Two optical microscopes from the top and the side provide an intuitive method to reconstruct the 3D position of an object. Unfortunately, the high magnification systems required to image a microrobot, reduce the depth-of-field [12]. Applying to stereo vision, this results in a very limited observable volume. To avoid this problem, depth-from-focus can be used [13], [14]. This method estimates the depth of the object based on the extent that it is out of focus and can adjust the focusing depth to move with the microrobot as it moves in 3D space. However, this limits object tracking only
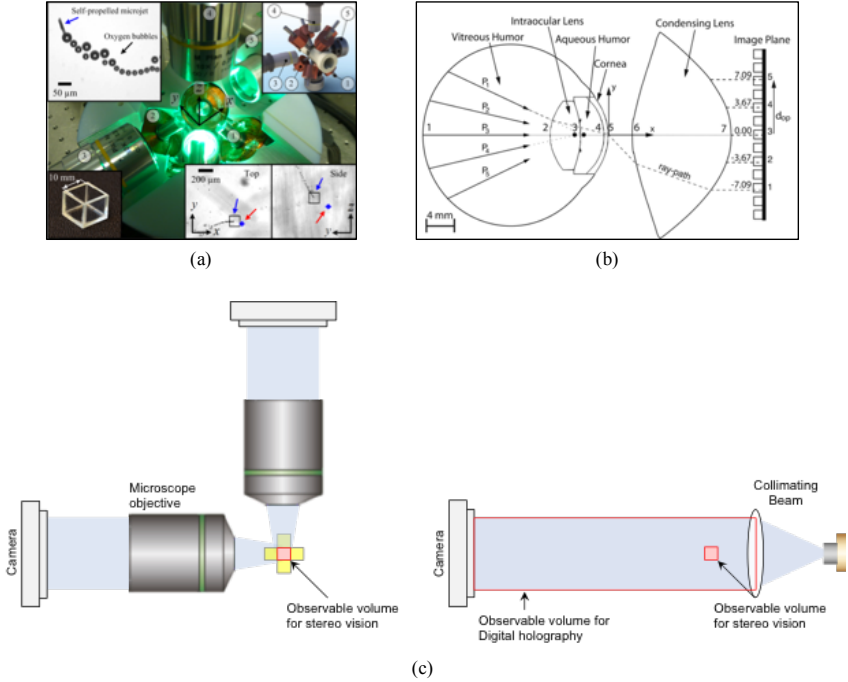
Figure A.1 : Vision system for microrobots. (a) Stereo vision system with top and side views [1] (b) Localization of microdevices using the optical models of human eye [2]. (c) A comparison of observable volume for stereo vision system and digital holography.

at a single depth as in Figure A.1. Recently, medical imaging modalities such as ultrasound and positron emission tomography has been suggested to track microrobots [1], [15], though not yet fully implemented with 3D manipulation at the microscale.

Digital holography has been proposed to overcome these limitations. Digital in-line holography reconstructs a 3D volume based on the diffraction pattern created when an electromagnetic wave interacts with an object [16], [17]. This diffraction pattern can be numerically analyzed to yield image slices at any desired imaging depth, which enables volumetric image reconstruction similar to magnetic resonance imaging. Since holographic imaging was first proposed to eliminate the lenses and the aberration introduced in electron beam imaging systems [18], it has been adapted for optical microscopy [19] and explored many
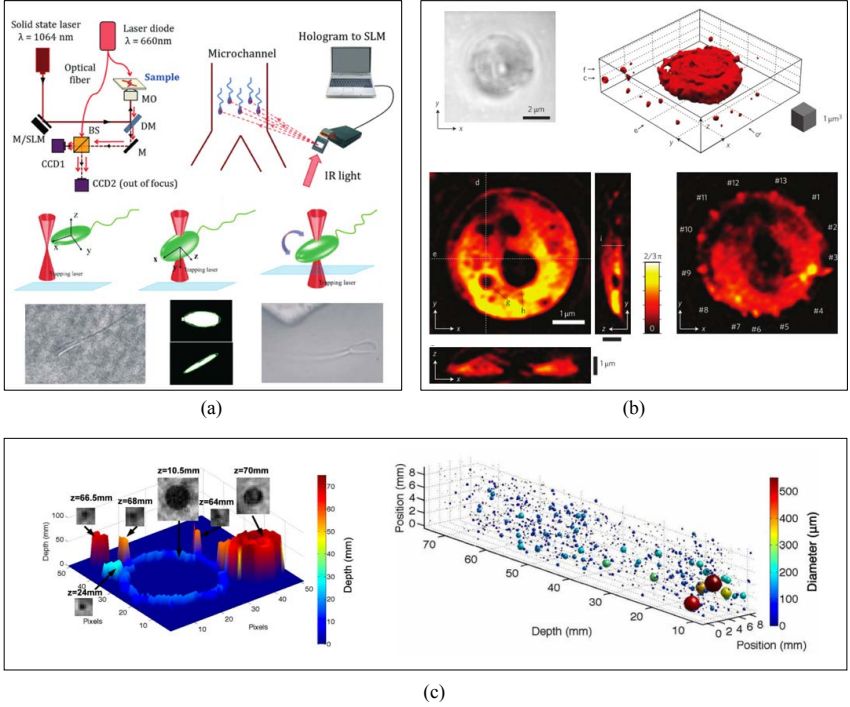
102

(a)

(b)

(c)

Figure A.2 : Applications of digital holography in imaging of living cells or micro particles. (A) 3D imaging and estimating the biovolume of sperm cells combining optical tweezers technique with digital holography [3]. (b) Super-resolved phase imaging of nanoscopic porous cell featuring sudden refractive index changes [4]. (c) Tracking 3D position and measuring the size of fast-moving bubbles in air-water mixture flows using a digital inline holographic imaging system [5].

applications ranging from high-resolution volumetric imaging of living cells [3], [4], [20] to 3D tracking of motile biological cells and particles in colloids [5], [21]–[24] as in Figure A.2. Nevertheless, real-time particle extraction of 3D object localization based on holography has yet to be reported.

## A.2 Digital Holography Background

A holographic imaging setup consists of a coherent collimated reference source $R$ and a camera sensor chip (Figure A.3). When the reference wave $R$ interacts with an object in the workspace, a diffraction wave $O$ is generated. The interference
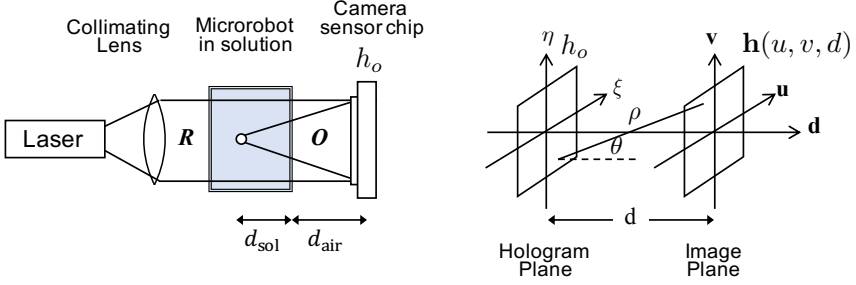
Figure A.3 : Schematics of a digital in-line holography setup. $R$, reference wave; $O$, object wave; $d$, propagation distance; $d_{\text{sol}}$ and $d_{\text{air}}$, geometric distance of wave travelling through solution and air, respectively. $h_0$ is a recorded hologram function in a hologram plane with a camera sensor chip and $\mathbf{h}(u, v, d)$ is a complex amplitude field in the image plane, which is the reconstructed image of the recorded hologram at a desired propagation distance $d$. $\xi$, $\eta$, $u$, and $v$ are the spatial coordinates in the hologram plane and the image plane.

pattern recorded by the camera sensor chip $h_0$, encodes all of the spatial information of the object in the 3D workspace. Holographic reconstruction is performed by back-propagating the hologram $h_0$ with the Fresnel diffraction pattern. The resulting object wave provides a reconstruction of the object's diffraction pattern at any depth.

The numerical hologram reconstruction is based on the Fresnel-Kirchhoff integral [25], which describes the complex amplitude image $\mathbf{h}(u, v, d)$ as

$$\mathbf{h}(u, v, d) = \frac{i}{\lambda} \iint h_0 R \frac{\exp\left(-i\frac{2\pi}{\lambda}\rho\right)}{\rho} \times \left(\frac{1}{2} + \frac{1}{2}\cos\theta\right) \mathrm{d}\xi \mathrm{d}\eta \qquad (A.1)$$

with

$$\rho = \sqrt{d^2 + (\xi - u)^2 + (\eta - v)^2} \qquad (A.2)$$

where $\lambda$ is the laser wavelength, $\rho$ is the distance between a point in the hologram plane and a point in the reconstructing image plane [25], and $\theta$ is the angle between two points. For large values of $d$ the small angle approximation ($\cos\theta \approx 1$) can be applied and the reference wave $R$ can be modelled as constant and real valued [26]. The convolution described by (A.1) is more efficiently implemented in the Fourier domain. Thus, the reconstruction process is given by a Fourier

transform, an element-wise multiplication, and an inverse Fourier transform.

$$\mathbf{h}(u, v, d) = \mathcal{F}^{-1}\{\mathcal{F}\{h_0\} \times G_d\}, \tag{A.3}$$

Here, $\mathcal{F}$ is the Fourier transform operator and $G_d$ is the distance dependent kernel as

$$G_d = \exp\left(i\frac{2\pi}{\lambda}\right)\exp\left(-i\pi\lambda d(u_s^2 + v_s^2)\right) \tag{A.4}$$

where $u_s$ and $v_s$ represent the Fourier spectral coordinates.

The numerical aperture (N.A.) of the system is

$$N.A. = \frac{n}{\sqrt{1 + 4(\frac{d}{w})^2}} \tag{A.5}$$

where $w$ is the sensor size and $n$ is the refractive index of the medium. This numerical aperture affects the axial resolution of reconstruction as

$$\sigma_{\text{axial}} = \frac{\lambda}{(N.A)^2} = \frac{\lambda}{n^2}(1 + 4(\frac{d}{w})^2), \tag{A.6}$$

which describes the ability to resolve two different objects at different depths [17].

The complex amplitude image $\mathbf{h}$ can be reconstructed at any distance $d$. However, this distance is the effective displacement in vacuum. Since the wave propagates in optically dense mediums, i.e., when the refractive index of medium is not unity, the propagation distance, $d$, is given by

$$d = \Sigma\frac{d_i}{n_i}, \tag{A.7}$$

where $d_i$ and $n_i$ are the geometric distances and the refractive indexes of the $i$-th medium, respectively.

## A.3 Tracking Algorithm

The numerical reconstruction given by (A.3) defines a set of images that can be searched to determine the 3D position of the microrobot. To accomplish this search, the 3D tracking algorithm is split into three steps, which are presented in Figure A.4. First, the object is located in a raw image and a subimage is generated at the last known depth. Next, a search is conducted to find the current depth of the object. Finally, the object's in-plane position is refined based on the image reconstructed at the current depth.
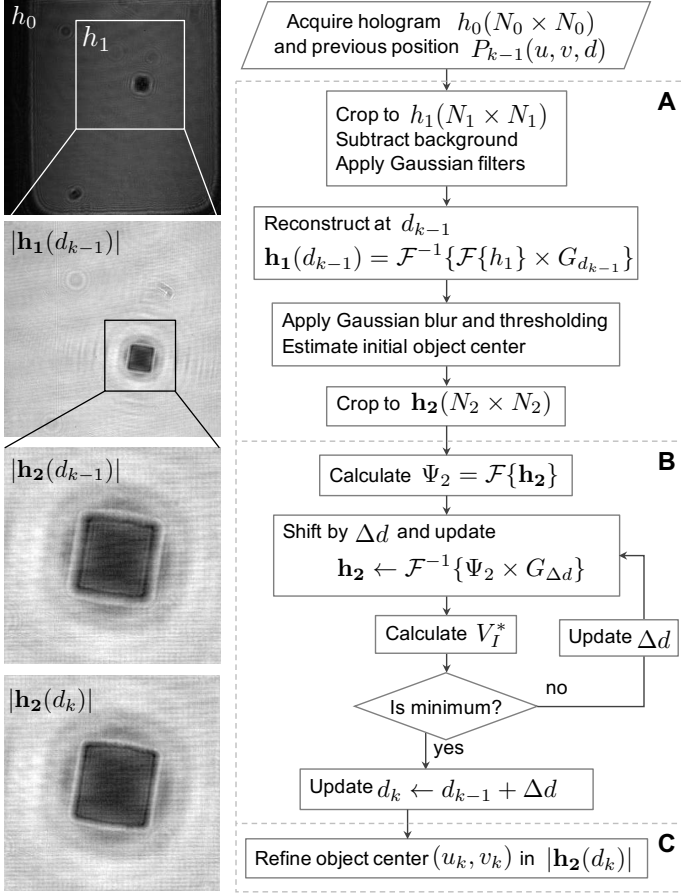
Figure A.4 : Flowchart for the holographic tracking algorithm. **A**. Preprocessing and initial estimation select a sub-image to use for a numerical reconstruction based on the previous position. **B**. Axial position is determined by successively checking the variance of complex image $V_I^*$ using Brent's minimization method. **C**. Lateral position is determined by segmenting the object in the final reconstructed image $|\mathbf{h_2}(d_k)|$. $N_0 = 2048$, $N_1 = 1024$, $N_2 = 256$ are used for the experiment.

## A.3.1  Image Preprocessing

An element-wise multiplication and an inverse Fourier transform in (A.3) are iteratively performed until the optimum is found. This algorithm has a compu-
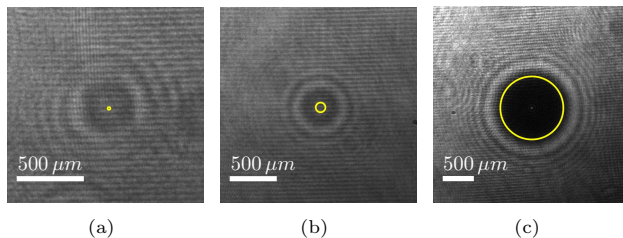
Figure A.5 : Holograms of different size of beads in deionized water with diameters of (a) $20\,\mu$m, (b) $100\,\mu$m and (c) $1000\,\mu$m. The actual bead size is marked with circles. These holograms are acquired with a CMOS sensor chip with a pixel size of $5.5\,\mu$m$\times 5.5\,\mu$m without magnification. Scalebars: $500\,\mu$m.

tational complexity of $O(N^2 \log N)$ where the image is $N \times N$ pixels. Thus, the first step is to crop the image to a smaller region of interest that contains all of the pertinent information. This is performed in two steps: the object needs to be identified in the image and the image needs to be reconstructed at a depth close to the object's expected depth. The first step determines the center of the subimage to be used in the search. The second step contracts the holographic diffraction pattern so that a smaller image can be used in the search. Localization of the object in the image can be performed either before the reconstruction using the diffraction pattern directly or after by examining the shape of the object's shadow. Small objects are difficult to localize from in-focus images because they are only a few pixels in extent. However, as shown in Figure A.5, they cast a prominent holographic bulls-eye. Thus, these objects can be localized more easily in the raw holographic image. Although the difference is much less significant than for small objects, large objects can be difficult to segment in the raw holographic image because the diffraction pattern distorts the object's shape and the ring pattern is less pronounced. A relatively large object was used in the experiment, and it has been localized in the reconstructed image. Once the object's approximate in-plane position is known and the image is reconstructed at the last known depth $d_{k-1}$, the background reference image is subtracted to remove zero-order disturbances [27], and a Gaussian filter is applied to reduce noise. The resulting complex amplitude image $\mathbf{h_1}(d_{k-1})$ is obtained and cropped to $\mathbf{h_2}(N_2 \times N_2)$, which is centered at the initial in-plane position estimate. As $\mathbf{h_2}$ is used for the subsequent search, the size of $N_2$ needs to be chosen considering computational efficiency and the accuracy of the result. For efficiency, $N_2$

should be a power of 2 and as small as possible. For accuracy, $N_2$ should be large enough to capture the diffraction pattern and to preserve the axial resolution of the subimage, i.e.,

$$N_2 \geq \frac{2\Delta d}{p} \sqrt{\frac{\lambda}{n^2 \sigma_{\text{axial}} - \lambda}}, \tag{A.8}$$

where $p$ is a camera pixel size and $\Delta d$ is the maximum depth difference expected between the initial reconstruction plane and the actual depth.

### A.3.2 Axial Position Estimation

To estimate the axial position of the microrobot, particle extraction using a complex amplitude is used [28]. This method is based on the observation that the variance of the imaginary part of reconstructed hologram image **h** has a minimum near the in-focus plane and is robust to noise in the numerical reconstruction.

The variance of an imaginary part of **h** gives a minimum value in the in-focus plane when the microrobot is not in the proximity of the container side walls. However, when the microrobot is close to the container side walls the hologram is distorted and $V_I$ has a minimum outside of the workspace in Figure A.6. In this case, a slope discontinuity is apparent near the in-focus plane in Figure A.6. To generalize these two cases, a shifted variance $V_I^*$, is defined by subtracting the effective variance slope across the container

$$V_I^* = V_I(\Delta d) - \frac{(V_I(d_M) - V_I(d_m))}{(d_M - d_m)} \Delta d \tag{A.9}$$

where $d_m$ and $d_M$ are the distance of the front and back of the container. The minimum of the shifted variance $V_I^*$ is slightly different from the minimum of $V_I$ in case 1 or the knee point of $V_I$ in case 2. However, this difference is negligible compared to the size of the microrobot and the uncertainty in the measurement.

Although the minimum can be obtained with an exhaustive search, this is not appropriate for real-time tracking algorithms because of the computational load of calculating $V_I^*$. Instead, Brent's search method is used to minimize the number of iterations [29]. It combines a bisection method with quadratic interpolation to perform a line search with a minimal number of function evaluations.

The current axial position of the microrobot is updated to $d_k = d_{k-1} + \Delta d$, where $\Delta d$ is the solution of the minimization problem. The depth $d_k$ is the propagation distance in a vacuum, thus (A.7) is used to convert it to the
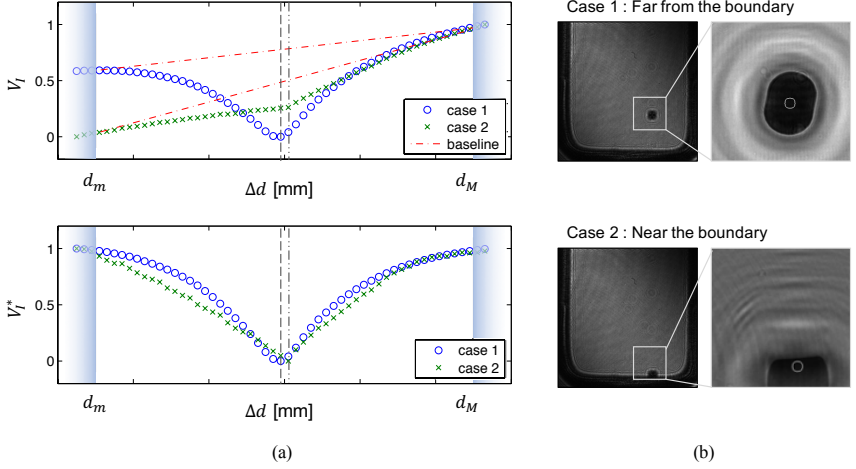
Figure A.6 : Autofocusing measure along a depth direction. (a) Variance, $V_I$, and shifted variance, $V_I^*$, along a depth direction. The container size sets the physical constraints, $d_m$ and $d_M$ on axial position estimation. $V_I$ shows the dipping characteristics near the in-focus plane (case 1) except when the microrobot is near to the wall of container (case 2) (top). To find the knee point in both case 1 and 2, $V_I$ is shifted with base line (bottom). (The graph is normalized to show the two cases at the same scale). (b) Reconstructed in-focus image when the object is far from the boundary (top) and near the boundary (bottom).

geometric axial position of the microrobot as

$$d_k^G = d_k n_{\text{sol}} + \Sigma d_i \big(1 - \frac{n_{\text{sol}}}{n_i}\big) \qquad (A.10)$$

where $n_{\text{sol}}$ is the refractive index of solution, and $n_i$ and $d_i$ are the refractive index and geometrical distance of waves travelling through the $i$-th medium, respectively (see Figure A.3).

### A.3.3 Lateral Position Estimation

Now that the depth $d_k$ of the microrobot is known, the lateral position estimate $(u_k, \ v_k)$ can be refined by segmenting the microrobot from the in-focus reconstructed amplitude image $|\mathbf{h}(d_k)|$. This is achieved by applying a Gaussian filter and using adaptive thresholding to segment the object. Among the observed contours in the binary image, the microrobot is segmented by finding the con-
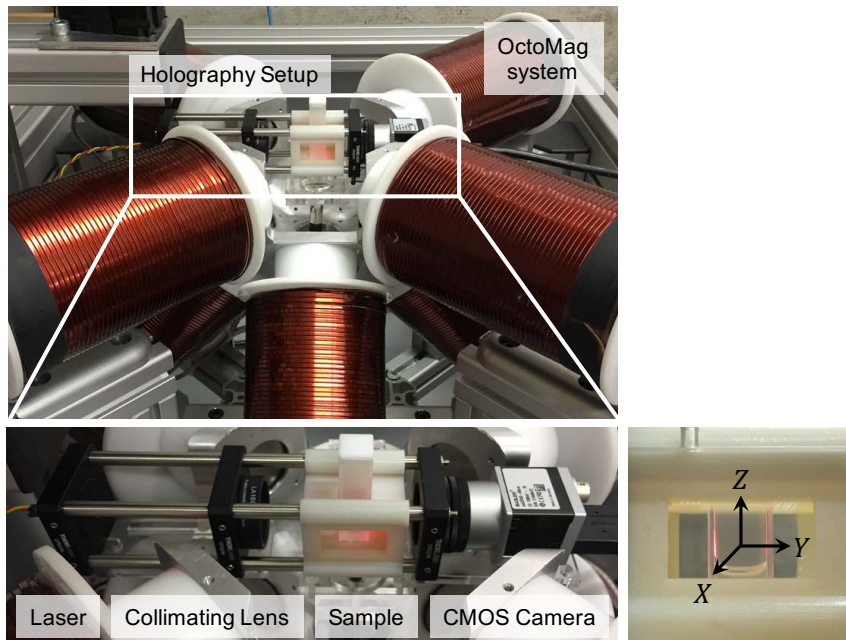
Figure A.7 : Digital in-line holography setup integrated with the OctoMag electromagnetic manipulation system. The origin of the coordinate system is at the center of the manipulation system's workspace.

tour that encloses an area that matches the expected object size. The lateral position is then updated with the segmented object's centroid.

## A.4  Experiments

### A.4.1  Experimental Setup

The Octomag electromagnetic manipulation system is used for 3D wireless magnetic control of the microrobot (see Figure A.7) [30]. The system consists of eight electromagnetic coils in a hemispherical arrangement and allows for magnetic fields up to 40 mT and magnetic field gradients up to 1 T/m. The magnetic workspace is a $20 \times 20 \times 20\,\text{mm}^3$ cube. For holographic imaging, the illumination is produced by a laser diode with a wavelength of 635 nm along with a BP635 red light bandpass filter. A digital camera with $2048 \times 2048$ pixels, each pixel

with an edge length of $5.5\,\mu$m, is used to record the holograms. It can generate at 90 fps.

The microobject is a Neodymium-Iron-Boron (NdFeB) cylindrical magnet with a diameter of $500\,\mu$m and a height of $500\,\mu$m, which is manipulated in silicone oil. The refractive index of silicone oil (i.e., $n_{sol}$ in (A.10)), is reported to be 1.502 at $20\,°$C, taken at the Sodium D Line (589.29 nm wavelength). This number is calibrated experimentally.

The system is controlled by a workstation PC (Intel Core i7-5930K CPU at 3.50GHz, 32 GB RAM) running a custom magnetic control program written in C++. The Fourier transform-based reconstruction and the variance calculation is implemented on a GPU using compute unified device architecture for parallel computations [31]. Under the current configurations of the system, the tracking algorithm can process images at 40 Hz. Each step in Section A.3 respectively takes 7.0 ms, 16.0 ms, and 1.3 ms on average. We use $N_0 = 2048$, $N_1 = 1024$, $N_2 = 256$ for the experiment. To provide a buffer, the image acquisition and control loop is limited to 20 Hz in the demonstrations.

### A.4.2 System Calibration

The refractive index of silicone oil is experimentally determined. A motorized stage with a resolution of 1 nm controls the 3D position of the calibration probe while the camera system remains stationary. The same NdFeB cylindrical magnet used for the control experiments is attached to a $22\,\mu$m diameter tungsten wire. Although the wire is visible in the reconstructed image, its effect on the calibration is negligible since it is at the same depth as the bead. The calibration probe is moved in the axial direction in steps of $200\,\mu$m in air and silicone oil. Figure A.8 shows the relation between the actual and focused depth, obtained from the tracking algorithm. The slope of this line indicates the effective refractive index of the medium. Using least squares, the refractive indices are measured to be 1.006 and 1.633 and the standard deviations of the residuals are $62.47\,\mu$m and $61.93\,\mu$m for air and silicone oil, respectively.

The accuracy of the 3D position estimateion is investigated by moving the probe in 3D space following the 4 mm squares at depth of -2, 0, and 2 mm. By using least squares, the optimal rotation and translation is found to eliminate the effect of misalignment between the camera and the stage. The standard deviations of residuals are 0.018 mm, 0.062 mm, and 0.014 mm in air and 0.023 mm, 0.169 mm, and 0.014 mm in silicone oil as shown in Figure A.9, for $x$-, $y$-, and $z$-
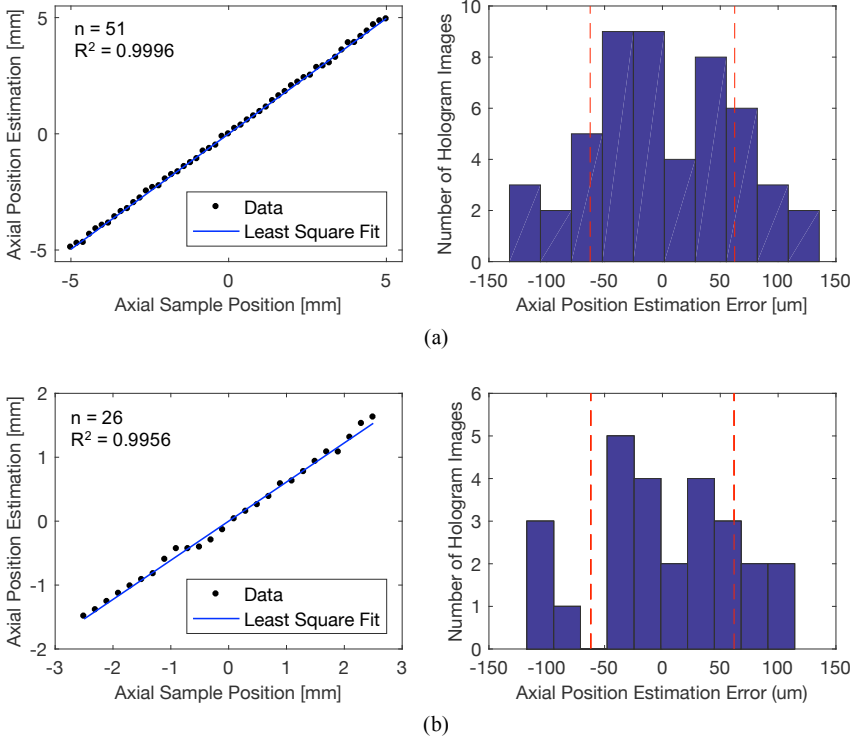
(a)



(b)

Figure A.8 : Calibration for the refractive index of (a) **air** and (b) **silicone oil**. The refractive indices of air and silicone oil are estimated as 1.006 and 1.633.

axes, respectively. The in-plane estimation shows smaller tracking errors than in the depth direction. In the image plane ($x$- and $z$-axes), the tracking algorithm shows similar accuracy in air and silicone oil about three camera pixels. In the depth direction ($y$-axis), it indicates larger errors in silicone oil than in air because the parasitic interferences are more pronounced, and the trajectory was in the range of this effect. However, the result is comparable to the axial resolution of the system calculated as $0.181\,\text{mm}$ within the workspace using (A.6).

### A.4.3 3D Closed-loop Position Control

A PD controller is used to minimize the position error between the estimation and the target point. The target is defined to be $0.3\,\text{mm}$ ahead of the projection
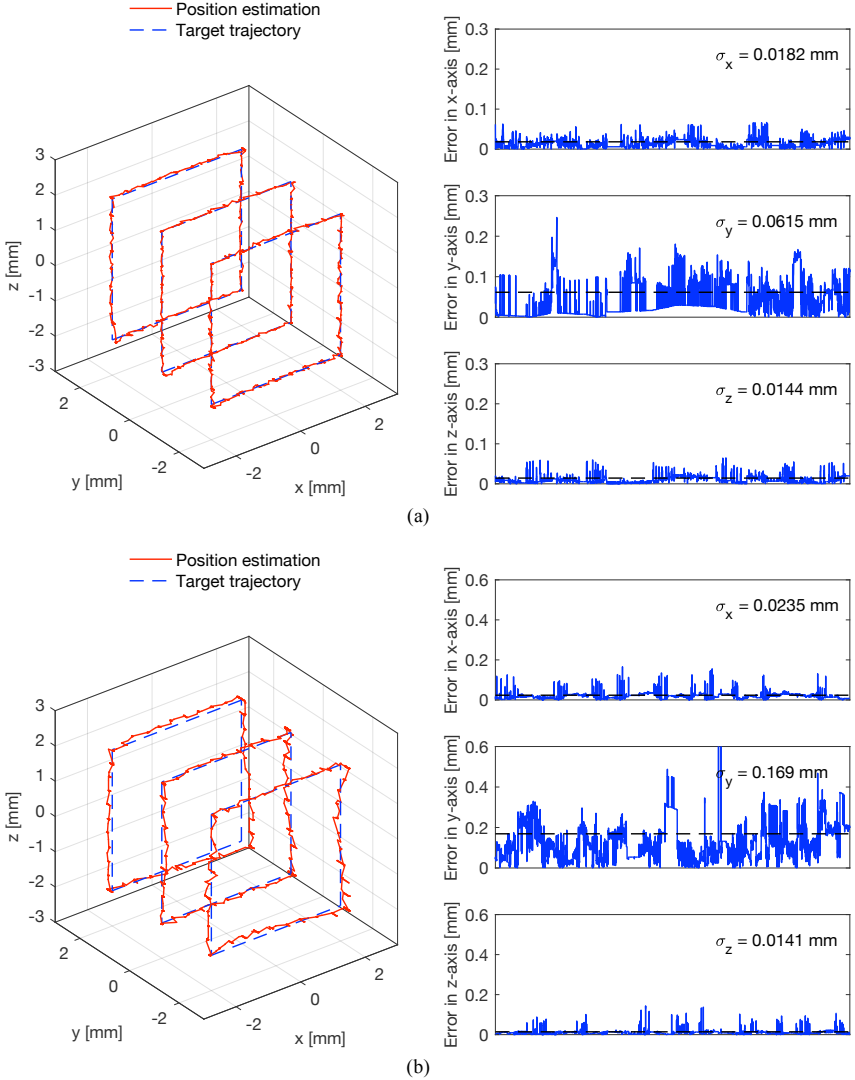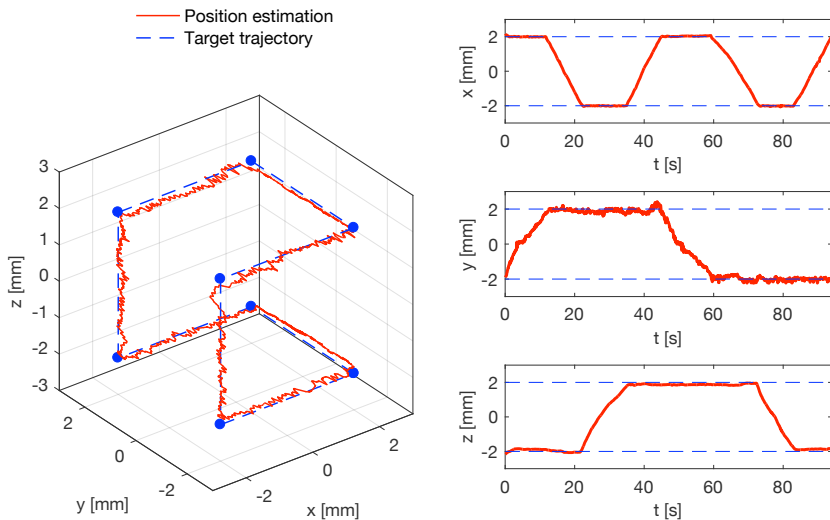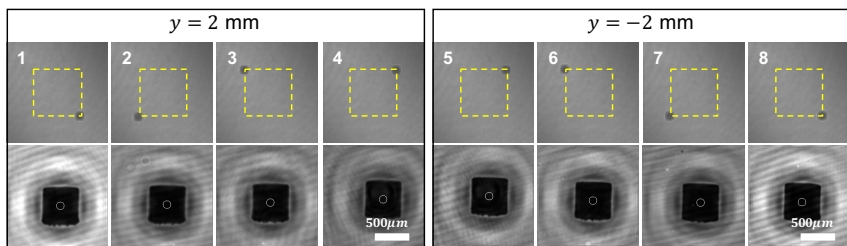
Figure A.9 : Accuracy of 3D position estimates when the object submerged in (a) **air** and (b) **silicone oil**. A reference trajectory is 4 mm squares in $y = (-2, 0, 2)$ mm.

of the current position on the target trajectory, which is a 4 mm cube centered at the workspace. The position estimate is filtered using a discrete forth-order

(a)



(b)

Figure A.10 : Closed-loop position control results using holographic tracking. (a) The 3D trajectory and tracking positions used for the controller are presented for one-cycle of trajectory. The trajectory completion time is 89 s per cycle on average. (b) Hologram image $h_0$ used in the closed-loop position control and its focused image $|\mathbf{h_2}|$ at the trajectory vertices. The yellow line shows the target trajectory in $y = 2$ mm and $y = -2$ mm.

low-pass butterworth filter with a $0.33\pi$ rad/sample cutoff frequency. In the experiment, the microrobot is aligned with the $z$-axis.

The resultant position estimates are reported in 3D for a single trajectory in Figure A.10. The mean absolute errors are $23\mu$m, $93\mu$m, and $123\mu$m and the corresponding standard deviations are $30\mu$m, $70\mu$m, and $40\mu$m for $x$-, $y$-, and

$z$-axes. The position error along $x$-axis is about several camera pixels, agreeing with the calibration result. Along $z$-axis, although the large mean absolute error is attributed to the discrepancy in gravity compensation of the microrobot, its standard deviation again corresponds with the calibration result. As expected, the resultant tracking in depth direction is less precise.

## A.5 Discussion and Conclusion

This chapter demonstrates real-time 3D position tracking of microrobots using digital holography in a microrobot control application. The advantages of holography over conventional optical microscopy for real-time tracking include the compactness of the imaging system, the ability to image the scene without requiring manual or automated mechanical focusing, and the ability to estimate an object's out-of-plane position along with its in-plane position from a single image. An additional advantage of holography for imaging microscale systems comes from object segmentation. Traditionally, small objects are difficult to segment from large backgrounds because they are difficult to distinguish from noise. However, in a holographic image, small objects affect a much larger region of the image than their physical extent because the technique considers diffraction patterns rather than reflections or shadows.

Although the cylindrical magnet is presented as a microdevice in this work, the proposed tracking method can be extended to other shapes of microdevices or be used with non-magnetic control systems. The method could also be adapted to track 3D position as well as 3D orientation of a single or multiple agents albeit at an increased computational cost.

# References

[1] I. S. Khalil, H. C. Dijkslag, L. Abelmann, and S. Misra, "Magnetosperm: A microrobot that navigates using weak magnetic fields," *Appl Phys Lett*, vol. 104, no. 22, p. 223 701, 2014.

[2] C. Bergeles, B. E. Kratochvil, and B. J. Nelson, "Visually servoing magnetic intraocular microdevices," *IEEE Trans Rob*, vol. 28, no. 4, pp. 798–809, 2012.

[3] F. Merola, L. Miccio, P. Memmolo, G. Di Caprio, A. Galli, R. Puglisi, D. Balduzzi, G. Coppola, P. Netti, and P. Ferraro, "Digital holography as a method for 3D imaging and estimating the biovolume of motile cells," *Lab Chip*, vol. 13, no. 23, pp. 4512–4516, 2013.

[4] Y. Cotte, F. Toy, P. Jourdain, N. Pavillon, D. Boss, P. Magistretti, P. Marquet, and C. Depeursinge, "Marker-free phase nanoscopy," *Nat Photonics*, vol. 7, no. 2, p. 113, 2013.

[5] L. Tian, N. Loomis, J. a. Domínguez-Caballero, and G. Barbastathis, "Quantitative measurement of size and three-dimensional position of fast-moving bubbles in air-water mixture flows using digital holography.," *Appl Opt*, vol. 49, no. 9, pp. 1549–1554, Mar. 2010.

[6] B. J. Nelson, I. K. Kaliakatsos, and J. J. Abbott, "Microrobots for minimally invasive medicine," *Annu Rev Biomed Eng*, vol. 12, pp. 55–85, 2010.

[7] E. Diller, Z. Ye, J. Giltinan, and M. Sitti, "Addressing of micro-robot teams and non-contact micro-manipulation," in *Small-Scale Robotics. From Nano-to-Millimeter-Sized Robotic Systems and Applications*, Springer, 2014, pp. 28–38.

[8] D. Ahmed, A. Ozcelik, N. Bojanala, N. Nama, A. Upadhyay, Y. Chen, W. Hanna-Rose, and T. J. Huang, "Rotational manipulation of single cells and organisms using acoustic waves," *Nat Commun*, vol. 7, 2016.

[9] B. Jang, A. Hong, H. E. Kang, C. Alcantara, S. Charreyron, F. Mushtaq, E. Pellicer, R. Büchel, J. Sort, S. S. Lee, *et al.*, "Multiwavelength light-responsive Au/B-TiO2 janus micromotors," *ACS Nano*, vol. 11, no. 6, pp. 6146–6154, 2017.

[10] E. Diller, J. Giltinan, and M. Sitti, "Independent control of multiple magnetic microrobots in three dimensions," *Int J Rob Res*, vol. 32, no. 5, pp. 614–631, 2013.

[11] I. S. Khalil, V. Magdanz, S. Sanchez, O. G. Schmidt, and S. Misra, "Three-dimensional closed-loop control of self-propelled microjets," *Appl Phys Lett*, vol. 103, no. 17, p. 172 404, 2013.

[12] P. Ferraro, S. Grilli, D. Alfieri, S. De Nicola, A. Finizio, G. Pierattini, B. Javidi, G. Coppola, and V. Striano, "Extended focused image in microscopy by digital holography," *Opt Express*, vol. 13, no. 18, pp. 6738–6749, 2005.

[13] P. Grossmann, "Depth from focus," *Pattern Recognit Lett*, vol. 5, no. 1, pp. 63–69, 1987.

[14] Z. Zhang and C.-H. Menq, "Three-dimensional particle tracking with subnanometer resolution using off-focus images," *Appl Opt*, vol. 47, no. 13, pp. 2361–2370, 2008.

[15] D. Vilela, U. Cossío, J. Parmar, A. M. Martínez-Villacorta, V. Gómez-Vallejo, J. Llop, and S. Sanchez, "Medical imaging for the tracking of micromotors," *ACS Nano*, vol. 12, no. 2, pp. 1220–1227, 2018.

[16] J. Garcia-Sucerquia, W. Xu, S. K. Jericho, P. Klages, M. H. Jericho, and H. J. Kreuzer, "Digital in-line holographic microscopy," *Appl Opt*, vol. 45, no. 5, p. 836, 2006, ISSN: 0003-6935.

[17] T. Latychevskaia and H.-W. Fink, "Practical algorithms for simulation and reconstruction of digital in-line holograms," *Appl Opt*, vol. 54, no. 9, pp. 2424–2434, Mar. 2015.

[18] D. Gabor, "A new microscopic principle," *Nature*, vol. 161, no. 4098, pp. 777–778, 1948.

[19] W. S. Haddad, D. Cullen, J. C. Solem, J. W. Longworth, A. McPherson, K. Boyer, and C. K. Rhodes, "Fourier-transform holographic microscope," *Appl Opt*, vol. 31, no. 24, pp. 4973–4978, 1992.

[20] M. F. Toy, S. Richard, J. Kühn, A. Franco-Obregón, M. Egli, and C. Depeursinge, "Enhanced robustness digital holographic microscopy for demanding environment of space biology.," *Biomed Opt Express*, vol. 3, no. 2, pp. 313–326, Feb. 2012.

[21] P. Memmolo, A. Finizio, M. Paturzo, L. Miccio, and P. Ferraro, "Twin-beams digital holography for 3D tracking and quantitative phase-contrast microscopy in microfluidics," *Opt Express*, vol. 19, no. 25, pp. 25 833–25 842, 2011.

[22] I. Pushkarsky, Y. Liu, W. Weaver, T.-W. Su, O. Mudanyali, A. Ozcan, and D. Di Carlo, "Automated single-cell motility analysis on a chip using lensfree microscopy," *Sci Rep*, vol. 4, 2014.

[23] M. Heydt, A. Rosenhahn, M. Grunze, M. Pettitt, M. Callow, and J. Callow, "Digital in-line holography as a three-dimensional tool to study motile marine organisms during their exploration of surfaces," *J Adhes*, vol. 83, no. 5, pp. 417–430, 2007.

[24] J. Fung, K. E. Martin, R. W. Perry, D. M. Kaz, R. McGorty, and V. N. Manoharan, "Measuring translational, rotational, and vibrational dynamics in colloids with digital holographic microscopy.," *Opt Express*, vol. 19, no. 9, pp. 8051–8065, Apr. 2011.

[25] U. Schnars and W. P. O. Jüptner, "Digital recording and numerical reconstruction of holograms," *Meas Sci Technol*, vol. 13, no. 9, R85, 2002.

[26] T. M. Kreis, M. Adams, and W. P. Jueptner, "Digital in-line holography in particle measurement," in *Proc SPIE Interferometry '99: Techniques and Technologies*, International Society for Optics and Photonics, 1999, pp. 54–64.

[27] N. Demoli, J. Meštrović, and I. Sović, "Subtraction digital holography," *Appl Opt*, vol. 42, no. 5, pp. 798–804, 2003.

[28] G. Pan and H. Meng, "Digital holography of particle fields: Reconstruction by use of complex amplitude," *Appl Opt*, vol. 42, no. 5, pp. 827–833, 2003.

[29] R. P. Brent, *Algorithms for minimization without derivatives*. Courier Corporation, 2013.

[30] M. P. Kummer, J. J. Abbott, B. E. Kratochvil, R. Borer, A. Sengul, and B. J. Nelson, "OctoMag: An electromagnetic system for 5-DOF wireless micromanipulation," *IEEE Trans Rob*, vol. 26, no. 6, pp. 1006–1017, 2010.

[31] J. Nickolls, I. Buck, M. Garland, and K. Skadron, "Scalable parallel programming with CUDA," in *ACM SIGGRAPH 2008 classes*, ACM, 2008, p. 16.

# AYOUNG HONG

ETH Zurich, Multi-scale Robotics Lab
Hoffeld 24, 8057 Zurich, Switzerland
E-mail: ahong@ethz.ch, ayoung911@gmail.com
Phone: +41 (78) 966 - 6761

## RESEARCH INTEREST

Medical/Surgical robots, Medical image processing
Microrobots, Automation in microscales
Optimal control, Discrete control systems

## EDUCATION

**ETH Zurich**, *Zürich, Switzerland*
**PhD Student** *Mechanical and Process Engineering*                    Jul 2013 – current

- *Dissertation :* A flexible needle with fluoroscopic imaging and magnetic steering for neurosurgical applications
- *Supervisor :* Prof. Dr. Bradley J. Nelson
- *Defended in Oct 2018*

**KAIST**, *Daejeon, Republic of Korea*
**M.S.** *Mechanical Engineering*                    Sep 2009 – Feb 2012

- *Thesis :* Stabilization of bilateral teleoperation system with packet loss in communication
- *Supervisor :* Prof. Dr. Doo Yong Lee
- GPA : 3.71/4.3

**B.S.** *Mechanical Engineering*                    Mar 2005 – Aug 2009

- Graduated with Magna Cum Laude
- Major GPA: 3.91/4.3, Cumulative GPA : 3.87/4.3
- Exchange student at Georgia Institute of Technology, Atlanta, USA

## PROFESSIONAL EXPERIENCE

- **ETH Zurich**, *Zürich, Switzerland*
  Research assistant                    Jul 2013 – Dec 2018
  Teaching assistant for Theory of Robotics and Mechatronics                    2013 – 2017
- **KIMM**, *Daegu, Republic of Korea*
  Research assistant                    Dec 2012 – Jun 2013
  worked on teleoperation system setup with KUKA robot and haptic device
- **Max Planck Institute for Biological Cybernetics**, *Tübingen, Germany*
  Research assistant                    Jan 2012 – Oct 2012
  worked on psychophysical study on multi-modal feedback in multi-robot teleoperation and teleoperation with imperfect communication

# HONORS AND AWARDS

- **Best Project Award for the Hamlyn winter school** on surgical imaging and vision, 2017
- **IEEE RAS Travel Awards** for CASE, Fort Worth, 2016
- **IEEE RAS Travel Awards** for ICRA, Seattle, 2015
- **MPG-ETH Zurich Center for Learning Systems Associate Fellow** from 2015
- **Global Internship Program Fellowship** with the award of 9066 Euros from the National Research Foundation of Korea (NRF), 2012
- **Outstanding Achievement Cum Laude Award** from the Mechanical Engineering Department, KAIST based on the academic merit, 2006
- **National Science and Engineering Undergraduate Scholarship** from Korea Student Aid Foundation from 2005 to 2009
- **Samsung Junior Frontier Leader Scholarship** from Samsung Electronics from 2005 to 2008

# SELECTED PUBLICATIONS

1. **A. Hong**, A. J. Petruska, and B. J. Nelson, "Magnetic Needle Guidance for Neurosurgery using a Single Fluoroscopic Image" in preparation.

2. **A. Hong**, Q. Boehler, R. Moser, L. Stieglitz, A. Zemmar and B. J. Nelson, "3D Path Planning for Flexible Needle Steering in Neurosurgery" under review.

3. B. Jang*, **A. Hong**\*, C. Alcantara, G. Chatzipripiridis, X. Marti, E. Pellicer, J. Sort, Y. Harduf, Y. Or, B. J. Nelson, and S. Pané, "Programmable Locomotion Mechanisms of Hard-Magnetic Nanowires Near a Surface Boundary" in *ACS Appl Mater Interfaces*, vol.11, pp.3214-3223, 2019. (*equal contribution)

4. S. Mohanty, **A. Hong**, C. Alcantara, A. J. Petruska, and B. J. Nelson, "Stereo holographic diffraction based tracking of microrobots," in *IEEE Robotics and Automation Letters*, vol.3, no.1, pp.567-572, 2018.

5. B. Jang, **A. Hong**, H. Kang, C. Alcantara, S. Charreyron, F. Mushtaq, E. Pellicer, R. Büchel, J. Sort, S. Lee, B. J. Nelson and S Pané, "Multi-wavelength light-responsive Au/B-$TiO_2$ Janus Micromotors," in *ACS Nano*, vol.11, pp.6146-6154, 2017.

6. **A. Hong**, D. G. Lee, and H. H. Bülthoff, and H. I. Son, "Multimodal Feedback for Teleoperation of Multiple Mobile Robots in an Outdoor Environment," in *Journal on Multimodal User Interfaces*, vol.11, pp.67-80, 2017.

7. D. Ahmed, C. Dillinger, **A. Hong**, and B. J. Nelson, "Artificial acousto-magnetic soft microswimmers," in *Advanced Materials Technology*, vol.2, no.7, 2017.

8. **A. Hong**, B. Zeydan, S. Charreyron, M. F. Toy, O. Ergeneman, S. Pané, A. J. Petruska, and B. J. Nelson, "Real-Time Holographic Tracking for the 3D Control of Microrobots," in *IEEE Robotics and Automation Letters*, vol.2, no.1, pp.143-148, Jan. 2017.

9. B. Jang, W. Wang, S. Wiget, A. J. Petruska, X. Chen, C. Hu, **A. Hong**, D. Folio, A. Ferreira, S. Pané, and B. J. Nelson,"Catalytic Locomotion of Core-Shell Nanowire Motors," in *ACS Nano*, vol.10, no.11, pp.9983-9991, 2016.

10. A. J. Petruska, F. Ruetz, **A. Hong**, L. Regli, O. Sürücü, A. Zemmar, and B. J. Nelson, "Magnetic Needle Guidance for Neurosurgery: Initial Design and Proof of Concept," in *Proceedings of IEEE International Conference on Robotics and Automations (ICRA'16)*, Stockholm, Sweden, May 2016.

11. **A. Hong**, A. J. Petruska, and B. J. Nelson, "Tracking a Magnetically Guided Catheter with a Single Rotating C-Arm," in *Proceedings of IEEE International Conference on Robotics and Automations (ICRA'15)*, Seattle, US, May 2015.

12. **A. Hong**, H. H. Bülthoff, and H. I. Son, "A Visual and Force Feedback for Multi-Robot Teleoperation in Outdoor Environments: A Preliminary Results," in *Proceedings of IEEE International Conference on Robotics and Automations (ICRA'13)*, Karlsruhe, Germany, May 2013.

## PROFESSIONAL SKILLS

C/C++, MATLAB/Simulink, LabView, OpenCV, OpenGL, ROS
AutoCAD, SolidWorks, Latex, MS Office